Engineering quantum systems for information processing and metrology using atoms, superconductors, and light

Dissertation
der Mathematisch-Naturwissenschaftlichen Fakultät
der Eberhard Karls Universität Tübingen
zur Erlangung des Grades eines
Doktors der Naturwissenschaften
(Dr. rer. nat.)

vorgelegt von
Lőrinc Sárkány
aus Szeged, Ungarn

Tübingen
2018

Tag der mündlichen Qualifikation:	15.05.2018
Dekan:	Prof. Dr. Wolfgang Rosenstiel
1. Berichterstatter:	Prof. Dr. József Fortágh
2. Berichterstatter:	Assoc. Prof. Dr. David Petrosyan
3. Berichterstatter:	Assoc. Prof. Dr. Rainer H. Dumke

Abstract

This thesis intends to give a concise yet meaningful overview about the progress in the physical realization of quantum information processing using hybrid systems of ultracold atoms and superconducting microwave resonators, describing our own theoretical and experimental contributions to advancing.

Ultracold atoms in their ground states are well-isolated quantum systems offering long coherence times, and therefore are prime candidates for quantum memory applications. Their performance is limited by their sensitivity on external magnetic-field noises and inhomogeneous Zeeman shifts inherently present in magnetic traps. We have developed an efficient method to eliminate the magnetic-field dependence of the differential Zeeman shift between the magnetically trappable clock-states up to second order around an arbitrarily chosen offset field, hence rendering atom-based quantum memory insensitive to magnetic noises.

We describe two protocols to mediate long-range interactions between Rydberg atoms using a thermally populated microwave cavity, realizing universal 2-bit quantum gates. This is of great practical interest, since in existing hybrid atom-superconducting resonator experiments the attainable temperature is not low enough to reach the vacuum state of the cavity mode. The first method relies on active mode cooling using an auxiliary reservoir of atoms. The second method makes use of a destructive quantum interference between different excitation paths, making the scheme insensitive to the actual photon state of the cavity.

We also report on a new laboratory for optical lattice clocks that we have established in parallel with this work. We present a novel concept for continuously operated atomic clocks, along with the steps we have taken towards its experimental realization.

Zusammenfassung

Diese Dissertation soll einen kurzen aber dennoch aussagekräftigen Überblick über die Fortschritte bei der Realisierung von Quanteninformationsverarbeitung mit Hybridsystemen aus ultrakalten Atomen und supraleitenden Resonatoren geben. Dabei sollen in erster Linie unsere eigenen theoretischen und experimentellen Beiträge zu diesem Forschungsfeld dargestellt werden.

Ultrakalte Atome im Grundzuständ sind von der Umgebung gut isoliert. Sie ermöglichen daher lange Kohärenzzeiten und sind erstklassige Kandidaten für die Anwendung als Quantenspeicher. Ihre Leistungsfähigkeit ist jedoch durch ihre Empfindlichkeit gegenüber äußeren Magnetfeldfluktuationen und durch die inhomogene Zeeman-Verschiebung in magnetischen Fallen limitiert. Es wird eine effiziente Methode entwickelt, um die differenzielle Zeeman-Verschiebung zwischen den beiden magnetisch fangbaren Uhrenzuständen bis zur zweiten Ordnung im Magnetfeld um ein beliebiges Offsetfeld auszugleichen. Damit werden gegen Magnetfeldfluktuationen unempfindliche atom-basierte Quantenspeicher ermöglicht.

Es werden zwei Protokolle beschrieben, mit denen sich langreichweitige Wechselwirkungen zwischen Rydberg-Atomen über einen thermisch besetzten Mikrowellenresonator und damit 2-Bit Quantengatter realisieren lassen. Die Entwicklung solcher Protokolle ist von großem praktischem Interesse, da die erreichbare Temperatur in bestehenden Versuchsaufbauten mit Atomen und Supraleitern nicht tief genug ist, um den Resonator in einen Vakuumzustand zu bringen. Die erste Methode basiert auf der kontinuerlichen Entnahme von thermischen Photonen aus dem Resonator mithilfe einer zusätzlichen Atomwolke. Die zweite Methode nutzt die destruktive Quanteninterferenz zwischen unterschiedlichen Anregungspfaden und macht das Schema damit von der Anzahl der Photonen im Resonator unabhängig.

Darüber hinaus wird der Aufbau eines neuen Labors für optische Atomuhren beschrieben. Insbesondere soll ein neuartiges Konzept für den kontinuerlichen Betrieb von Atomuhren sowie die durchgeführten Schritte zu dessen Realisierung dargestellt werden.

Contents

1 List of publications

This is a cumulative thesis based on the publications listed below. The publications are appended at the very end of the thesis.

1.1 Appended publications

Publication [PUB 1]

L. Sárkány, P. Weiss, H. Hattermann, and J. Fortágh

Controlling the magnetic-field sensitivity of atomic-clock states by microwave dressing

Phys. Rev. A **90**, 053416 (2014)

Publication [PUB 2]

L. Sárkány, J. Fortágh, and D. Petrosyan

Long-range quantum gate via Rydberg states of atoms in a thermal microwave cavity

Phys. Rev. A **92**, 030303 (R) (2015)

Publication [PUB 3]

L. Sárkány, J. Fortágh, and D. Petrosyan

Faithful state transfer between two-level systems via actively cooled finite-temperature cavity

Phys. Rev. A 97, 032341 (2018)

Publication [PUB 4]

P. Weiss, M. Knufike, S. Bernon, D. Bothner, **L. Sárkány**, C. Zimmermann, R. Kleiner, D. Koelle, J. Fortágh, and H. Hattermann

Sensitivity of Ultracold Atoms to Quantized Flux in a Superconducting Ring

Phys. Rev. Lett. **114**, 113003 (2015)

Publication [PUB 5]

M. Mack, J. Grimmel, F. Karlewski, **L. Sárkány**, H. Hattermann, and J. Fortágh

All-optical measurement of Rydberg-state lifetimes

Phys. Rev. A **92**, 012517 (2015)

Publication [PUB 6]

H. Hattermann, D. Bothner, L. Y. Ley, B. Ferdinand, D. Wiedmaier, **L. Sárkány**, R. Kleiner, D. Koelle, and J. Fortágh

Coupling ultracold atoms to a superconducting coplanar waveguide resonator

Nature Communications **8**, 2254 (2017)

1.2 Contributions

- **Publication [PUB 1]**

  I have proposed the idea of microwave dressing as a possible technique to combat the detrimental effects of the magnetic-field noises and inhomogeneities on the phase coherence of an atomic cloud, and established the theoretical foundation of the experiment. The measurements were done by H. Hattermann and myself, the evaluation was predominantly my duty, the manuscript was written by H. Hattermann with contributions from J. Fortágh and myself.

- **Publication [PUB 2]**

  All three authors have participated in developing the main idea behind this work. The analytical calculations were done by D. Petrosyan and myself, while I have performed all the numerical calculations. The manuscript was written mostly by J. Fortágh and myself, with significant contributions from D. Petrosyan.

- **Publication [PUB 3]**

  All three authors have contributed to developing the main idea behind this work. I have participated in the analytical and numerical calculations, as well as in writing the manuscript.

- **Publication [PUB 4]**

  I have contributed to the evaluation of the effects of the quantized magnetic flux on the magnetic trapping potentials.

- **Publication [PUB 5]**

  I have participated in the conception of the experiment, building up and maintaining the setup.

- **Publication [PUB 6]**

  I have provided the microwave dressing framework for the experiment, and participated in discussing the results.

2 Hardware for quantum computation

Calculating the behavior of large quantum systems using classical computers is an extremely difficult task, since the necessary resources grow exponentially with the size of the system. A natural alternative approach is to consider if we could utilize quantum systems to perform simulations and calculations about another one on a more fundamental level.

R. Feynman has proposed the idea of quantum simulation, also called analog quantum computing [1]. A few years later D. Deutsch has created the concept of the universal (digital) quantum computer [2] that serves as the core concept of quantum computation (QC). Independently, following the pioneering work of S. Wiesner [3] that has established the field of quantum cryptography, C. Bennett and G. Brassard have invented the first quantum key distribution protocol [4].

Ever since the field has exploded. A large number of efficient quantum algorithms have been developed that provide us with an exponential speed-up compared to the classical algorithms for various complex problems [5]. Famous examples include the Deutsch-Jozsa algorithm [6], Shor's algorithm for integer-factorization [7], or the HHL algorithm for solving systems of linear equations [8]. Other algorithms, such as the quantum Fourier transform, or Grover's algorithm for searching efficiently in a large unstructured database [9] also provide significant reduction in necessary computational effort. Ultracold atom-based analog quantum simulators have been realized to study the properties of spin chains [10–12]. Large-scale optimization problems are tackled by commercially available quantum annealers operating with 1000+ solid-state qubits [13].

In order to harness the benefits of quantum algorithms, current research is devoted to construct the quantum analogue of digital computers. Since digital quantum computers mimic the architecture of classical computers, the tasks to be solved are rather familiar: information must be represented, processed, stored and transported, leading to the need for qubits, quantum gates, quantum memories and quantum communication. Each of this subsystems should fulfil different requirements, e.g a quantum processor must be able to process information fast, but not necessarily be able to store it for a longer period of time, while an ideal memory possesses exactly the opposite properties.

Many computationally equivalent paradigms exist for quantum computing, e.g. the cluster-state QC which assumes a highly entangled many-qubit state, but uses only one-bit gates afterwards [14] or the topological QC operating with anyons [15].

Here, we focus on the most common architecture, the circuit-QC [16, 17]. The five general criteria of this approach were first summarized by DiVincenzo [18]. First, information is represented on two-level quantum systems with long-lived states $|0\rangle$ and $|1\rangle$ (called *qubits*) by superposition states $|\Psi\rangle = \alpha|0\rangle + \beta|1\rangle$. Quantum algorithms are unitary operations carried out by *quantum gates* acting on either a single or multiple qubit(s), following the Boolean-logic based approach from classical computers. Second, one must be able to initialize the qubits in a well-defined and known initial state. Third, since in a realistic qubit quantum information will be degraded due to dephasing originating from the qubit's intrinsic decay processes as well as its coupling to the environment, every operation on qubits must be performed faster than the timescale of any of the relevant decohering processes to minimize information loss. In classical computers the equivalent challenge is efficiently overcome by periodicly rewriting the information to the memory bits before they have decayed completely. Unfortunately, this strategy does not work with qubits due to the no-cloning theorem [19], but the issue can still be partially handled by using *quantum error correction codes* [20] which are also helpful in fighting the errors caused by non-perfect execution of gate operations. Fourth, one must be able to perform multiple-qubit operations in order to harness the resource provided by quantum entanglement. In principle, it is enough to realize single- and certain two-qubit operations (called *universal gates*), since every multiple-qubit operation can be decomposed to a product of such gates [16], but from a practical point of view it might be advantegous to have gates acting on multiple quantum bits as well, since they might significantly reduce the number of required gate operations. Famous universal quantum gates include the controlled NOT (CNOT), controlled PHASE (CPHASE), and controlled SWAP gates (CSWAP) [16]. Fifth, the final state of the qubit must be measurable.

The accuracy or degree of success of any particular gate execution is measured by the *fidelity*, defined as $F \equiv |\langle \Psi_{\text{target}} | \Psi_{\text{act}} \rangle|$, where $|\Psi_{\text{target}}\rangle$ is the target quantum state and $|\Psi_{\text{act}}\rangle$ is the state actually obtained after performing the operation. When designing a quantum gate, higher fidelity is surely desirable, but at some point further improvement will invoke severe technological challenges, therefore it is vital to know what we should aim for. This is a non-trivial question to answer, it depends (among many other factors) on the applied error-correction code, the physical realization of the qubits, and the type of gates being considered. For a detailed review see [21]. According to the current state-of-the-art research, the acceptable infidelity level lies around $10^{-2} - 10^{-4}$.

We note that the DiVincenzo criteria are much more stringent than what is necessary for quantum annealing. The reason is that in this latter case the task is to find the ground state of a system, which represents the solution of the optimization problem. This is usually done by adiabatically transforming the Hamiltonian from an easily preparable and accessible staring point by turning on couplings and interactions within the system. In case of QC, we aim for much more. The benefit is of course that a quantum computer is a general purpose device, while an optimizer is problem-specific. This point is well-demonstrated by the fact that optimizators are available with more than thousand qubits [13], while the current world-record general-purpose quantum computer has 14 qubits [22], to the best of our knowledge.

After performing the specified quantum algorithm, quantum information must be stored in a local *quantum memory*, similarly to classical computers. The memory and the processor might be realized in the same quantum system, e.g. with ultracold atoms (see Sec. 2.1), but in general they might be two different quantum systems as well, since contradicting needs have to be fulfilled. A good processor should interact strongly with external fields, which also makes it susceptible to decoherence induced by environmental noises. Vice verse, a good quantum memory, i.e. an isolated quantum system, does not interact strongly. Therefore a *quantum bus* might be necessary to transfer information between the different subsystems. The bus can also be used to introduce long-range interactions between qubits, see Sec. 2.3.

Such "combined" systems are called *hybrid systems*. A crucial requirement for this scheme to be useful is that each connection between the subsystems should be strong enough so that information can be transferred without significant decoherence. In particular, the Hamiltonian describing the coupling typically has the form $H_{\mathrm{AB}} = \hbar g(a+a^\dagger)(b+b^\dagger)$, where g is the coupling strength, a and b are the bosonic de-excitation operators in subsystems A and B, e.g. atomic lowering operators, photon or phonon annihilator [23, 24]. Furthermore, let γ be the typical rate of decoherence in the system, including possible atomic decay rates, cavity damping rate, dephasing etc. Ideally $\gamma = 0$, in this case the coupling Hamiltonian leads to coherent Rabi oscillations between A and B. The coupling is said to be *weak*, if $\omega_A, \omega_B \gg \gamma > g$, where $\omega_A \approx \omega_B$ are the excitation energies in the corresponding subsystems. In this case, the oscillation is damped before a complete oscillation could be completed, coherent exchange of quantum information is not possible. For $\omega_A, \omega_B \gg g \gg \gamma$ we have *strong coupling*. Here, exchange is possible with high fidelity, and the dynamics of the system can be well approximated by the Jaynes-Cummings Hamiltonian $H_{\mathrm{JC}} = \hbar g(a^\dagger b + b^\dagger a)$, which is essentially a rotating-frame approximation (RWA) of H_{AB}. The coupling is said to be *ultrastrong* if $\omega_A, \omega_B \sim g > \gamma$. In this regime RWA breaks down, and more involved calculations are necessary to study the dynamics. Ultrastrong coupling has been established in certain systems (see below). However, in atomic physics strong coupling is usually aimed for.

A commonly used technique to enhance the coupling strength is to couple an ensemble of N indistinguishable particles from subsystem A instead of a single one. In this case the system is described by the Tavis-Cummings Hamiltonian $H_{\mathrm{TC}} = \hbar\sqrt{N}g\,(\mathcal{A}^\dagger b + \mathcal{A}b^\dagger)$, where $\mathcal{A} = 1/\sqrt{N}\,\sum_{i=1}^{N} a_i$ is the collective lowering operator [25]. The ensemble behaves as a large collective spin that couples to B with an effective coupling strength $g_{\mathrm{eff}} = \sqrt{N}g$.

Various quantum systems have been investigated as qubit candidates, e.g. single photons [26], ultracold neutral atoms [27] and ions [28, 29], polar molecules [30, 31], ensembles of electronic and nuclear spins [32–34], mesoscopic superconducting [35–37] and mechanical devices [38]. Each of these systems have their own merits. For example, superconducting structures are primary candidates for quantum processors due to their (ultra)strong coupling to microwave fields with technologically convenient frequencies [39], integrability to solid-state circuits, and well-established fabrication techniques. However, they are known to be susceptible to decoherence arising from spurious interactions with magnetic moments and phonons in the substrates [24, 37], limiting their coherence times only to a couple of μs, and they do not couple directly to optical photons, which would be a necessity to be able to transfer quantum information over large distances.

Much progress has been achieved in experimental realization of hybrid quantum systems as well. Coupling ensembles of nitrogen vacancy centers (NV) in diamond to superconducting qubits via microwave resonators was one of the earliest proposals [40, 41]. Strong coupling strength on the order of $5 - 50$ MHz has indeed been achieved, although the storage time is severly limited to a few hundred nanoseconds [42, 43]. Nuclear spin systems offer significantly higher storage time ($\sim$ 1s) [33] at a cost of weaker coupling. Direct coupling between NV centers and flux qubits has been demonstrated [44]. Ions in solid-state systems have also been successfully coupled strongly to microwave resonators [45–47].

2.1 Ultracold atoms

Ultracold alkaline atoms in their hyperfine ground states are well isolated quantum systems, providing long coherence times [48], therefore they are ideal candidates for quantum memories. Ensembles of ultracold atoms [49, 50] and even a single atom in an optical cavity [51] have indeed been utilized for this purpose. An elementary quantum network has been demonstrated with the latter system [52], and recently coherent microwave-to-infrared upconversion has been proposed with ultracold atoms [53, 54]. On the other hand, quantum gates based on the strong dipole-dipole interaction between highly-excited Rydberg atoms have also been proposed and realized [55–59].

Here we consider ^{87}Rb to illustrate this dual usability of ultracold atoms. Its level structure is depicted in Fig. 1. The ground state is split into two hyperfine-states with total angular momentum $F = 1$ and $F = 2$, the splitting is $\omega_{\mathrm{HFS}} \approx 2\pi \times 6.834$ GHz. The transition between the two states is magnetic-dipole-allowed. In presence of magnetic fields they are further split into three resp. five Zeeman sublevels. The dependence of the energy on the field strength can be calculated analiticly and is given by the Breit-Rabi formula [60]. The states $|5S_{1/2}F = 1, m_F = -1\rangle$, $|5S_{1/2}F = 2, m_F = 1\rangle$, and $|5S_{1/2}F = 2, m_F = 2\rangle$ are magnetically trappable. As the magnetic moments of the former two have similar magnitudes, they are often used in magnetically trapped atomic clock experiments, and as qubit states in quantum memory applications [61–64]. However, the slight mismatch between them is still a dominant source of error. We have developed an efficient method to

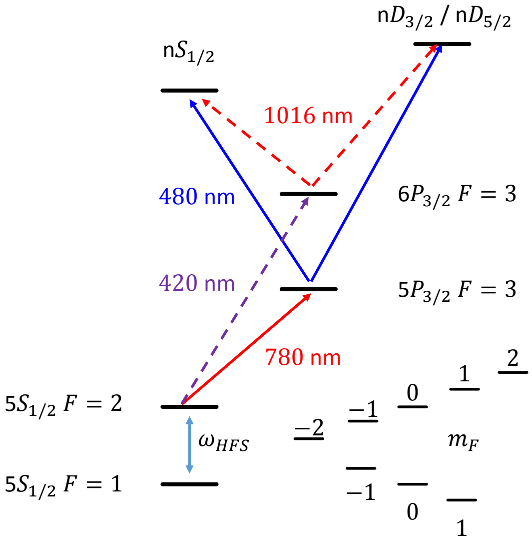

Figure 1: Level structure of ^{87}Rb. The ground-state is split into two hyperfine states ($F = 1$ and $F = 2$) with separation $\omega_{\mathrm{HFS}} = 2\pi \times 6.834$ GHz. In external magnetic fields they are further split into three and five Zeeman sublevels. Two possible two-photon Rydberg excitation pathways used in our research group are depicted, the intermediate state is either $5P_{3/2}$ or $6P_{3/2}$.

Property	n-scaling	^{87}Rb (50P)
Radiative lifetime	n^3	106 μs
Orbital radius	n^2	170 nm
Dipole moment $\langle ns\|d\|np\rangle$	n^2	3200 ea_0
Scalar polarizability	n^7	$\sim$ GHz cm$^2/V^2$

Table 1: Scaling laws for basic Rydberg properties. Values are taken from [68], a_0 is denoting the Bohr radius.

overcome this issue, presented in Sec. 2.1.1.

Transitions between highly-excited Rydberg states also lie in the microwave regime. Rydberg atoms possess remarkable properties putting them in the limelight of recent research. Their energy spectrum is similar to that of hydrogen:

$$E_{\mathrm{n,l,j}} = E_\infty - \frac{Ry^*}{(n^*)^2}, \tag{1}$$

where $E_\infty/\hbar = 2\pi \times 1010.0291646$ THz is the ionization energy, $Ry^*/\hbar = 2\pi \times 3289.82119466$ THz is the Rydberg-constant corrected for the reduced electron mass in ^{87}Rb, and $n^* \equiv n - \delta_{\mathrm{n,l,j}}$ with $\delta_{\mathrm{n,l,j}}$ being the so-called quantum defect [65]. The physical picture behind this formula is that the single valence electron experiences the potential of the point-like nucleus shielded by the core electrons accounted for by the quantum defect. This effective potential is well-understood [66], the energy levels can be accurately calculated and measured experimentally [65]. Rydberg states of ^{87}Rb can be directly excited from the ground state with a 297 nm laser. Due to technological complexity associated with UV-lasers, it is common to use a two-photon excitation via the $5P_{3/2}$ ($6P_{3/2}$) state instead using 780 nm / 480 nm (420 nm / 1016 nm) lasers, either by resonant π-pulses or using Stimulated Adiabatic Raman Passage (STIRAP). For an exhaustive review comparing the two methods see [67]. While the choice of the intermediate state, the detunings and the applied laser power do make a difference in how coherent the excitation is, for our purpose now we can treat the excitation as an effective process, neglecting these details.

Several key properties of Rydberg atoms exhibit scaling laws in powers of n [68]. The ones that will be important for us are summarized in Tab. 1. What makes Rydberg atoms particularly interesting for QC is their exceptionally high electric dipole moments, promising strong electric dipole coupling to microwave fields, cf. Sec. 2.2.1.

The strong interaction between Rydberg atoms leads to another remarkable effect, the *Rydberg blockade* [55]. Consider N atoms in the ground state subjected to a laser exciting them into a Rydberg state. In vague terms if one atom is promoted to a Rydberg state, the excitation frequency for any sufficiently nearby atom is shifted due to the strong interaction. Hence, if the excitation laser frequency is kept constant, a second Rydberg excitation is forbidden within a certain distance called the *blockade radius*. Since atoms are equivalent, as long as this simple picture holds, the ensemble can be described with collective Dicke-states $|G\rangle = |g_1 \dots g_N\rangle$ and $|R\rangle = 1/\sqrt{N}\sum_{i=1}^{N} |gg \dots gr_i g \dots g\rangle$ [69]. The blockade effect ensures that the system is confined to the subspace spanned by these two vectors, hence the whole ensemble behaves as an effective two-level system, called the *superatom*. Furthermore, the effective coupling between $|G\rangle$ and $|R\rangle$ is enhanced by a factor of $\sqrt{N}$ with respect to the single atom value Ω, analogously to the Tavis-Cummings model discussed earlier.

This effect has been demonstrated experimentally [70–73], and is of great practical interest, since simply by turning to ensembles, one wins a significant enhancenement in the excitation rate, which is usually severely limited by the available laser power. However, it is easy to see, that one does not have such enhancement between two symmetric states, e.g. when coupling two neighboring Rydberg states (both blockaded) with a microwave.

The blockade radius is defined as the distance where the interaction shift equals the effective linewidth of the excitation [74]. In general, the interaction potential is not isotropic, and can only be calculated numerically [75–77]. As a first approximation, it shows a crossover from dipole-dipole: $U_{\mathrm{dd}} = C_3/R^3$ (valid for $R \ll R_c$) to van der Waals interaction: $U_{\mathrm{vdW}} = C_6/R^6$ (for $R \gg R_c$), upon varying the interatomic distance. Here, R_c is the crossover-distance, which is highly state-dependent and typically lies around $R_c = 1 - 8\ \mu$m [75]. This leads to the following formula for the blockade radius:

$$d_b = \left(\frac{C_p}{2\Omega} \sqrt{\frac{\Gamma_r}{\gamma_{rg}}} \right)^{1/p}, \tag{2}$$

where the target Rydberg state with natural decay rate Γ_r is excited with Rabi frequency Ω. Here, $\gamma_{rg} \equiv \Gamma_r/2 + 2\Gamma_z$ is the total dephasing rate of the Rydberg state, while Γ_z quantifies the dephasing rate with respect to the ground state including all the technical dephasings as well (e.g. laser linewidth). For dipole-dipole and van der Waals interaction, $p = 3$ and $p = 6$, respectively.

It is important to emphasise that the blockade radius is *not* an intrinsic atomic property, it depends on the applied excitation laser power, the linewidth of the laser, and, via the effective dephasing rate, also on the lifetime of the intermediate state and the detuning involved in the two-photon excitation path. There are limitations on the validity of this simple picture [56], and the physics of Rydberg atoms is a rich field on its own.

The lifetime of the Rydberg states is, however, rather short. As stated above, it scales with n^3, but using too high principal quantum numbers quickly becomes counterproductive, due to the increased susceptibility to noise, spurious fields, and collisional ionizations [78]. While turning to circular states, Rydberg states with highest allowed angular momentum, i.e. $l = n - 1$, greatly increases the lifetime to the order of 10 ms [79], it is still too short for quantum memory applications. Hence the proposed usage of atoms in quantum computation is the following. Rydberg atoms can be used to perform the gate operation itself by making use of the strong dipole-dipole interaction between them. Alternatively, they can be coupled to a microwave cavity to receive quantum information from a separate quantum processor. Afterwards, the information must be coherently mapped to the hyperfine ground states for storing.

2.1.1 Noise-insensitive quantum memory

For quantum memory applications it is essential to have long lifetime of atomic coherence. The performance of magnetically trapped atoms are limited by three main factors: electromagnetic noise from the surrounding environment, quadratic residual differential Zeeman shift (see below), and density-dependent collisional shifts [62, 63]. Several methods have been suggested to overcome these hurdles. By carefully choosing the density of the cloud and the trapping parameters, the latter two effects can partially compensate for each other [61]. The identical spin rotation effect, which is essentially a spin-echo-like effect originating from inter-atom interactions and indistinguishability of the atoms has also been demonstrated to increase the coherence times [48, 80]. With careful engineering, coherence times on the order of 10 s have been established in the vicinity of a superconducting CPW resonator [48].

Here, we present a flexible method we have developed to control the magnetic-field sensitivity of the atomic qubit operated at an arbitrary magnetic offset field [PUB 1]. In particular, it is an efficient way to combat magnetic field noises and dephasing originating from moving in the inhomogeneous magnetic field that defines the trapping potential itself. The method allows us to choose the density of the cloud and the offset field of the trap almost arbitrarily and independently from each other.

The energies of ^{87}Rb in magnetic fields are given by Breit-Rabi formula [60]. By expanding it up to second order in B we obtain:

$$\hbar\omega(F=1,m_F) = -m_F\,\mu_1\,B - (4-m_F^2)\beta B^2, \tag{3}$$

$$\hbar\omega(F=2,m_F) = +m_F\,\mu_2\,B + (4-m_F^2)\beta B^2 + \omega_{\mathrm{HFS}}, \tag{4}$$

with

$$\mu_1 = \mu_B\cdot\left(-\frac{5}{4}\,g_I + \frac{1}{4}\,g_J\right) \approx 2\pi\times 702.37\ \text{kHz/G},$$

$$\mu_2 = \mu_B\cdot\left(\frac{3}{4}\,g_I + \frac{1}{4}\,g_J\right) \approx 2\pi\times 699.58\ \text{kHz/G},$$

$$\beta = \frac{1}{16\,\omega_{\mathrm{HFS}}}\,(g_I-g_J)^2\,\mu_B^2 \approx 2\pi\times 71.89\ \text{Hz/G}^2,$$

where g_I and g_J are the Landé g-factors for the nucleus and the electron, respectively. Since μ_1 are μ_2 are "almost equal", when working with magnetic traps one typically chooses $|0\rangle \equiv |5S_{1/2}F=1, m_F=-1\rangle$ and $|1\rangle \equiv |5S_{1/2}F=2, m_F=+1\rangle$ as the two-level system, since their differential Zeeman shift is only weakly depending on the magnetic field. Actually, by setting the offset field of the magnetic trap to

$$B_{\mathrm{off}} = B_{\mathrm{magic}} = \frac{6\beta}{2(\mu_2-\mu_1)} \approx 3.228\ \text{G}, \tag{5}$$

the so-called *magic offset field*, the first order dependence of the differential shift is eliminated, leaving a residual shift of $6\beta\,(B-B_{\mathrm{magic}})^2 \approx 2\pi\times 431\ \text{Hz/G}^2\cdot(B-B_{\mathrm{magic}})^2$.

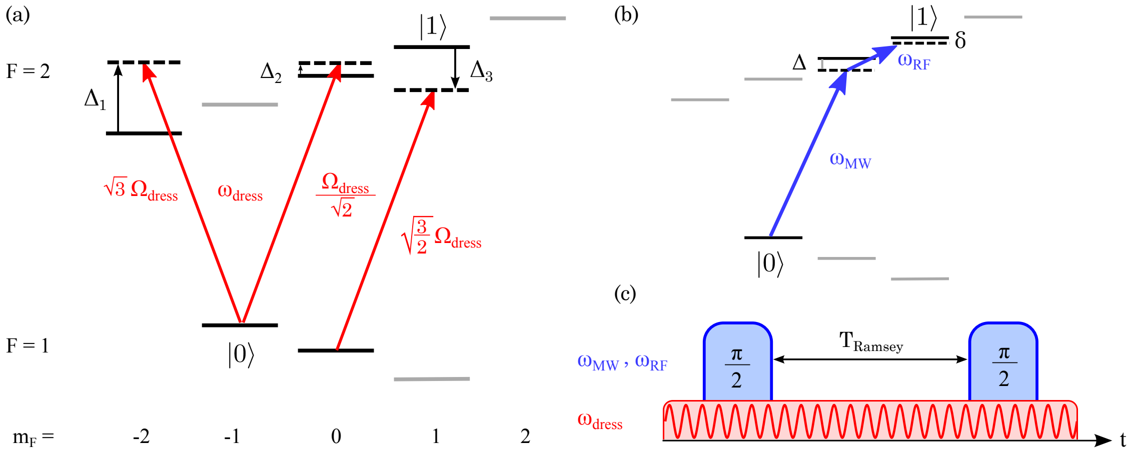

Figure 2: (a) Ground hyperfine-structure and Zeeman sublevels in ^{87}Rb in magnetic field. A microwave field with frequency ω_{dress} and Rabi frequency Ω_{dress} is applied to dress the qubit states. (b) The atomic transition is probed by means of Ramsey interferometry. A two-photon pulse with $\omega_{\mathrm{MW}} \approx 2\pi \times 6.833$ GHz and $\omega_{\mathrm{RF}} \approx 2\pi \times 2$ MHz is used to drive the transition. (c) Schematic of the experimental sequence. A $\pi/2$ pulse is used to prepare the atoms in a superposition state $1/\sqrt{2}\,(|0\rangle + |1\rangle)$. After a variable hold time T_{Ramsey} , the interferometer is closed by the application of a second $\pi/2$ pulse and the population of the two states, oscillating with frequency δ, is measured. The dressing field is left on throughout the interferometer sequence.

The magnetic-field sensitivity is changed if the atoms are subjected to an off-resonant microwave dressing field with frequency ω_{dress} and Rabi frequency Ω_{dress}, see Fig. 2. By choosing these parameters appropriately, the differential Zeeman shift can be shaped nearly arbitrarily around a chosen center point B_{center}, in particular it can be eliminated up to second order in B, leaving only a weak third-order dependence behind. The dressing field exerts AC-Stark shifts on the qubit states, which have the following form in rotating-wave approximation:

$$\Delta\omega_{\mathrm{dress},i} = \sum_{i,\alpha} \frac{\Omega_{i,\alpha}^2}{\Delta_{i,\alpha}}, \tag{6}$$

where $i = |0\rangle$ or $|1\rangle$, and $\alpha = \pi, \sigma_+, \sigma_-$ denotes the possible polarizations of the dressing field with corresponding Rabi frequencies and detunings denoted by $\Omega_{i,\alpha}$ and $\Delta_{i,\alpha}$, respectively. To simplify the situation we have worked with a linearly polarized dressing field with the polarization being perpendicular to the quantization axis. Hence, we only need to take into account σ_+ and σ_- transitions. In this case only three states are relevant for the dressing: $|F = 2, m_F = -2\rangle$ and $|F = 2, m_F = 0\rangle$ for $|0\rangle$, and $|F = 1, m_F = 0\rangle$ for $|1\rangle$. The relevant detunings are given by

$$\Delta_1 = \Delta_{\mathrm{dress}} + (\mu_1 + 2\mu_2)B - 3\beta B^2, \tag{7}$$

$$\Delta_2 = \Delta_{\mathrm{dress}} + \mu_1 B - 7\beta B^2, \tag{8}$$

$$\Delta_3 = \Delta_{\mathrm{dress}} - \mu_2 B - 7\beta B^2, \tag{9}$$

where $\Delta_{\text{dress}} \equiv \omega_{\text{dress}} - \omega_{\text{HFS}}$. With this notation, the differential Zeeman shift between the two states reads as:

$$\begin{aligned}\Delta\omega =&\omega_{\text{HFS}} + (\mu_2 - \mu_1)B + 6\beta B^2 - \\ &- \Omega_{\text{dress}}^2 \cdot \left(\frac{3}{\Delta_1(B)} + \frac{1/2}{\Delta_2(B)} + \frac{3/2}{\Delta_3(B)}\right),\end{aligned} \tag{10}$$

where the state-independent Rabi frequency is defined as

$$\Omega_{\text{dress}} = \frac{1}{2\sqrt{2}}\,\mu_B\,g_F\,|B_{\text{dress}}|. \tag{11}$$

By requiring that the first and second derivatives of Eq. (10) with respect to B disappear at a given offset field B_{center}, we obtain an optimal dressing field characterized by ω_{dress} and Ω_{dress}. By dressing with this field, the differential Zeeman shift is eliminated up to second order around B_{center}. We remark that the choice of B_{center} is only limited by the available microwave power.

To demonstrate the validity of the theory, we have measured the two-photon transition frequency between $|0\rangle$ and $|1\rangle$ as a function of the offset field for different dressing powers. The experimental setup is described elsewhere in detail [48, 81]. An ensemble of ultracold ^{87}Rb atoms is prepared in a magneto-optical trap and subsequently transferred into an Ioffe-Pritchard-type magnetic trap situated in the room-temperature environment of our setup. The atomic cloud is further cooled by forced radio-frequency evaporation and then loaded into an optical dipole trap used to transport the ensemble to a position below the superconducting atom chip at 4.2 K. We load an ensemble of $\sim 1 \times 10^6$ atoms at a temperature of $\sim 1\ \mu$K into the magnetic chip trap, which is based on a Z-wire geometry. The atomic cloud in the magnetic trap is cooled to a temperature of ~ 250 nK by evaporation. After this sequence, which is repeated every 23 s, we end up with an ensemble of roughly 1×10^5 atoms. The frequency of the transition is measured by means of Ramsey interferometry. The interferometric sequence is started 100 ms after switching on the dressing field by applying a combined microwave and radio-frequency two-photon pulse with a pulse area of $\pi/2$, which prepares the atomic ensemble in a coherent superposition of states $|0\rangle$ and $|1\rangle$ see Figs. 2(b) and 2(c). The microwave pulses are irradiated from an external antenna with a wave vector perpendicular to the quantization axis, while the radio-frequency field is generated by an alternating current in the trapping wire. Both frequencies are chosen with a detuning of $\Delta = 2\pi \times 310$ kHz with respect to the transition to the intermediate level $|5S_{1/2}\,F = 2, m_F = 0\rangle$, so that the probability of populating this level is negligible. After a variable hold time T_{Ramsey}, the interferometer is closed by a second $\pi/2$ pulse and we measure the population of the two qubit states, which oscillates with the angular frequency $\delta = |\omega_{\text{MW}} + \omega_{\text{RF}} - \omega_{01}|$. We determine this frequency δ for different offset fields B_{off} and seek to eliminate the magnetic-field dependence of the transition.

We have chosen to cancel the magnetic-field dependence around $B_{\text{off}} = 2.65$ G. The results of the measurement are plotted in Fig. 3, along with the results of the theoretical calculations. The data indeed demonstrate the suppression of the variations in the differential Zeeman shift. The analysis of the theory curves in

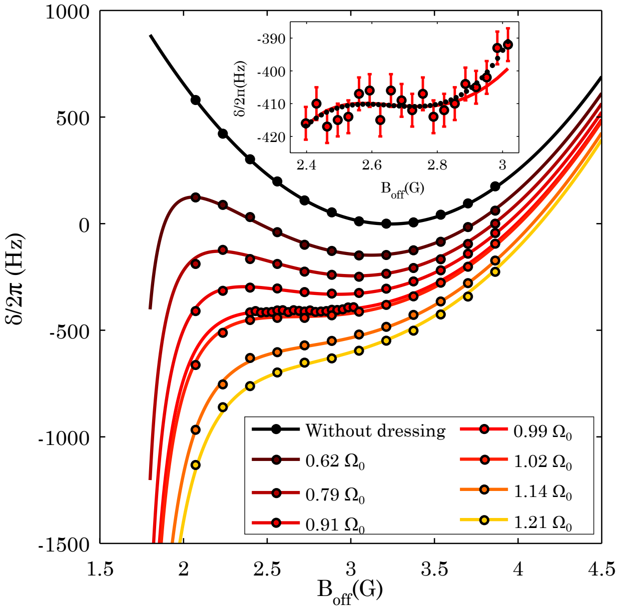

Figure 3: Measurement of the differential Zeeman shift between states $|0\rangle$ and $|1\rangle$ for different dressing powers. The frequency zero point was set to the frequency at the magic offset field without dressing. For a Rabi frequency $\Omega_{\text{dress}} = \Omega_0 = 2\pi \times 20.1$ kHz, the frequency is nearly independent of the magnetic offset field in a range of ± 100 mG around the chosen value $B_{\text{center}} = 2.65$ G. Inset: Detail of the curve with $\Omega_{\text{dress}} = 0.99\Omega_0$. We estimate a measurement error of ± 5 Hz resulting from fluctuations of the MW power. The theory curve (solid red line) is plotted along a polynomial fit (dotted black line), showing the suppression of the first- and second-order Zeeman shift down to a level of -7.3 Hz/G and 5.0 Hz/G^2.

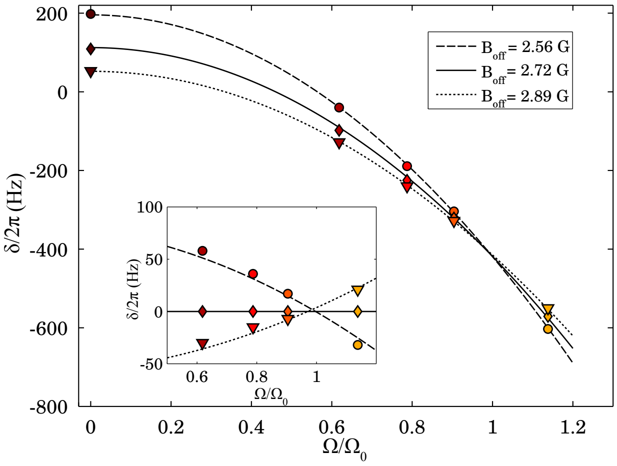

Figure 4: Frequency difference of the clock transition as a function of the Rabi frequency of the dressing for different magnetic fields. The data was extracted from the measurements in Fig. 3. *Inset*: Frequency difference for different offset fields with respect to the measurements at $B_{\text{off}} = 2.72$ G as a function of the Rabi frequency. At the optimal Rabi frequency Ω_0, the three curves show nearly identical frequencies, proving the cancellation of the differential Zeeman shift up to second order.

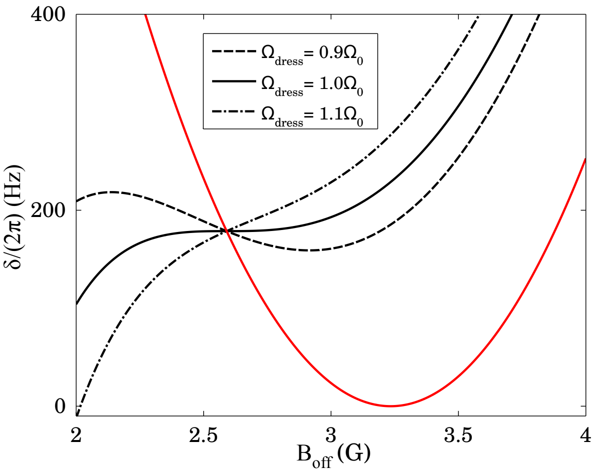

Figure 5: *Double magic* dressing of the qubit states, for which the dependence of the frequency on both the magnetic field and the Rabi frequency disappears around a field value $B_{\text{center}} = 2.59$ G. The calculation assumes a Rabi-frequency imbalance of $\sqrt{6}\,\Omega_{0,\sigma+}/\Omega_{0,\sigma-} = 1.25$, the obtained optimal parameters are $\Omega_0 = 2\pi \times 86.7$ kHz, $\Delta_{\text{dress}} = -2\pi \times 309$ kHz.

Fig. 3 shows that it is possible to generate plateaus where the frequency differs by less than 0.1 Hz over a magnetic-field range of more than 100 mG. As is visible in the inset of Fig. 3, the measurement does not reach this accuracy. We estimate a frequency uncertainty of ±5 Hz, based on the limited time between the Ramsey pulses and the uncertainty of the unstabilized microwave power.

The reduced sensitivity of the clock transition to magnetic-field variations is shown in Fig. 4. Here we plot the measured frequencies and the theory curves for three different offset fields as a function of the Rabi frequency, as extracted from the values in Fig. 4. For the optimum Rabi frequency Ω_0, all three curves show the same AC Zeeman shift. The inset in Fig. 4 shows the frequency difference between the curves measured for the three offset fields with respect to the value $B_{\text{off}} = 2.72$ G. The three curves cross nearly at the same point, showing the strong suppression of the differential Zeeman shift over a field range larger than 0.2 G.

The stability of the microwave power is expected to be the strongest limitation on the frequency stability. In order to reach the 0.1 Hz range at the field point of 2.65 G, a power stability on the order of $\Delta\Omega_{\text{dress}}/\Omega_{\text{dress}} \sim 1 \times 10^{-4}$ would be required. For certain offset fields, however, it is possible to find solutions for Eq. (10) where both the B-field dependency as well as the dependency on the Rabi frequency Ω_{dress} disappear. An example for such a solution can be seen in Fig. 5: Here, we calculate that the transition frequency varies by less than ±0.1 Hz over a range of 100 mG around $B_{\text{center}} = 2.59$ G. At the center of the plateau, the frequency δ becomes independent of the Rabi frequency for a detuning of $\Omega_{\text{dress}} = -2\pi \times 309$ kHz. In a range of ±10 mG around B_{center} a Rabi-frequency stabilization on the order of 1% would be sufficient to reach a level of 0.1-Hz stability. Such *double magic* dressing enables the employment of this technique with on-chip microwave devices, where Rabi frequencies are inversely proportional to the distance to the chip.

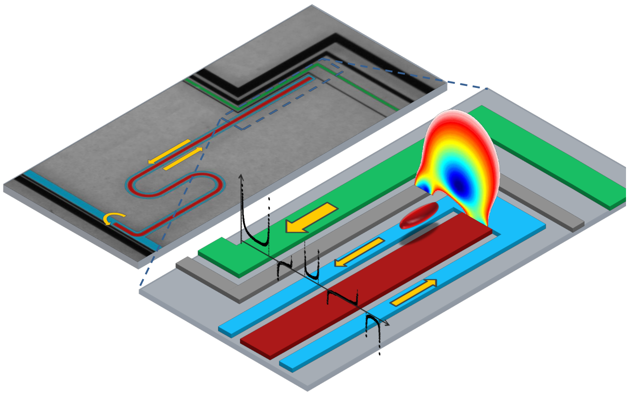

Figure 6: Principle of a CPW resonator consisting of ground planes (blue) and a central conductor (red). Atoms are trapped far away from the surface in a Z-trap formed by the current in the green wire and external fields (not shown), then moved towards the surface by simultaneously reducing the current and the bias field. External magnetic fields induce supercurrents in the resonator, as illustrated by the current distribution curves (black). These fields along with external bias fields form the magnetic trapping potential above the chip [48].

2.2 Microwave cavity as quantum bus

A key component of a hybrid quantum system is the quantum bus that connects the various subsystems. We focus our discussion to microwave resonators, since they are a natural choice in ultracold atom-superconducting qubit systems due to the transition frequencies in the subsystems, the ultrastrong coupling demonstrated to superconducting qubits [39], and finally their well-understood manufacturing technology. We note however, that alternative approaches have also started to emerge recently, e.g. usage of nanomechanical oscillators [82, 83].

Irrespectively of the particular resonator in question, two parameters are crucial: (1) The decay rate κ of the field in the resonator (or equivalently its quality factor defined as $Q \equiv \omega/\kappa$, with ω being the mode frequency), and (2) the field strength generated by a single photon, since these determine if the coupling between the cavity and the quantum subsystem is strong enough.

Early experiments were using macroscopic, three-dimensional bulk superconducting resonators, which is a familiar technology from experimental particle physics. These resonators provide extremely high quality factors, $Q = 10^8 \ldots 10^{10}$ [84], but due to the large mode volume, the field strengths are relatively small. Nonetheless, several experiments have achieved strong coupling between the atoms and the cavity. Superradiance and transient micromaser effect have been demonstrated [69, 85, 86]. Single Rydberg atoms were shot through the cavity, and coherent exchange of microwave photons between the atoms and the cavity were observed [87, 88], demonstrating the quantized nature of the cavity field.

Inspired by the solid-state community, coplanar waveguide resonators (CPW) started to take place in cold atomic research as well. The basic structure is depicted in Fig. 6 [48]. The resonator consists of thin conducting strips deposited on a substrate forming the waveguide structure. Originally they were made of copper

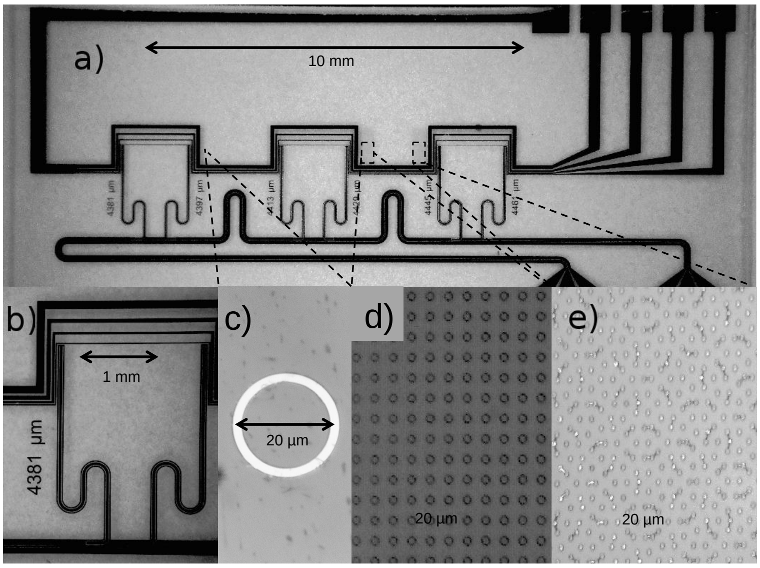

Figure 7: Photo of the atom chip used in experiments [PUB 1] and [PUB 4]. The Z-shaped wires on (a) and (b) are used for trapping purposes. The superconducting ring is shown on (c). For studying periodic and quasiperiodic magnetic lattices the chip also contains Nb-pillars arranged in square lattice (d) and Penrose tiling (e) (not used in our experiments). Photo is taken from [93].

[89] or gold [90], but recently typically superconductors are used to reduce ohmic losses and to suppress thermic Johnson noise [91]. CPW resonators have small mode volumes, therefore offer high field strengths, but possess significantly lower quality factors, $Q = 10^4 \ldots 10^5$ at $T = 4$ K [92].

Naturally, all superconducting resonators must be operated under cryogenic conditions to reach the superconducting transition temperature. For Nb-resonators $T_c = 9.2$ K. In practice, the quality factor of the resonator tumbles significantly at elevated temperatures due to the BCS-resistance [84, 94], therefore it is desirable to cool them to 1 K. A photo of the chip used in experiments [PUB 1] and [PUB 4] is presented in Fig. 7. The resonator is formed by the central conductor and the ground planes (curved structures in Fig. 7(a) and Fig. 7(b)), the Z-shaped wires are for trapping purposes. Since the resonator forms a closed superconducting loop, the flux it encloses is quantized and conserved [95, 96], i.e. any perpendicular external magnetic field is compensated by the induced supercurrents. These effects must be taken into account when designing the trapping above the resonator [48, 97]. To study the effect rigorously, a separate superconducting ring was placed onto the chip, see Fig. 7(c). By freezing different amounts of magnetic flux into the ring, the quantized effect on the resulting trapping potential has been investigated in detail, finding perfect agreement with the predictions [PUB 4].

A key advantage of this CPW approach is that the resonator can be integrated with additional current-carrying thin-layer wires. By properly designing the layout, the currents, and external bias magnetic fields, a magnetic microtrap is formed in the vicinity of the surface [98]. The technique is versatile and extremely precise: atoms can be guided [99] or positioned with sub-micrometer accuracy in all three dimensions [100], can be split [101], or, by forming a magnetic conveyor belt, they

	3D	2D CPW
Size	5cm × 5cm × 5cm	15 μm × 15 μm × 1cm
Mode volume [cm^3]	125	2×10^{-6}
Q	10^8	10^4
κ	68 Hz	680 kHz
E [V/m]	5×10^{-5}	0.34
B [μG]	1.5×10^{-3}	10
E-coupling	1.5 kHz	10 MHz
B-coupling	2 Hz	16 kHz

Table 2: Expected fields and coupling strengths for 3D superconducting and 2D-CPW resonators. The mode frequency is set to $f = 6.8$ GHz. The coupling strength calculations assume a single $n = 50$ Rydberg atom and scaling laws from Tab. 1 (electric case), and a collective enhancement with $N = 10^6$ ground-state atoms (magnetic case). The values Q and κ for CPW resonators are based on in-house measurements [PUB 6].

can be transported on large, macroscopic distances [102, 103]. The resulting *atom chip* is a compact and fully integrated system, it can be used to create ultra-cold mirror MOTs without any additional out-of-the-chip trapping wires [104].

2.2.1 Coupling atoms to cavities

There are two possibilities to couple atoms to microwave fields: either using magnetic dipole transitions in the ground state, or electric dipole transitions between Rydberg states. The achievable coupling strengths can be estimated roughly in the following way. The field strength of single photon confined in an effective V_{eff} volume is

$$E = \sqrt{\frac{\hbar\omega}{2\epsilon_0 V_{\text{eff}}}}. \tag{12}$$

With this the electric coupling strength between two neighbouring Rydberg states $|nS\rangle$ and $|nP_{3/2}\rangle$ is $g_E \approx n^2 a_0 e \cdot E$, while the single-atom magnetic coupling between the cavity and the ground state is $g_B \approx \mu_B B = \mu_B \cdot E/c$. The order of magnitude estimations are summarized in Tab. 2, taking into account a $\sqrt{N}$ enhancement factor for the magnetic coupling when working with a ground-state ensemble.

Although strong collective magnetic coupling between ground state ^{87}Rb and CPW resonators has been proposed theoretically [105], we will pursue coupling via Rydberg states. Indeed, recently magnetic coupling between an ensemble of 10^5 ground-state atoms and a driven CPW resonator has been demonstrated for the first time [PUB 6]. With cavity decay rate $\kappa = 2\pi \times 3$ MHz, and single-atom coupling strength $g = 2\pi \times 0.5$ Hz estimated from simulating the magnetic field of the resonator, the established coupling was weak.

Working with Rydberg atoms in the vicinity of a solid-state surface raises a number of challenges to be solved. First, due to their high polarizability (cf. Sec. 2.1), Rydberg atoms are exceptionally sensitive to electric field noises and stray electric fields. The level shifts and state mixing can be calculated and measured accurately

[106], the results show that for $n = 70$ the Stark shift stops being quadratic and is getting chaotic for fields as low as 2.5 V/cm. As long as the disturbing field is homogeneous, it can be compensated for, but the system is extremely sensitive to any inhomogeneity. Unfortunetely, such inhomogeneities are expected to occur: due to the relation between the ionization energy of the atom and the work function of chip material, atoms tend to get deposited onto the surface, where a dipole layer is formed after a partial electron transfer from the atom to the surface, creating an inhomogenous stray electric field, resulting in a spatially dependent shift [107–109]. The extent of this charge transfer heavily depends on the material properties of the surface which might be used to control this effect [110, 111]. Coating the surface with a bulk layer of rubidium has been shown to be helpful [112], although additional work needs to be done when working with CPW resonators, since the central conductor and the ground planes cannot be shorted. Investigating the Stark maps, it turns out that around certain electric fields the differential shifts between $|nS_{1/2}\rangle$ and $|nP_{3/2}\rangle$ is nearly zero, which seems to be a proper working point. We intend to study this in the future. Another possibility is to dress the Rydberg atoms with microwave fields to modify the polarizabilities, rendering the differential shift to be zero [113].

Another issue is the temperature of the surface. Blackbody radiation induces transitions between neighbouring Rydberg states, severly shortening their lifetime [114]. A systematic study of this effect has been carried out recently [PUB 5], qualitatively confirming the theoretical predictions.

A third challenge is the incoherent thermal population of the microwave mode, reducing the fidelity of existing Rydberg-cavity quantum gates. We address this issue in detail in Sec. 2.3.

2.3 Long-range interaction via a thermal microwave cavity

In recent years, several proposals have been devised about how to realize universal quantum gates in hybrid systems, e.g. [115–118]. A common feature of these protocols is that the microwave cavity mode is assumed to be at practically $T = 0$ K temperature containing initially zero photons. Since the coupling strength between the atoms and the cavity being in a Fock state with n photons is proportional to $\sqrt{n+1}$, at finite temperatures the coupling strength will follow the thermal distribution of the photons $p(n|\bar{n}_{\mathrm{th}}) = \bar{n}_{\mathrm{th}}^{n}/(\bar{n}_{\mathrm{th}} + 1)^{n+1}$, where $\bar{n}_{\mathrm{th}} = (\mathrm{e}^{\hbar\omega/k_B T)} - 1)^{-1}$ is the mean thermal photon number at temperature T. Similarly, the atom-cavity coupling exerts an n-dependent AC-Stark shift onto the atoms. This means that the phase of the atomic dipole after interacting with the cavity for a fixed duration will severely depend on n, causing the overall fidelity of the interaction (summed up to n) dropping below unusable levels.

It is a standard procedure to cool down solid-state systems to $T \simeq 20$ mK using dilution refrigerators. However, it is an extremely challenging engineering task to combine this technology with ultracold atoms [119]. The CPW resonators in state-of-the-art ultracold atom experiments are cooled instead by liquid ^{4}He to $T = 4.2$ K. At this temperature, the cavity is heavily populated from its environment, due to the relatively low mode frequency $\omega \sim 2\pi \times 10$ GHz. At $T = 4.2$ K it contains

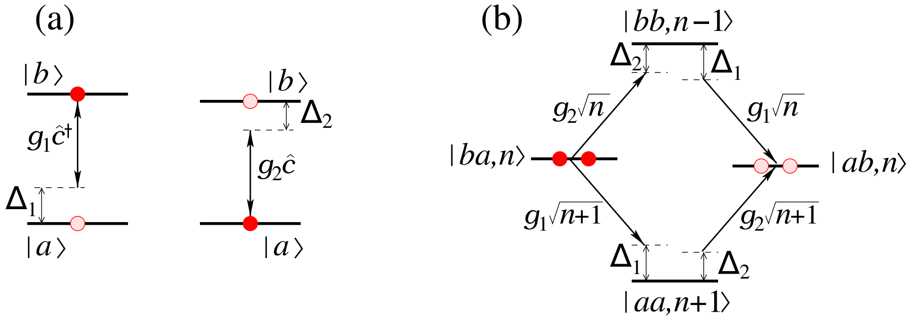

Figure 8: Level scheme of the system. (a) Two atoms with levels $|a\rangle$, $|b\rangle$ are coupled to the cavity field $\hat{c}$ with the coupling strengths g_1 and g_2 and detunings Δ_1 and Δ_2 , respectively. (b) Transitions between states $|ba, n\rangle$ and $|ab, n\rangle$ containing n cavity photons can occur via two paths involving intermediate non-resonant states $|bb, n-1\rangle$ and $|aa, n+1\rangle$.

$\bar{n}_{\text{th}} \sim 10$ thermal photons on average. This is in stark contrast with optical cavities that are in vacuum state even in a room-temperature environment. Therefore it is of crucial importance to develop methods that are compatible with existing cryogenic technology and can handle the constant inflow of thermal photons.

As demonstrated in [120], it is possible to remove thermal photons by shooting Rydberg atoms through the cavity. The atoms absorb the photon, and quite literally take it out from the cavity. This creates a non-equilibrium situation, but since for high-Q cavities ($Q \sim 10^8$) it takes ~ 10 ms for the environment to re-contaminate the cavity mode, this is a working solution. However, for CPW resonators with limited Q-factors this method fails, because the mode is repopulated within ~ 10 μs, which is comparable with the typical timescale to excite Rydberg atoms at all.

We have managed to create two fundamentally different solutions to overcome this problem, as will be discussed in this section. Both of them realize a universal 2-bit quantum gate, mediating interaction between two spatially separated quantum systems via a thermal cavity. Here we only highlight the basic ideas, for detailed discussions see the referred publications.

2.3.1 Continuous cooling with atoms

The first method is based on continuous removal of thermal photons from the cavity. This lowers the effective mode temperature even though the environment is still at $T \simeq 4$ K. By appropriate choice of experimental parameters, the very same mode can be used off-resonantly to mediate interactions between two atomic ensembles, realizing a SWAP or $\sqrt{\text{SWAP}}$ gate [PUB 3].

Let us consider two two-level systems coupled off-resonantly to the same cavity mode $\hat{c}$ with coupling strengths g_1 and g_2, see Fig. 8(a). The detunings are denoted by Δ_1 and Δ_2, respectively. The Hamiltonian of the system in rotating-wave approximation is

$$H = \sum_{i=1,2} \left[\frac{1}{2} \Delta_i (\hat{\sigma}_{bb}^{(i)} - \hat{\sigma}_{aa}^{(i)}) + g_i (\hat{c}\hat{\sigma}_{ba}^{(i)} + \hat{c}^\dagger \hat{\sigma}_{ab}^{(i)}) \right], \tag{13}$$

where $\sigma_{\mu\nu} = |\mu\rangle\langle\nu|$. The system is subjected to several relaxation processes: both Rydberg states in the atoms $|a\rangle$ and $|b\rangle$ decay with rate Γ to some lower state(s) $|s\rangle$ that are decoupled from the cavity field, and the cavity field relaxes to the thermal equilibrium. These processes are described by the following Liouvillian:

$$\mathcal{L} = \mathcal{L}_{a_1} + \mathcal{L}_{a_2} + \mathcal{L}_c, \tag{14}$$

with

$$\begin{aligned}\mathcal{L}_{a_i}\hat{\rho} &= \frac{1}{2}\,\Gamma(2\hat{\sigma}^{(i)}_{sa}\hat{\rho}\hat{\sigma}^{(i)}_{as} - \hat{\sigma}^{(i)}_{aa}\hat{\rho} - \hat{\rho}\hat{\sigma}^{(i)}_{aa}) + \frac{1}{2}\,\Gamma(2\hat{\sigma}^{(i)}_{sb}\hat{\rho}\hat{\sigma}^{(i)}_{bs} - \hat{\sigma}^{(i)}_{bb}\hat{\rho} - \hat{\rho}\hat{\sigma}^{(i)}_{bb})\\ \mathcal{L}_c\hat{\rho} &= \frac{1}{2}\,\kappa(1+\bar{n}_{\mathrm{th}})(2\hat{c}\hat{\rho}\hat{c}^\dagger - \hat{c}^\dagger\hat{c}\hat{\rho} - \hat{\rho}\hat{c}^\dagger\hat{c}) + \frac{1}{2}\kappa\bar{n}_{\mathrm{th}}(2\hat{c}^\dagger\hat{\rho}\hat{c} - \hat{c}\hat{c}^\dagger\hat{\rho} - \hat{\rho}\hat{c}\hat{c}^\dagger).\end{aligned}$$

Here, $\hat{\rho}$ is the density operator of the total system which obeys the master equation $\partial_t\hat{\rho} = -\frac{i}{\hbar}[H,\hat{\rho}] + \mathcal{L}\hat{\rho}$.

Let us consider states $|ba,n\rangle$ and $|ab,n\rangle$. Our goal is to establish coherent Rabi oscillations between these two states with an amplitude and Rabi frequency that are independent from n. We have two excitation paths: either via $|aa,n+1\rangle$ or $|bb,n-1\rangle$, involving a photon addition to or subtraction from the cavity mode, as illustrated in Fig. 8 (b). In order to minimize the detrimental effect of the cavity field relaxation and thermalization, the two subsystems should exchange virtual photons. Therefore we choose the qubit and atom detunings large (and roughly equal): $\Delta_{1,2} \gg |\Delta_1 - \Delta_2|$, $g_{1,2}\sqrt{n_{\max}}$, where $n_{\max}$ is the maximum number of thermal photons that we can expect with reasonable probabilty (typically $n_{\max} \simeq 2 - 10 \times \bar{n}_{\mathrm{th}}$). We now adiabatically eliminate these intermediate states. With $\Delta \equiv \Delta_2$ and $\delta \equiv \Delta_1 - \Delta_2$, for $\Delta \gg \delta$ the detuning $\delta E(n) \equiv E_{ba,n} - E_{ab,n}$ between the two target states and the transition rate $G(n)$ between them is given by

$$\begin{aligned}\delta E(n) &\simeq \delta + \frac{g_1^2 - g_2^2}{\Delta}(2n+1)\\ G(n) &\simeq \frac{g_1 g_2}{\Delta}\left(1 - \frac{\delta}{2\Delta} - \frac{g_1^2 + g_2^2}{\Delta^2}(2n+1)\right),\end{aligned} \tag{15}$$

where we have neglected terms on the order of $\delta\frac{g^2}{\Delta^2}$, $\frac{g^4}{\Delta^3}$ and higher. We thus see that in general both the detuning and the transition rate heavily depend on n. Although in case of $g_1 = g_2$ and for extremely large detunings $\bar{n}_{\mathrm{th}}(g_{1,2}/\Delta)^2 \ll 1$ we do obtain nearly n-independent Rabi-oscillations, for mismatched coupling strengths coherent oscillation is not possible, since the difference between $\delta E(n)$ for various n is on the order of the transition rate G.

If, on the other hand, we could pinpoint the photon distribution to $n = 0$ by reducing the effective photon number in the cavity, we could obtain high-fidelity oscillations. Let us now assume we can indeed remove photons from the cavity with a rate γ_c. This cooling effect is described by the Liouvillian

$$\mathcal{L}'_c\hat{\rho} = \frac{1}{2}\,\gamma_c(2\hat{c}\hat{\rho}\hat{c}^\dagger - \hat{c}^\dagger\hat{c}\hat{\rho} - \hat{\rho}\hat{c}^\dagger\hat{c}). \tag{16}$$

Projecting the master equation to the photon space and introducing $P_n \equiv \langle n|\hat{\rho}|n\rangle$, the probabilty of having n photons in the cavity, the evolution of the field in absence of atoms is described by the following set of equations:

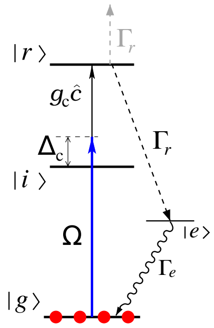

Figure 9: Schematics of the cooling setup. Atoms in the ground state $|g\rangle$ are excited to the Rydberg state $|r\rangle$ by a two-photon transition via intermediate nonresonant state $|i\rangle$. The resonant two-photon transition involves a photon absorption from the laser field acting on the transition $|g\rangle \to |i\rangle$ with Rabi frequency Ω and detuning $\Delta_c \gg \Omega$, and a photon absorption from the cavity field coupled with strength $g_c \ll \Delta_c$ to the Rydberg transition $|i\rangle \to |r\rangle$ detuned by $-\Delta_c$. State $|r\rangle$ decays with rate Γ_r either by ionization or by an induced cascade to state $|g\rangle$ via intermediate state $|e\rangle$ having large decay rate Γ_s.

$$\partial_t P_n = d(n+1)P_{n+1} + anP_{n-1} - dnP_n - a(n+1)P_n, \tag{17}$$

where $a = \kappa\bar{n}_{\text{th}}$, and $d = \kappa(\bar{n}_{\text{th}}+1)+\gamma_c$. The steady-state solution is

$$P_n = \frac{\bar{n}_{\text{eff}}^n}{(1+\bar{n}_{\text{eff}})^{n+1}}, \tag{18}$$

which corresponds to an equilibrium with effective photon number $\bar{n}_{\text{eff}} = \frac{\bar{n}_{\text{th}}}{1+\gamma_c/\kappa}$, i.e. the thermal mean number is reduced by a factor of $(1+\gamma_c/\kappa)$. This means that for $\gamma_c \gg \kappa$ the effective temperature of the mode is indeed significantly lowered.

Removing photons from the cavity can be realized for example by assuming N_c “cooling” atoms in the ground state $|g\rangle$ trapped near a cavity antinode. A laser field acts on the transition from $|g\rangle$ to a Rydberg state $|i\rangle$ with Rabi frequency Ω and (large) detuning $\Delta_c \gg \Omega$, see Fig. 9. Each atom is coupled to the cavity field $\hat{c}$ on the Rydberg transition $|i\rangle \to |r\rangle$ with strength $g_c \ll \Delta_c$. Upon adiabatically eliminating the off-resonant intermediate state we obtain an effective Rabi frequency $\Omega_n^{(2)} = \Omega g_c\sqrt{n}/\Delta_c$ for the two-photon transition $|g,n\rangle \to |r,n-1\rangle$ which involves absorption of a laser photon and a cavity photon. The amplitude $A_{g,n}$ and $A_{r,n-1}$ for states $|g,n\rangle$ and $|r,n-1\rangle$ obey the following equations:

$$\begin{aligned} \partial_t A_{g,n} &= -i\Omega_n^{(2)} A_{r,n-1}, \\ \partial_t A_{r,n-1} &= -\frac{1}{2}\Gamma_r A_{r,n-1} - i\Omega_n^{(2)} A_{g,n}, \end{aligned} \tag{19}$$

where Γ_r is the population decay rate of the Rydberg state $|r\rangle$ and we assume the two-photon resonance. Assuming fast decay $\Gamma_r \gg \Omega_n^{(2)}$, we can set $\partial_t A_{r,n-1} = 0$ and obtain the incoherent transition rate $\frac{1}{2}R_n = \frac{|\Omega_n^{(2)}|^2}{\Gamma_r/2}$ from $|g,n\rangle$ to $|r,n-1\rangle$. With N_c cooling atoms, we can then identify the photon extraction rate via $\gamma_c n = N_c R_n$, leading to $\gamma_c = N_c \frac{4\Omega^2 g_c^2}{\Delta_c^2\Gamma_r}$. Typically the natural decay of Rydberg states is rather slow.

Larger rates can be obtained either by laser-induced or selective-field ionization of $|r\rangle$, which however would continuously deplete the available cooling atoms. A better alternative is to use a laser field with Rabi frequency Ω_r to resonantly couple $|r\rangle$ to a lower excited state $|e\rangle$ that decays back to the ground state with rate $\Gamma_e \gg \Omega_r$. With this, the effective decay of $|r\rangle$ is $\Gamma \simeq \frac{4\Omega_r^2}{\Gamma_e}$.

Let us now estimate the fidelity. Starting from $|ba, n\rangle$ at time $t = 0$, in absence of relaxation, the probabilty for the system to be in state $|ab, n\rangle$ at time t is given by

$$p_{ab,n}(t) = \left|\frac{G(n)}{\bar{G}(n)}\right|^2 \sin^2[\bar{G}(n)t], \tag{20}$$

where $\bar{G}(n) = \sqrt{G(n)^2 + \frac{1}{4}|\delta E(n)|^2}$ is the generalized Rabi frequency. Relaxations lead to exponential damping of the transfer probabilty. The decay of states $|a\rangle$ and $|b\rangle$ introduces a factor of $\mathrm{e}^{-\Gamma t}$. The cavity decay is strongly suppressed by $(g_{1,2}/\Delta)^2$, thus we neglect it for the time being. With this we have the following formula for the transfer probabilty

$$p_{ab,n}(t) = \mathrm{e}^{-2\Gamma t}\left|\frac{G(n)}{\bar{G}(n)}\right|^2 \sin^2[\bar{G}(n)t]. \tag{21}$$

If initially we have a distribution P_n of photon states, the total probabilty is given by

$$p_{ab}(t) = \sum_n P_n p_{ab,n}(t). \tag{22}$$

Turning on the cooling and thus also assuming $\bar{n}_{\text{eff}} \ll 1$ the transfer probability can be estimated as

$$p_{ab}(t) > P_0\, p_{ab,0} = \frac{1}{1+\bar{n}_{\text{eff}}}\,\mathrm{e}^{-2\Gamma t} \times \frac{1}{2}\left(1 - \cos[2G(0)t]\,\mathrm{e}^{-\kappa_{\text{eff}}t}\right), \tag{23}$$

with $\kappa_{\text{eff}} = (\kappa + \gamma_c)\,\frac{g^2}{\Delta^2}$, where $g^2 = \frac{1}{2}(g_1^2 + g_2^2)$. From this we obtain the following estimation for the fidelity:

$$\begin{aligned} F \equiv P_0\, p_{ab,0}(t_{\text{tr}}) &\gtrsim \\ \left[1 - \frac{\kappa\bar{n}_{\text{th}}}{\kappa+\gamma_c}\right]&\left[1 - \frac{\pi}{2}\,\frac{\Gamma\Delta}{g_1 g_2}\right]\left[1 - \pi\,\frac{\kappa+\gamma_c}{4\Delta}\,\frac{g^2}{g_1 g_2}\right], \end{aligned} \tag{24}$$

It is instructive to observe that three conditions are required for obtaining high fidelities:

(i) $\kappa + \gamma_c \gg \kappa\bar{n}_{\text{th}}$, i.e. the cooling rate should be high enough to achieve $\bar{n}_{\text{eff}} \ll 1$.

(ii) $\frac{g_1 g_2}{\Delta} \gg \Gamma$, i.e. the transition rate $G(0)$ should be high enough so that the probabilty of atomic or qubit decay shall be small during the transfer.

(iii) $\Delta \gg \gamma_c + \kappa$, i.e. the cavity field should be strongly detuned to have small thermal population and therefore decay during the transfer.

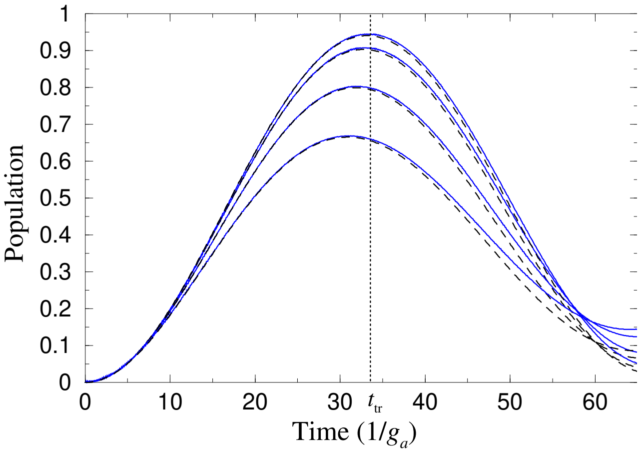

Figure 10: Population of state $|ab\rangle$ for different cooling rates γ_c, as obtined from solving the master equation (solid blue), and from the approximate Eq. (22) (dashed black). The cooling rates are $\gamma_c = (4, 9, 24, 49)\kappa$, corresponding to $\bar{n}_{\text{eff}} = (1.0, 0.5, 0.2, 0.1)$ for the graphs with progressively larger amplitudes. The dotted vertical line indicates time $t_{\text{tr}} = \frac{\pi}{2G(0)}$, when the population of $|ab, 0\rangle$ is peaked. Other parameters: $\Delta = 30g_2$, $\delta = \frac{g_2^2 - g_1^2}{\Delta}$, $\kappa = 10^{-3}g_2$, $\bar{n}_{\text{th}} = 5$, $\Gamma = 3 \times 10^{-4}g_2$, $g_1 = 1.4g_2$.

We have confirmed the validity of this theory by exact numerical simulations. Since the photon distributions is now highly peaked around $n = 0$, we choose $\delta = \frac{g_2^2 - g_1^2}{\Delta}$ to satisfy $\delta E(0) = 0$ in Eq. (15), and the transfer time as $t_{\text{tr}} = \frac{\pi}{2G(0)}$. We indeed observe coherent Rabi oscillations with enhanced fidelity as the effective photon number is gradually reduced with higher cooling rates, as can be seen in Fig. 10.

2.3.2 Temperature-resistent quantum gate

The second possibility is that we do not even try to remove the thermal photons, but instead come up with a scheme that is simply resistant against their detrimental effect. The scheme is inspired by the work of Sørensen and Mølmer [121, 122], and relies on a destructive quantum interference between multiple excitation pathways. We only recall here the basic ideas, for full discussion see [PUB 2].

Let us have two identical atoms with ground state $|g\rangle$ and a Rydberg state $|r\rangle$, as illustrated in Fig. 11. The atoms interact non-resonantly with a common cavity mode via the dipole-allowed microwave transitions to adjacent Rydberg states $|a\rangle$ and $|b\rangle$ with coupling strengths $g_{\text{a,b}}$. Two excitation lasers with optical frequencies $\omega_{1,2}$ and Rabi frequencies $\Omega_{1,2}$ act on the transitions $|g\rangle_1 \to |a\rangle_1$ and $|g\rangle_2 \to |b\rangle_2$. The detunings with respect to the corresponding atomic states are denoted by $\delta_{1,2}$.

The Hamiltonian of the system is

$$H = \omega_c \left(\hat{c}^\dagger \hat{c} + \frac{1}{2} \right) + \sum_{i=1,2} \left[H_{\text{a}}^{(i)} + V_{\text{ac}}^{(i)} + V_{\text{al}}^{(i)} \right], \tag{25}$$

where ω_c is the cavity mode frequency, $H_{\text{a}}^{(i)} = \sum_\mu \omega_\mu |\mu\rangle_i \langle\mu|$ is the Hamiltonian of the unperturbed atom i ($\mu = g, r, a, b$), $V_{\text{ac}}^{(i)} = g_a \hat{c}\, |a\rangle_i \langle r| + g_b \hat{c}^\dagger\, |b\rangle_i \langle r| + \text{h.c.}$

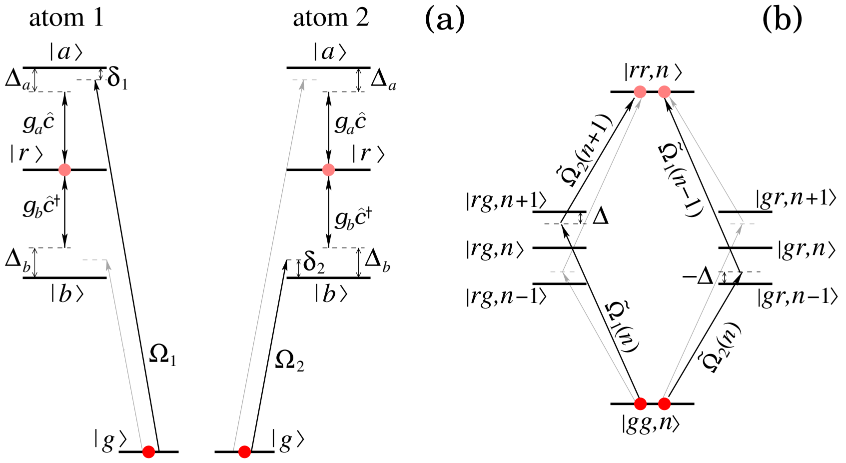

Figure 11: (a) Level scheme of two atoms interacting with the cavity field on the Rydberg transitions $|r\rangle \leftrightarrow |a\rangle, |b\rangle$ with strengths $g_{a,b}$ and driven by the laser fields with Rabi frequencies $\Omega_{1,2}$ on the transitions from the ground state $|g\rangle$ to states $|a\rangle, |b\rangle$. (b) Under appropriate conditions (see text for details), there are two interfering excitation pathways from the two-atom ground state $|gg,n\rangle$ to the double-excited Rydberg state $|rr,n\rangle$, which cancel the dependence of the total transition amplitude $\bar{\Omega}$ on the cavity photon number n.

describes the atom-cavity interactions, and $V_{\mathrm{al}}^{(1)} = \Omega_1 \mathrm{e}^{-i\omega_1 t} |a\rangle_i\langle g| + \mathrm{h.c.}$ and $V_{\mathrm{al}}^{(2)} = \Omega_2 \mathrm{e}^{-i\omega_2 t} |b\rangle_i\langle g| + \mathrm{h.c.}$ describe the laser drivings of atoms 1 and 2, respectively.

Our aim is to achieve coherent oscillations between the collective states $|gg,n\rangle$ and $|rr,n\rangle$ with maximal amplitude and oscillation frequency which do not depend on n. Assuming $\Omega_{1,2} \ll \delta_{1,2}$, we adiabatically eliminate intermediate states $|a\rangle_1$ and $|b\rangle_2$, obtaining the two-photon Rabi frequencies $\tilde{\Omega}_1(n) = \frac{\Omega_1 g_a \sqrt{n+1}}{\delta_1}$ and $\tilde{\Omega}_2(n) = \frac{\Omega_2 g_b \sqrt{n}}{\delta_2}$ on the transitions $|gg,n\rangle \to |rg,n+1\rangle$ and $|gg,n\rangle \to |gr,n-1\rangle$. These processes are accompanied by addition and removal of a single cavity photon, respectively. If we now choose the two-photon detunings $\Delta_{1,2}$ of $|rg,n+1\rangle$ and $|gr,n-1\rangle$ to have equal magnitude, but opposite sign $\Delta_1 = -\Delta_2 \equiv \Delta \gg \tilde{\Omega}_{1,2}$, we can also eliminate these intermediate states to obtain a resonant multiphoton transition between $|gg,n\rangle$ and $|rr,n\rangle$ involving two laser photons and an exchange of a virtual cavity photon between the two atoms. The resulting effective Rabi frequency is

$$\bar{\Omega} = \frac{\tilde{\Omega}_1(n)\tilde{\Omega}_2(n+1)}{\Delta_1(n)} + \frac{\tilde{\Omega}_2(n)\tilde{\Omega}_1(n-1)}{\Delta_2(n)} = \frac{\Omega_1\Omega_2 g_a g_b}{\delta_1\delta_2\Delta}. \tag{26}$$

However, here $\Delta_{1,2}$ both depend on n via the Stark shifts caused by the coupling to the cavity. The central question is how to choose the experimental parameters ($\omega_{1,2}$, $\Omega_{1,2}$, $\delta_{1,2}$, $g_{a,b}$, and $\Delta_{a,b}$) to indeed keep the multiphoton transition resonant, to achieve $\Delta_1(n) = -\Delta_2(n)$, and to eliminate the n-dependence from them at the same time.

Performing a fourth order perturbation calculation in the laser and cavity couplings, we have established that the following constraints must be satisfied:

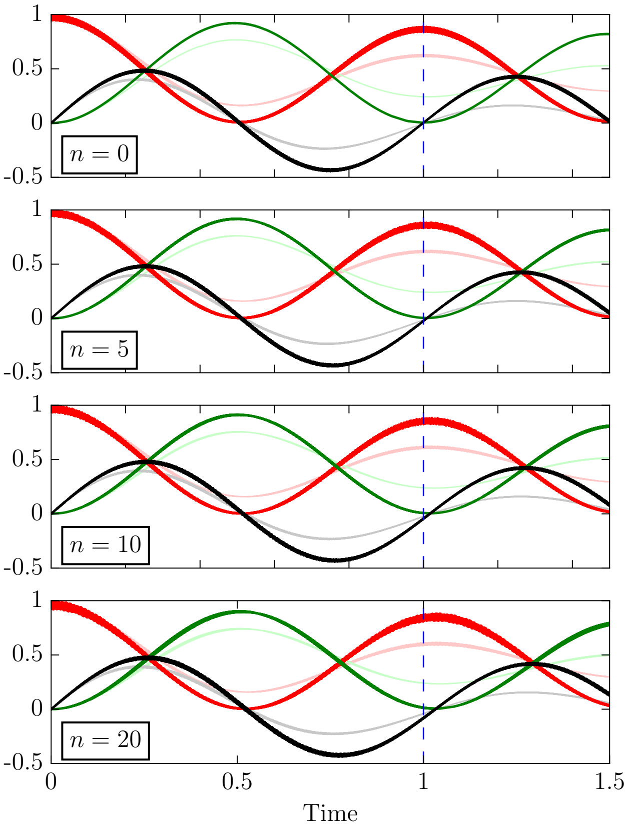

Figure 12: Rabi oscillations between $|gg, n\rangle$ and $|rr, n\rangle$ for cavity photon numbers n = 0, 5, 10, 20. Thick lines show coherent oscillations of populations $\rho_{gg,gg} = \langle gg|\hat{\rho}|gg\rangle$, $\rho_{rr,rr} = \langle rr|\hat{\rho}|rr\rangle$, and coherence $\rho_{gg,rr} = \langle gg|\hat{\rho}|rr\rangle$ for Rydberg state decay $\Gamma = 0.142\,[\bar{\Omega}(0)/2\pi]$ and no dephasing, $\gamma = 0$, while thinner lines show the same quantities for large dephasing $\gamma = 0.4\,[\bar{\Omega}(0)/2\pi]$. Parameters are $\Omega_1 = 56.50$, $\Omega_2 = 60.00$, $\delta_1 = 663.8$, $\delta_2 = -742.0$, $g_a = 9.5$, $g_b = 10.0$, $\Delta_a = 722.0$, $\Delta_b = 800.0$ ($\times 2\pi$ MHz), leading to $\bar{\Omega}(0) \approx 2\pi \times 21.1$ kHz. Time is in units of $[2\pi/\bar{\Omega}(0)]$.

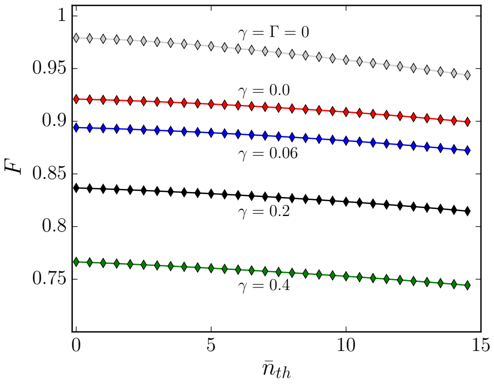

Figure 13: Transfer fidelity F at time $t_\pi = \pi/\bar{\Omega}(0)$ vs. the mean number $\bar{n}_{\text{th}}$ of thermal photons in the cavity, for dephasing rates $\gamma = 0, 0.06, 0.2, 0.4$ and decay rates $\Gamma = 0$ (uppermost curve) and $\Gamma = 0.142$ (all other curves), in units of $[\bar{\Omega}(0)/2\pi]$. Other parameters as are in Fig. 12.

$$\frac{g_a^2}{\Delta_a} = \frac{g_b^2}{\Delta_b}, \tag{27}$$

$$\frac{g_a \Omega_1}{|\delta_1|} = \frac{g_b \Omega_2}{|\delta_2|}, \tag{28}$$

$$|\Delta_a - \Delta_b| \gg g_a g_b \left| \frac{n+1}{\Delta_b} - \frac{n}{\Delta_a} \right|, \quad \text{for } n < n_{\max}, \tag{29}$$

where $n_{\max}$ is the maximal possible thermal photon number given by the temperature of the cavity. Respecting these equations the leftover four-photon detuning scales as $S_{\text{rr}} = \frac{g_a^4 n^2}{\Delta_a^3}$ which is negligible, and the n dependence of the effective Rabi frequency is highly suppressed, $\bar{\Omega}(n) \approx \bar{\Omega}(0)\,(1 - \frac{g_a^2}{\Delta_a^2} n)$. These results have been confirmed by exact numerical simulations, the results of which are shown in Fig. 12. We have also taken into account the most relevant decaying and dephasing processes using standard Liouvillians [123] with Lindblad generators $\hat{L}_\nu^{(i)} = \sqrt{\Gamma}\,|g\rangle_i\langle\nu|$ for the decaying of the states $\nu = r$, a, b, and $\hat{L}_g^{(i)} = \sqrt{\gamma/2}\,(|g\rangle_i\langle g| - \sum_\nu |\nu\rangle_i\langle\nu|)$ for the dephasing with respect to the ground state with rate γ. We observe that although the oscillations are damped by atomic decay and dephasing, the amplitude and frequency are remarkably stable with increasing temperatures.

The fidelity of the transfer defined as $F = \sum_n p(n|\bar{n}_{\text{th}})\,\langle rr, n|\hat{\rho}(t_\pi)|rr, n\rangle$ at time $t_\pi = \pi/\bar{\Omega}(0)$ is plotted in Fig. 13 for various dephasing rates γ and mean thermal photon numbers $\bar{n}_{\text{th}}$. While dephasing indeed has a detrimental effect on the transfer fidelity, it only weakly and nearly linearly depends on $\bar{n}_{\text{th}}$, due to the slight decrease of the effective Rabi frequency $\bar{\Omega}(n)$ discussed above. This can be compensated for by appropriately correcting the transfer time t_π if $\bar{n}_{\text{th}}$ is approximately known.

The effect of dephasing can be suppressed by increasing $\bar{\Omega}(0)$, therefore the maximum attainable value is an important parameter. We assume that it is limited by the cavity couplings $g_{a,b}$, since the laser Rabi frequencies can be collectively enhanced in the superatom regime (cf. Sec. 2.1). With $\eta = |\delta_2|/\Omega_2 \gg 1$ and

$\bar{\eta} = |\Delta_1|/\bar{\Omega}_1 \gg 1$ for each $n \lesssim n_{\max}$, we obtain $\bar{\Omega}_{\max} < \frac{g_b}{\eta\bar{\eta}\sqrt{n_{\max}+1}}$. As an estimate, assuming $g_{a,b} = 2\pi \times 10$ MHz, $\eta, \bar{\eta} = 10$, and a cavity mode with $\omega_c = 2\pi \times 15$ GHz at $T = 4$ K, leading to $n_{\max} \approx 2\bar{n}_{\text{th}} \approx 10$, we have $\bar{\Omega}_{\max} \approx 2\pi \times 30$ kHz.

Since every single-photon and two-photon coupling is off-resonant in the scheme, Rabi oscillation occurs if and only if the two atoms are in the same state initally. By keeping the coupling lasers on for time $t_{2\pi} = 2\pi/\bar{\Omega}$, a complete Rabi cycle will be driven on the transition $|gg\rangle \leftrightarrow |rr\rangle$, resulting in a sign-change of $|gg\rangle$. This transformation corresponds to a universal two-bit CPHASE gate [16, 123]. With this we have indeed established a flexible framework for quantum computation in a thermal environment. Each atom with long-lived hyperfine ground-states $|g\rangle$ and $|s\rangle$ encodes a qubit. Gate operation can be performed on any pair of atoms within the cavity by addressing them with coupling lasers $\Omega_{1,2}$. The physical distance of the atoms is of no importance, as long as they are coupled to the same cavity mode, meaning that there is no restriction on the geometrical arrangement of qubits.

The presented methods allow us to perform hybrid quantum gates with Rydberg atoms in existing 4 K setups, which is of great practical interest, since at the time of writing this thesis, no existing 100 mK setups suitable for ultracold atomic experiments are available, to the best of our knowledge. The long-range nature of the gates promises efficient scalability of the system. Indeed, coupling multiple atomic clouds to the same cavity mode, the corresponding 2-bit gates can be executed on any pairs of clouds, irrespectively of their physical separation. This is in strong contrast with existing Rydberg atom-based gates, where the quickly decaying dipole-dipole interaction allows only nearest-neighbour atoms to interact.

The fidelity of the proposed gates is determined by the relation between the effective Rabi frequency and the decay rate of the Rydberg states. It can be improved by either increasing the gate speed or the lifetime of Rydberg states. For the former, the coupling strength between the resonator and the atom should be enhanced by utilizing higher Rydberg states. For the latter, proper thermal shielding is beneficial, since it suppresses black-body radiation. Furthermore, circular Rydberg states can be used in the first gate. Their exceptionally long lifetimes eliminate this source of infidelity. The second gate is slow by construction. Next to the aforementioned points of improvement, performance can be significantly increased by reducing the intermediate detuning Δ, analogously to the fast-gate regime of the Sørensen-Mølmer ion gate [124].

The microwave dressing scheme, and in particular double magic dressing provides the possibility of noise-insensitive quantum memories. By coherently mapping the Rydberg states to hyperfine ground states, quantum information can be stored in the same atoms that were used for performing the gate operation, hence leading to an integrated, chip-based, $T = 4$ K temperature quantum architecture capable of processing and storing quantum information.

As a further development, one could think about realizing coherent microwave-to-optical photon conversion with the atoms [53, 54], which would also allow coherent quantum communication between distant systems.

3 Optical lattice clocks

Frequency is by far the one physical quantity that can be determined with the highest accuracy [125]. Portable hydrogen masers [126] and chip-scale caesium atomic frequency references are commercially available [127, 128], and it is difficult to overestimate their role in modern technology, such as satellite synchronization and navigation [129], telecommunication [130] or defence industry. They are of fundamental interest in metrology, the very definition of the SI second is based on atomic frequency references: the second is defined as the duration of 9 192 631 770 periods of the radiation corresponding to the transition between the two hyperfine levels of the ground state of the ^{133}Cs atom at $T = 0$ temperature [131]. State-of-the-art caesium fountain clocks have a stability of $\sim 1 \times 10^{-16}$, therefore the accuracy of the second is per definitionem limited to this level. Still, time is defined with the lowest uncertainity among all the SI units.

Atomic clocks using trapped ions with optical clock transitions have been proposed in the '70s [132], and by 2008 ion clock frequencies have been tested against each other with a total uncertainty of $\sim 5 \times 10^{-17}$ after three hours of averaging [133].

Due to the strong Coulomb interaction between ions, ion clocks usually operate with a single trapped particle, which poses a major limitation to the stability due to the quatum projection noise [134]. Therefore, ensembles of neutral atoms with ultranarrow transitions suitable for spectroscopic measurements (alkaline-earth and alkaline-earth-like elements, such as ytterbium) have been investigated for metrological purposes, but their usefulness was severly limited in free space by gravity, residual Doppler shifts arising from an imperfect wavefront of the probe beam, and atom-atom collisions [135–137]. On the other hand, trapping the atoms in an optical dipole trap would have caused uncontrolled Stark shifts. The breakthrough was the concept of *magic wavelength* trapping: by properly choosing the trap wavelength and polarization, the differential Stark shift of the the clock states could be greatly suppressed [138]. The first demonstration of a neutral strontium-based optical lattice clock followed shortly [139], and due to the ongoing research and development, by now they are in direct competition with ion clocks. The stability of neutral atom-based optical frequency standards have now reached the 5×10^{-19} level after one hour interrogation [140], and they are currently used to detect the effects of special [141] and general relativity in a laboratory environment, such as relativistic geodesy [142] or gravitational waves [143], to measure atom-surface interactions [144], or to test the constancy of the fundamental constants of nature [145, 146].

In this section, we describe our efforts to build the first clock experiment at the University, in cooperation with Prof. Hidetoshi Katori (University of Tokyo). We present the conceptual improvements we have proposed to push the performance of neutral atom optical lattice clocks even further. Apart from the fundamental research goals, the secondary aim of the project is to provide a stable, absolute, and narrow-line optical frequency reference system, which is essential for the Rydberg quantum information research presented in the previous section. This work describes a work in progress, the first publications are yet to be submitted.

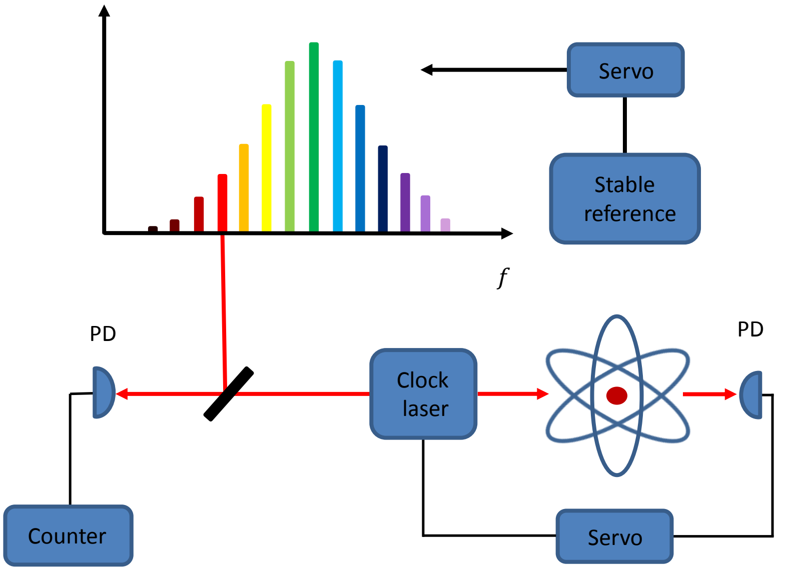

Figure 14: Principle of operation of a passive atomic clock. Atoms are interrogated with the clock laser. using the spectroscopic signal, the laser is frequency stabilized to the clock transition. The frequency comb is stabilized to a reference oscillator (e.g. caesium reference), then the beat signal between the comb and the clock laser is detected and counted.

3.1 State-of-the-art

The operation principle of atomic optical clocks is depicted in Fig. 14. Atoms are laser-cooled and trapped in a magic wavelength optical lattice. The clock transition with frequency f_0 and linewidth Δf_0 serves as stable frequency standard. Our goal is to measure this frequency against some reference. For this purpose first a highly phase-coherent local oscillator (the *clock laser*) is frequency-stabilized to the clock transition. This is ususally achieved by performing either Rabi or Ramsey spectroscopy [147], and then the spectroscopic signal is used to create a feedback loop to control the laser frequency.

If the reference and clock frequencies happen to be almost equal, the measurement can be finished by counting their beat signal directly. However, this is typically not the case, in fact there is a $4-5$ orders of magnitude difference between the primary microwave standards and the optical clock frequencies that needs to be bridged. In certain special cases this can be achieved with longish frequency chains [148, 149].

Since the development of optical frequency combs the experimental complexity of the task has been greatly reduced [150]. The comb is essentially a pulsed laser, the spectrum of which has the form $f_n = f_{\mathrm{CEO}} + n \cdot f_{\mathrm{rep}}$. With proper design, the comb may have modes in the microwave and the UV-VIS range at the same time. Here, f_{CEO} is the carrier-envelope offset frequency, and f_{rep} is the repetition rate of the comb, typically lying in the 100 MHz – 10 GHz range. Usually they are two independent parameters, although in certain combs one of them is fixed by design (offset-free combs [151]). By stabilizing the comb to a stable radio frequency or microwave reference oscillator (e.g. caesium standard) and forming the beat signal between the appropriate comb mode and the clock laser, the clock laser is referenced against the reference oscillator, enabling its frequency to be measured. The frequency comb may also be used to test two different optical clocks against each other. In order to do this, the comb is stabilized to one of the clock transitions instead of a microwave standard. The accuracy of such measurements is determined by the superior stability of the optical clocks instead of the microwave standards.

Let us now investigate the properties of strontium as well as the standard workflow with them [139, 152, 153] in order to be able to identify the possibilities for improvement. For simplicity, we focus on the bosonic ^{88}Sr isotope.

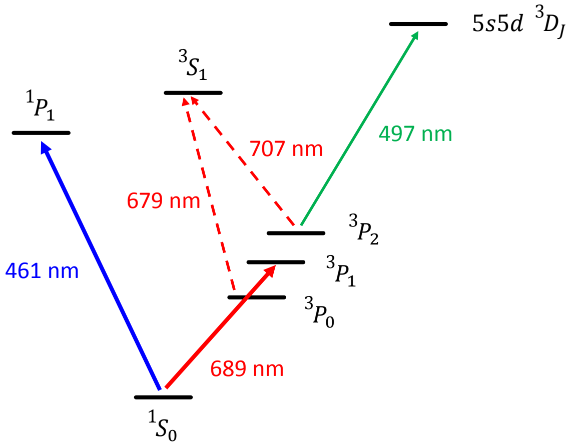

Figure 15: Atomic levels of strontium involved in laser cooling. Magneto-optical traps are operated on the transitions denoted by solid lines, dashed lines denote the repumpers.

Strontium (and alkaline-earth elements in general) facilitate multiple transitions suitable for laser cooling, as illustrated in Fig. 15. The basic properties of the transitions are summarized in Tab. 3.

In order to achieve a sufficient flux of ultracold ($\sim 2\mu$K) atoms, multiple cooling steps have to be utilized. First, a MOT operated on the $5s^2\,^1S_0 \rightarrow 5s5p\,^1P_1$ transition (461 nm) is loaded from a Zeeman slower. Due to the broadness of the transition the typical magnetic gradient is $\sim$ 50 G/cm. The MOT can be operated without any repumping, since the transition is “almost” closed, see Sec. 3.2. However, without repumping a fraction of atoms ends up in the metastable $5s5p\,^3P_2$ state, removing them from the cooling cycle. To prevent this, the $5s5p\,^3P_0 - 5s6s\,^3S_1$ and $5s5p\,^3P_2 - 5s6s\,^3S_1$ are usually also driven with 679 nm and 707 nm lasers, res-

Transition	$\Gamma\ (/2\pi)$	λ [nm]	I_{sat}	T_{Doppler}	T_{recoil}	v_c
$5s^2\,^1S_0 - 5s5p\,^1P_1$	32 MHz	461	42.7 mW/cm^2	770 μK	1 μK	15 m/s
$5s^2\,^1S_0 - 5s5p\,^3P_1$	7.6 kHz	689	3 μW/cm^2	180 nK	460 nK	5 cm/s
$5s5p\,^3P_2 - 5s5d\,^3D_3$	8.7 MHz	497	9.3 mW/cm^2	210 μK	880 nK	4 m/s
$5s5p\,^3P_2 - 5s4d\,^3D_3$	54 kHz	2923	0.3 μW/cm^2	1.3 μK	25 nK	16 cm/s

Table 3: Basic properties of the cooling transitions. Data are taken from [152, 154]. The capture velocities are calculated as $v_c = \Gamma/k$.

pectively. The temperature of the cloud in the blue MOT is $\sim 1-2$ mK. Since this is still too high for the narrow $5s^2\,{}^1S_0 \rightarrow 5s5p\,{}^3P_1$ transition to capture, an intermediate cooling step is necessary to lower the temperature. For this purpose, one can use either the $5s5p\,{}^3P_2 \rightarrow 5s5d\,{}^3D_3$ transition (497 nm) or one can drive the $5s^2\,{}^1S_0 \rightarrow 5s5p\,{}^3P_1$ transition (689 nm) with a frequency-broadened laser. Finally, the field gradient is lowered to $\sim 5-10$ G/cm and the narrow-line MOT is operated on the $5s^2\,{}^1S_0 \rightarrow 5s5p\,{}^3P_1$ transition, leading to a typical temperature of $1\,\mu$K. Finally the atoms are loaded to an optical lattice operated on the magic wavelength at 813 nm to perform the clock spectroscopy on the $5s^2\,{}^1S_0 \rightarrow 5s5p\,{}^3P_0$ transition in the Lamb-Dicke regime, and the clock frequency is measured as discussed above. We note that in absence of nuclear magnetic momentum in ^{88}Sr ($I=0$), the clock transition is dipole-forbidden. Finite transition amplitude can be induced by external magnetic fields causing a state-mixing [155]. Oftentimes, the fermionic ^{87}Sr isotope is used instead which has a magnetic moment $I = 9/2$ and with this a naturally allowed clock transition with a linewidth of ~ 1 mHz [153].

A central quantity describing the stability of clocks is the *Allan-deviation* [156]. Let us denote the clock laser frequency by f_{LO}, and the transition frequency of the system by f_c (this may not be equal to the atomic f_0 due to systematic errors). Assuming we can measure the fractional frequency difference $y \equiv (f_c - f_{\mathrm{LO}})/f_0$, the Allan-deviation σ_y is defined as

$$\sigma_y^2(M) = \frac{1}{2(M-1)} \sum_{i=1}^{M} [\langle y\rangle_{i+1} - \langle y\rangle_i]^2, \tag{30}$$

where $\langle y\rangle_i$ is the ith measurement of the average fractional frequency difference. Under reasonable assumptions [134], we arrive to the following formula:

$$\sigma_y(\tau) = \frac{\eta}{2\pi Q \cdot \mathrm{S/N}} \sqrt{\frac{T_c}{\tau}}, \tag{31}$$

where $Q \equiv f_0/\Delta f_0$ is the quality factor of the clock transition, S/N is the signal-to-noise ratio of the detection, T_c is the cycle-time of the clock, and τ is the total elapsed time. For quantum projection noise limited measurements the S/N ratio scales as $\sqrt{N}$ where N is the number of atoms participating in the measurement. This is precisely what makes neutral atom lattice clocks competitive with ion clocks.

The performance of neutral atom optical clocks is limited by several factors. The most significant systematic uncertainty is caused by the black-body radiation (BBR), which couples non-resonantly to the clock states, shifting the clock frequency [157]. The uncertainty can be reduced by measuring and controlling the temperature of the environment [158], operating the clock under cryogenic conditions [159], or by turning to atomic species that are more resistent against BBR-shifts (e.g. Hg, Cd) [160].

The main limitation for the stability of neutral atom optical lattice clocks originates from their cyclic operation principle [147] which creates a two-fold problem. First, according to Eq. (31) the instability scales as $\sqrt{T_c/\tau}$. Each operation cycle lasts $T_c = t_m + t_p$ time: first the preparation of the new atomic cloud takes up t_p seconds, and the useful measurement time is t_m. For a typical neutral atomic clock system $T_c \sim 1$ s, $t_m \sim 300$ ms $< t_p$, therefore most of the operation time is "wasted" on preparation. Additionally, stability is limited by the *Dick effect* [161]. Essentially, by sampling the short-term fluctuations of the clock laser with the cycle frequency, these instabilities are down-converted to low-frequency noise deteriorating the long-term stability. The precise impact on the clock stability depends on the amount of dead-time, the interrogation method (Rabi or Ramsey), and the exact noise spectrum of the clock laser [161, 162]. This is by far the most severe limitation to the stability: in principle, assuming $N = 10^5 - 10^6$ atoms participating in the clock measurement, the stability should reach a few times $10^{-18}/\sqrt{\tau}$ [138, 163], while the Dick limit is lying at $\sim 10^{-15}/\sqrt{\tau}$ [164], i.e. current performance is two to three orders of magnitude behind the predicted potential. Therefore, it is of crucial importance to combat this effect.

One obvious point for improvement is to reduce the phase fluctuation of the clock laser. To do this, lasers have been stabilized to specially designed long cavities made of ultralow expansion materials, carefully isolated from thermal and mechanical perturbations [165, 166]. To suppress the Brownian motion of the mirror coatings cryogenic cavities have been developed [167], and recently crystalline coating materials have been utilized [168]. The lowest linewidth reported to date is below 40 mHz using a piece of single-crystal silicon cooled to 120 K as the laser cavity, reducing the Dick limit to $\sim 10^{-16}\sqrt{T_c/\tau}$ [169].

Another strategy for mitigation is to optimize the clock cycle [170], or to lock the clock laser to two atomic ensembles to obtain an interleaved, dead-time free interrogation [171]. By turning to non-destructive detection in the clock spectroscopy, the dead-time can be reduced since atoms can be "reused" [172]. In case of comparing two optical clocks, interrogating them with the same laser with a small delay has been demonstrated to surpass the Dick limit [163].

3.2 Towards a continuous optical lattice clock

Our research is addressing the cycle problem in a more fundamental way. Instead of seeking for shortcuts, we have proposed a novel cooling principle, which we call the *core-shell MOT*, to produce a continuous stream of ultracold strontium atoms trapped in a moving optical lattice. By performing interruption-free clock spectroscopy without any cycles and dead-time, the Dick effect would be completely eliminated.

As opposed to "traditional" cooling schemes, where two cooling steps are performed sequentially at the same physical place, in our scheme the situation is reversed: we apply two cooling stages simultaneously but separated in space, as illustrated in Fig. 16b.

The collection and pre-cooling of atoms is realized in the outer shell with a broad-line cooling. The inner volume, the "core", is used for the final narrow-line cooling. One must choose the cooling transitions and other experimental parameters in a way that a hot atom entering the shell from outside slows down enough, so that upon entering the core region, the narrow-line MOT can capture and further cool it to ultra-low temperatures. Finally, we aim to extract the atoms from the core with a moving optical lattice operated at the magic wavelength.

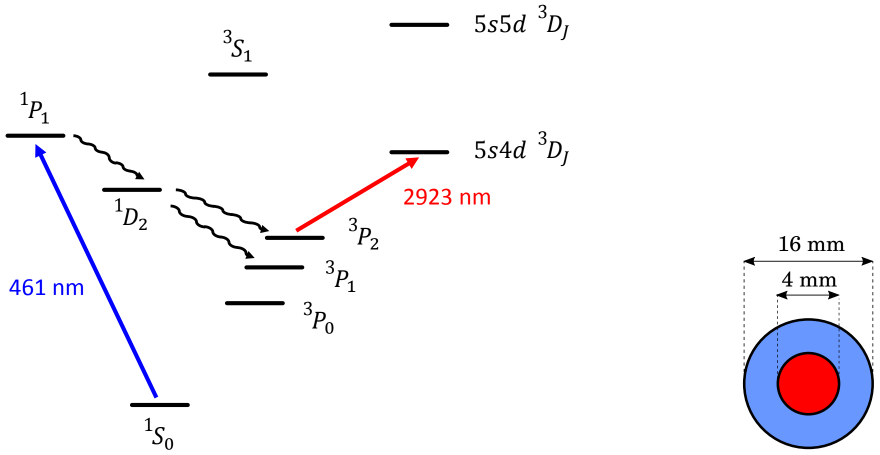

(a) Atomic states involved in the core-shell MOT

(b) Structured beam used for the core-shell MOT

Figure 16: Operation principle of the core-shell MOT

After considering several possibilities, the most promising choice of cooling transitions is depicted in Fig. 16a. We use the $5s^2\,{}^1S_0 \to 5s5p\,{}^1P_1$ transition in the shell, and make use of the fact that the transition is not completely closed. Indeed, atoms in the ${}^1P_1$ state may not only decay to the ground state, but also to the $5s4d\,{}^1D_2$ state with a rate of $\gamma_0 = 2\pi \times 620\,\mathrm{s}^{-1}$. This is $\sim 5 \times 10^4$ times smaller than the decay back to the ground state. From the ${}^1D_2$ state, atoms decay further into ${}^3P_1$ and ${}^3P_2$ states. The former decays back to the ground state, the latter is a metastable state with a lifetime of $\gamma = 500$ s. The effective accumulation rate for this state is $\gamma_{\mathrm{eff}} = (14\,\mathrm{ms})^{-1}$ [173]. This is a reasonable compromise: it is large enough to have an appreciable accumulation speed, but also small enough so that hot atoms can scatter enough photons from the blue transition to be pre-cooled.

In the absence of any repumping, once in the ${}^3P_2$ state, atoms are dark for the blue transition and will leave the shell. Upon entering the core region, they are further cooled on the $5s5p\,{}^3P_2 \to 5s4d\,{}^3D_3$ transition at 2923 nm. Note that the capture velocity of this is transition is three times larger as that of $5s^2\,{}^1S_0 \to 5s5p\,{}^3P_1$, see Tab. 3.

There have been attempts recently to realize core-shell cooling [174, 175], but they were unable to reach ultra-low temperatures for a simple reason: the authors have used the standard blue and red transitions for cooling. Since they share a common level (the ground state), scattered photons from the continuously operated blue transition heated up the cloud to the usual blue temperature. The situation is entirely different in our case, since the two transitions are independent.

Since the broad and narrow-line cooling steps require magnetic field gradients that differ by ~ 1 order of magnitude, we have built a special coil system delivering the field profile shown in Fig. 17. The system consists of two pairs of overlapping Helmholtz coils. The homogeneity of the field in the core region is better than 1 %, and is ramped up to 50 G/cm in the shell region.

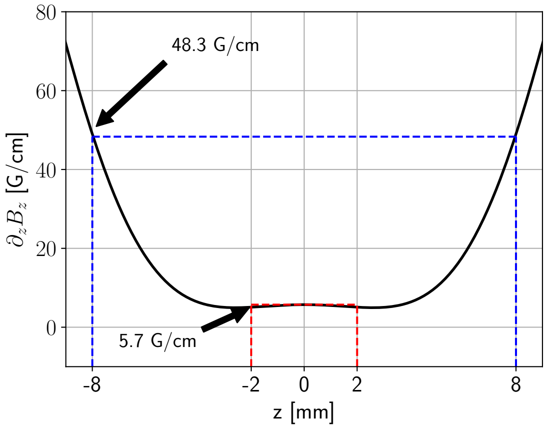

Figure 17: Magnetic field gradient along the strong axis. The core region extends from $z = -2 \ldots 2$ mm, the total beam diameter is 16 mm.

Experimental setup To date a basic setup has been developed and installed, allowing us to perform laser cooling on the $5s^2\,{}^1S_0 \rightarrow 5s5p\,{}^1P_1$ transition, and to perform spectroscopic measurements to calibrate the laser system and to measure the basic properties of the MOT.

Laser system The 679 nm and 707 nm repump lasers are grating-stabilized extended-cavity diode lasers (ECDL). The 461 nm cooling laser is frequency doubled from a 922 nm tapered amplifier (TA) ($P_{\mathrm{max}} = 2$ W) using a fiber-coupled ridge-waveguide periodicly-poled lithium niobate crystal (PPLN) from NTT Electronics. The TA is seeded from a grating-stabilized ECDL, see Fig. 18. The build-up of the 497 nm laser is identical.

The narrow-line 689 nm laser is a cateye-reflector ECDL stabilized to a high-finesse ULE cavity residing in a vacuum chamber ($\mathcal{F} = 2 \cdot 10^5$, $FSR = 2$ GHz). A slave laser is injected from the master, whose absolute frequency is determined from its beat signal with a frequency comb, and is adjusted using a double-pass acousto-optic modulator (AOM), (Fig. 19, 20). The frequency comb (Toptica Difference Frequency Comb) is an offset-free comb with repetition rate $f_{\mathrm{rep}} = 80$ MHz. It provides all the wavelengths necessary for running the rubidium Rydberg and the strontium clock experiments: 420, 689, 698, 780, 960, 1016, 1550 nm.

The 2923 nm laser is created using difference-frequency generation (DFG). The light from a 780 nm and a 1064 nm TA are mode-filtered with a single-mode polarization maintaining fiber, combined in free space, and guided into a fiber-coupled PPLN-DFG module, see Fig. 21.

Vacuum system Compactness was of primary concern, therefore the design differs from traditional setups significantly. The section view of the system is shown in Fig. 23. The magnetic field shown in Fig. 17 is generated by two overlapping pairs of anti-Helmholtz coils. The currents are flowing in opposite directions, and with proper design their fields compensate each other in the core region, producing the desired low and homogeneous gradient. The MOT is formed by three pairs of counter propagating lasers. Two dispensers (AlfaVakuo 50 mg) are installed into

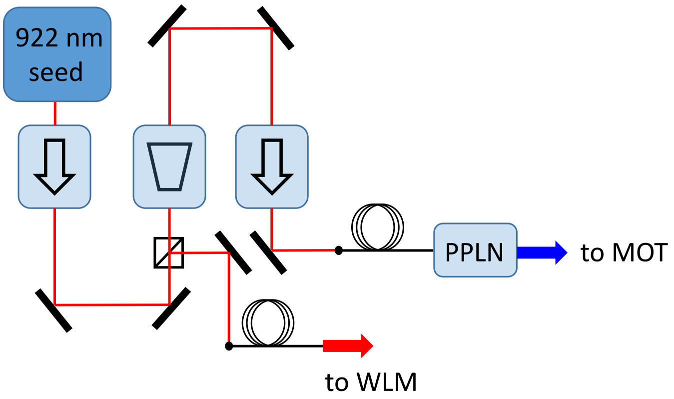

Figure 18: Generation of the 461 nm light: a grating-stabilized ECDL seeds the TA with ∼ 15 mW of light. After passing through various beam-shaping optics (not shown) the light is frequency-doubled by a fiber-coupled ridge-waveguide PPLN. The frequency of the seed laser is stabilized using a commercial wavelength meter.

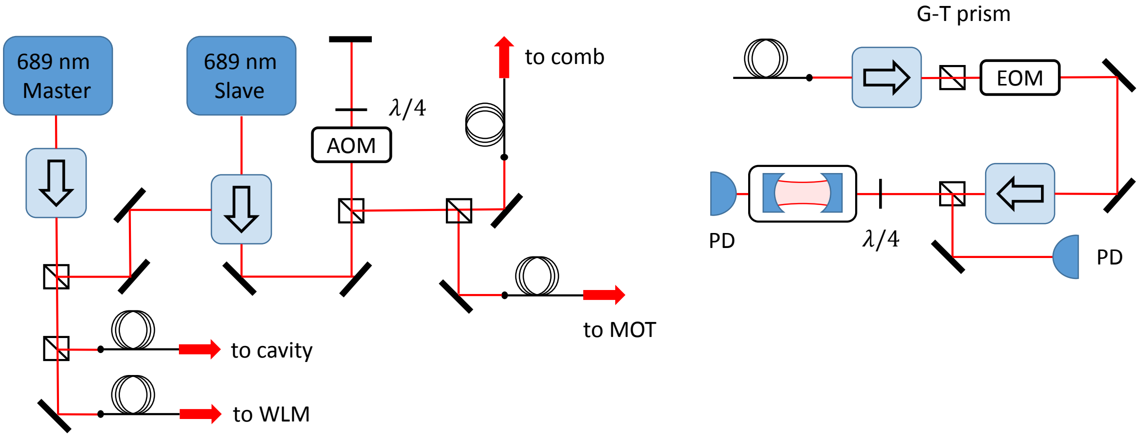

Figure 19: Schematics for the 689 nm laser system. The master laser is stabilized to an ULE cavity, and seeds the slave laser. The absolute frequency is determined by beating the light with the frequency comb, which is used to create a feedback-loop for stabilizing the frequency via a double-pass AOM. (right) The master laser is stabilized to an ULE cavity using Pound-Driver-Hall scheme. Multiple optical isolators are installed to prevent etalon effects. The purity of the polarization is ensured by a Glan–Taylor prism.

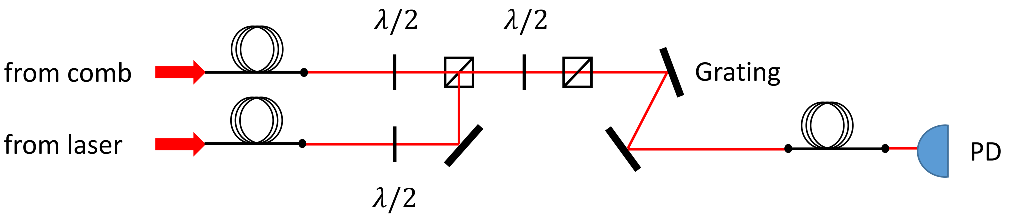

Figure 20: Optical setup for generating the beat signal between the narrow-line MOT laser and the frequency comb.

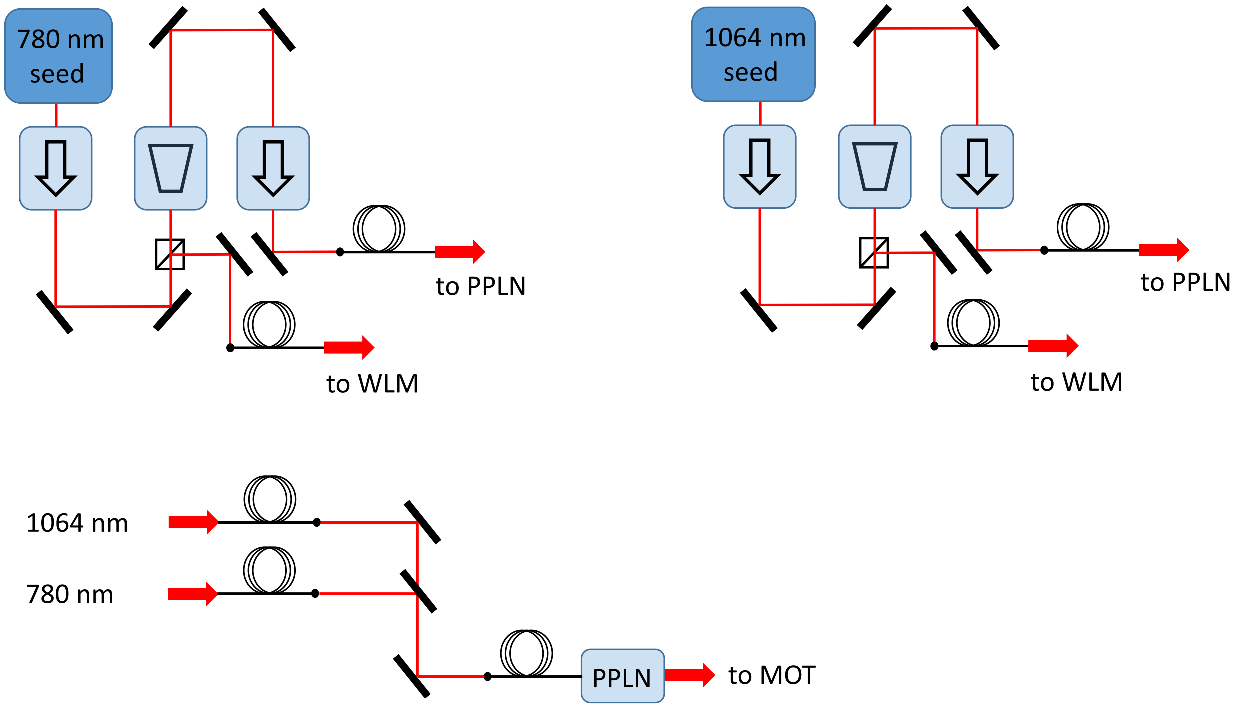

Figure 21: Mid-IR laser system operated at 2923 nm. The target light is created by DFG occuring in fiber-coupled PPLN crystal. The two seed laser systems are identical in principle design with the 922 nm pump laser in Fig. 18

.

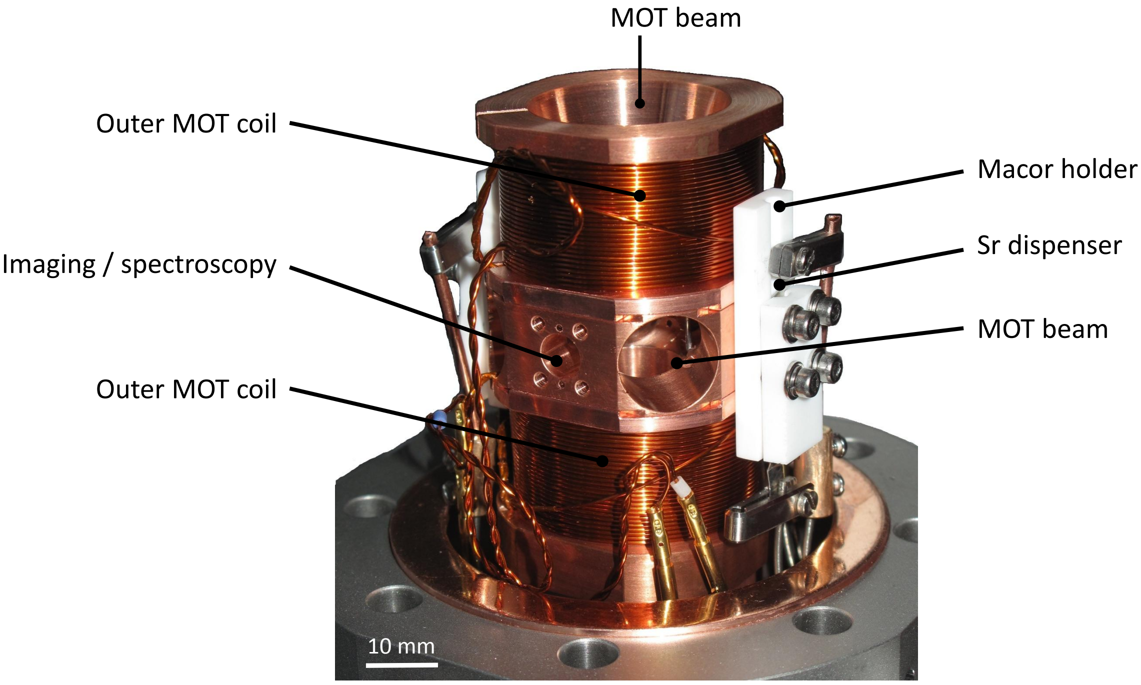

Figure 22: Photo of the mounted copper holder with the dispensers and the MOT coils. The inner coil pair is not visible, it resides below the outer pair. The holder is mounted on a 17 mm diameter copper rod for efficient heat removal.

the chamber. They are clamped between two Macor plates which are screwed to the central copper holder. Direct impact of hot atoms in the MOT region is shielded by two wires with 1 mm diameter. To keep the system as compact as possible, in contrast to other setups, there is no Zeeman slower installed into the chamber. For imaging and absorption spectroscopy there is a separate light path that is not overlapped with the MOT beams, permitting in situ measurements. The assembled system is shown in Fig. 22.

Currently only one dispenser is in use, its first activation curve is shown in Fig. 24. The current is gradually increased from 1.5 A. When the temperature reaches the melting point of the indium seal (190 °C), the seal melts down, releasing the protective argon gas enclosed into the dispenser. This is marked by the sudden increase in pressure at 3.7 A. Appreciable strontium emission is signaled by the second peak, around 4 A. When strontium is emitted, it precipates to the cold surfaces and acts as a getter material, actually lowering the pressure by capturing contaminations. However, the MOT only becomes visible at much higher currents, $I \gtrsim 10$ A, most likely due to the imperfect heat isolation of the dispensers and partial oxidization upon storage.

The coils and the dispensers are generating significant amount of heat that is extracted through a copper rod with diameter of 17 mm. Due to size constraints, the vacuum chamber is assembled from three parts: the upper and lower part host the coils and the dispensers, while the lowest part is used for mounting the electric feedthrough and the vacuum pump (NEXTorr ion getter pump with a passive non-emission getter).

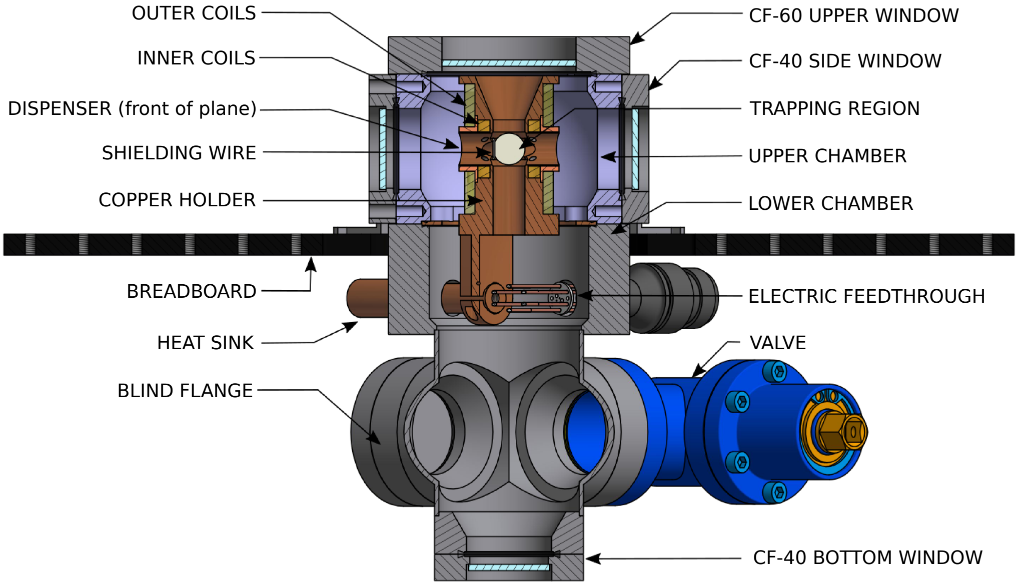

Figure 23: Section view of the vacuum chamber.

Preliminary results We have established a blue MOT using 679 and 707 nm repumpers, and characterized its basic properties. The cooling beam and the two repumper beams were expanded to have a diameter of 15 mm, and were overlapped. The cooling laser was red-detuned by 65 MHz from resonance and had a

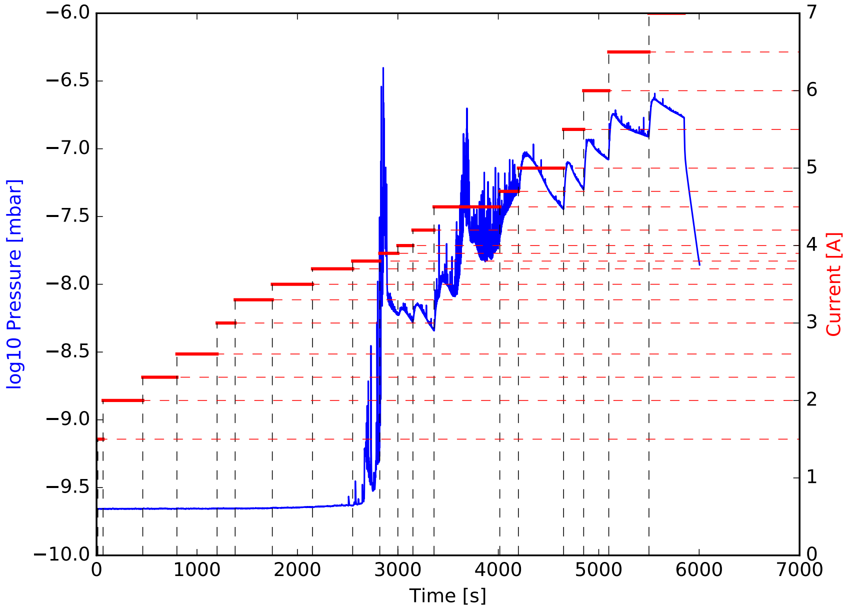

Figure 24: Activation curve of the dispenser in use. Melting of the indium seal occurs around 3.7 A (first emission peak), while evaporation of strontium starts around 4 A (second peak).

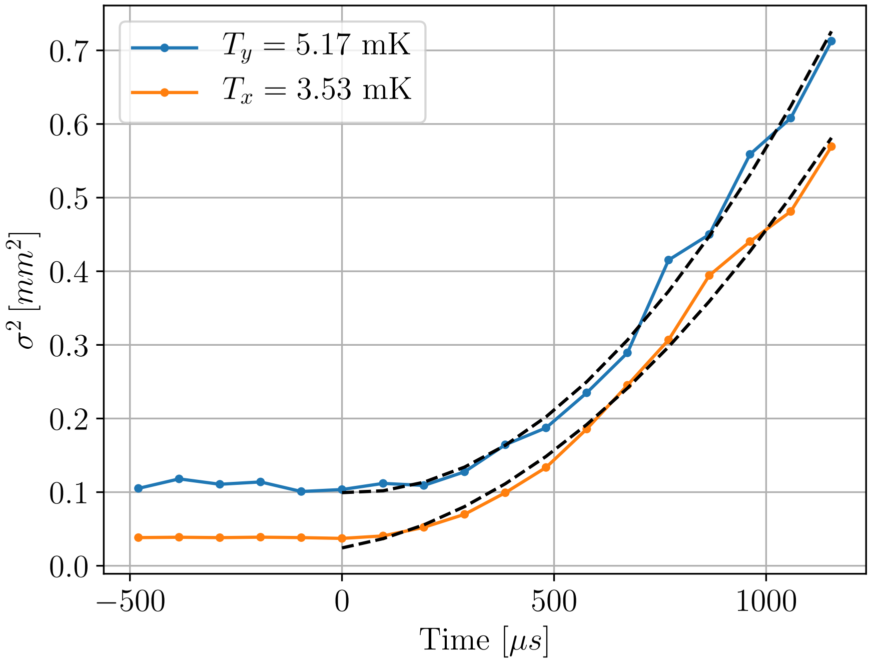

Figure 25: Expansion of the atomic cloud during time-of-flight imaging.

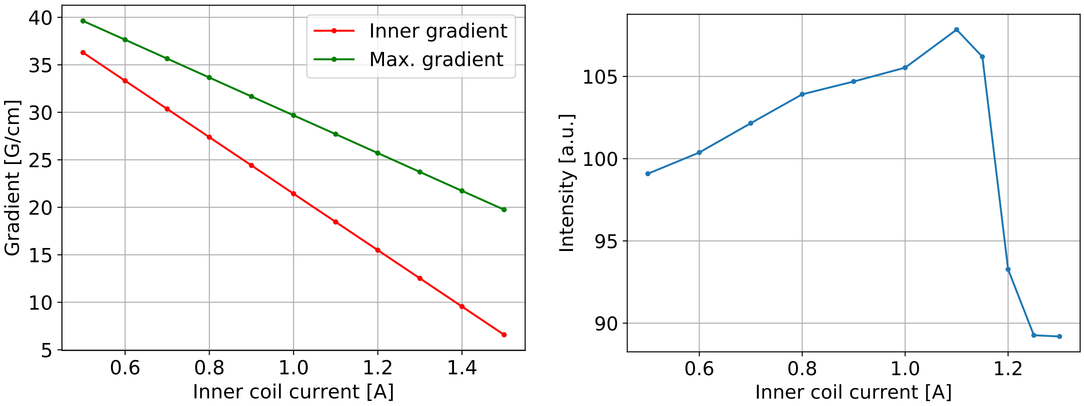

(a) Outer coil current: −1.5 A

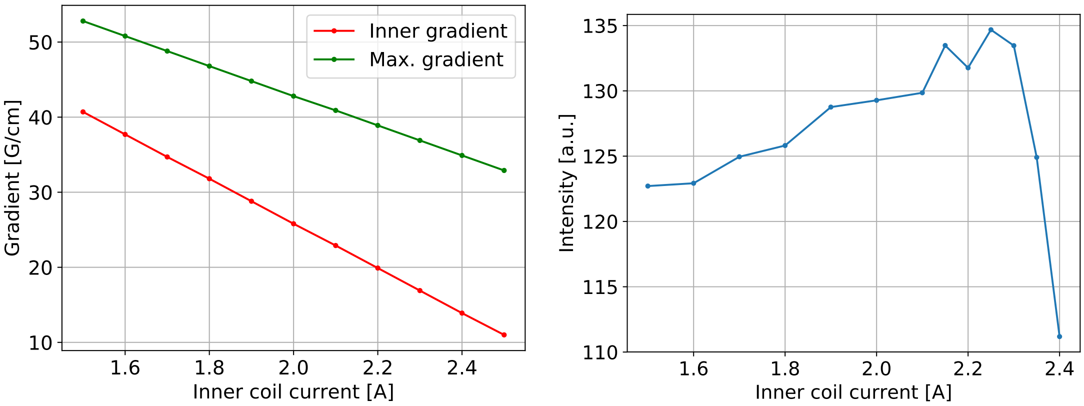

(b) Outer coil current: −2.5 A

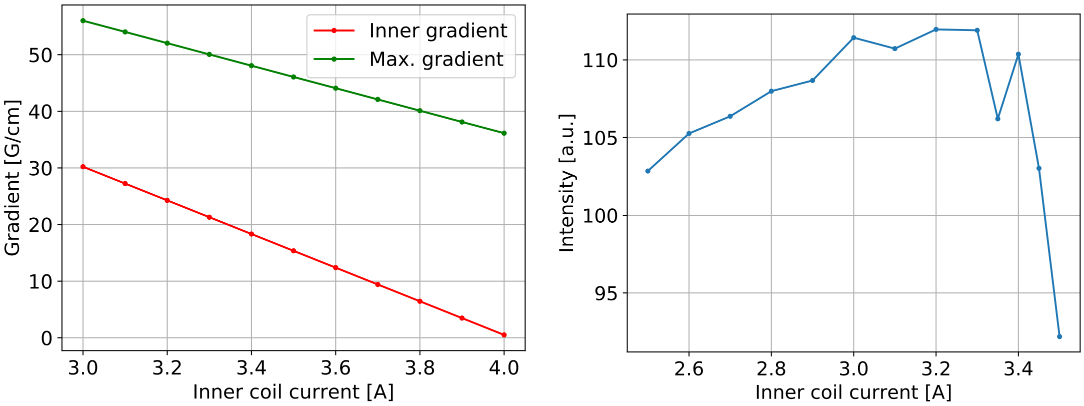

(c) Outer coil current: −3.5 A

Figure 26: Fluorescence of the blue MOT for various core gradients.

power of $P(461\,\mathrm{nm}) = 30$ mW, the repump powers were $P(679\,\mathrm{nm}) = 2.5$ mW and $P(707\,\mathrm{nm}) = 1$ mW. The applied gradient was 50 G/cm. The dispenser was heated with $I = 11$ A, the pressure in the vacuum chamber was $p = 2 \cdot 10^{-9}$ mbar. The density distribution of the cloud was measured by absorption imaging using resonant 461 nm light and a CMOS camera (uEye UI1240SE-NIR). The temperature of the atoms is determined from time-of-flight images following standard procedure [176]. The exact timings of the imaging pulse sequence has been summarized elsewhere [177]. The density profile of the atoms is fitted with a Gaussian with half-width $\sigma(t)$, see Fig. 25. From this the expansion speed can be inferred using $\sigma(t) = \sqrt{\sigma_0^2 + v^2 t^2}$. Finally, the temperature is given by the equipartition theorem $\frac{1}{2}k_B T = \frac{1}{2}mv^2$.

In the core-shell MOT we will need to capture the atoms released from the shell in the core region. We have performed a series of measurements to investigate the behaviour of the blue MOT in the final magnetic field, see Fig. 17. After fixing the current in the outer coils, the inner coil current has been gradually increased and with this the magnetic field gradient has been lowered in the central region. We have detected the fluorescence of the MOT by the same camera as before. The results are summarized in Fig. 26. The gradients in the core region as well as the maximal gradient in the shell region are plotted on the left figures, while the fluorescence of the atoms are shown on the right. To our surprise, the blue MOT is proven to be extremely robust against lowered gradients, and the fluorescence remains detectable at gradients as low as 15 G/cm. This is a very encouraging result for the core-shell concept, since it seems possible to detect the core *and* the shell MOT at the same time.

This research is at a very early stage. The established setup allows us to perform experiments with ultracold strontium atoms. We have presented a novel concept for continuous cooling. Upon lowering the gradients at the core, the confinement potential of the blue MOT gets weaker and weaker, until it is no longer able to contain the atoms. The breakdown point therefore is determined by the confinement strength (which is in turn limited by available laser power in our case) and the temperature of the atoms. Nonetheless, a high concentration of atoms is expected in the core region, which we first indend to collect using a MOT operated on $5s5p\,^3P_2 \rightarrow 5s5d\,^3D_3$ for demonstration purposes.

4 Conclusion and outlook

Hybrid quantum systems consisting of ultracold atoms and superconducting microstructures have been rapidly developed in the recent years. Still, many open questions have to be answered. In this thesis we have reviewed the major challenges and presented our own contributions to combat some of these critical issues.

We have developed an efficient method to control the Zeeman shifts of the hyperfine ground states of alkaline atoms using off-resonant microwave dressing. The differential Zeeman shift between the magnetically trappable clock states of ^{87}Rb has been eliminated up to second order in the magnetic field, reducing the sensitivity to magnetic field inhomogeneities by two orders of magnitude. We believe this method is a powerful way to reduce dephasings in atomic quantum memories originating from magnetic field inhomogeneities and environmental noises.

Mediating long-range interactions between atomic ensembles to perform universal quantum gates between any pairs of qubits is of crucial importance for the scalability of quantum computing. The state-of-the-art technology is to use thermally populated CPW resonators for this purpose, which is insufficient to facilitate currently existing theoretical proposals, because thermal photons reduce the gate fidelities below unusable levels. We have devised two fundamentally different methods to overcome this hurdle. In the first method, we have proposed to actively and continuously remove photons from the cavity, hence reaching a new thermal equilibrium with significantly lowered mode temperature. Using the same cavity mode off-resonantly, a coherent $\sqrt{\text{SWAP}}$ gate is realizable even at high environmental temperatures. The second method relies on a destructive quantum interference between two possible excitation pathways, making our scheme resistant against the photon population of the cavity. This allows us to perform a CPHASE operation with high fidelity. These methods are yet to be demonstrated experimentally, which is the main goal of the newly initiated GiRyd project hosted in our group [178].

The first steps towards these experiments was to learn how to work with ultracold atoms in the vicinity of superconducting surfaces. A most important issue is to establish coherent coupling between the atoms and the CPW resonator. A weak magnetic coupling has indeed been achived using ground-state atoms. The finite lifetime of Rydberg atoms is a limiting factor for Rydberg atom-based quantum gates. The effect of reduced environmental temperature is believed to be helpful, since it lowers the rate of black-body radiation-induced Rydberg-Rydberg transitions. We have investigated this issue in detail. As for the next steps in these experiments, coherent Rydberg-cavity coupling has to be demonstrated, which also demands that we learn to control Rydberg atoms in the vicinity of superconducting surfaces. In particular, efficient methods to reduce the sensitivity of the atoms on external electric fields are necessary. There are also challenges for the solid-state side. By cleverly choosing the materials used in the chip, the deposition of atoms to the surface, and the formation of dipole layers might be suppressed. New layout for flexible electric-field compensation is also required, as well as higher quality factors for the microwave resonators.

In parallel with this work, we have established a highly current and relevant field of research at the University. Indeed, ultracold strontium atoms serve as the backbone of precision metrology. In cooperation with the group of Prof. Hidetoshi Katori (Riken and University of Tokyo), we have worked out a concept for continuously operated optical lattice clocks, which is expected to eliminate the most significant source of instability of the optical lattice clock experiments. We have built a new laboratory, and established a solid MOT setup allowing us to start experimental research along this direction. The next milestone for the core-shell strontium MOT project is to demonstrate the presence of cold atoms in the core region in the final magnetic-field configuration, i.e. with low gradients in the core.

It is worthwhile to put our research into broader perspective. Based on current trends, all-purpose, large-scale digital quantum computers still need at least a decade of intensive development, according to the most conservative estimates [179]. Nonetheless, quantum devices have already started to appear in certain sub-fields of information technology (e.g. secure communication), and are predicted to have a significant impact in many areas in the next five years, e.g. simulation, optimization, quantum internet, and even metrology [179]. Hybrid systems are expected to play an essential role in these applications [23].

As for the lattice clock, we have already discussed that a broad range of applications would benefit from improved clock stability and how continuous operation would enable it by eliminating the single most important limiting factor, the Dick effect. Here, we would like to point out another appealing perspective. Laser stability is a fundamental issue for precison metrology. Currently, all lasers operate in the good-cavity regime, where the laser linewidth is limited by the stability of the optical cavity. With the recent technological advances, we are approaching the limit of possible improvements, the best laser resonators are stable down to subatomic lengths, any further improvement seems extremely difficult [169]. A most probable disruptive technology is the so-called *bad-cavity* laser [180]. Here, the fundamental limitation to the frequency is the atomic transition linewidth and not the cavity, therefore alkaline-earth atoms are primary candidates for this technology due to the narrow clock transition [181]. Transient operation has already been demonstrated on the $5s^2\,{}^1S_0 \rightarrow 5s5p\,{}^3P_1$ [182], but for a real laser, a continuous supply of ultracold strontium atoms is necessary.

5 Acknowledgment

First of all, I would like to thank József Fortágh for being a real mentor to me. He has created an atmosphere that cultivates innovation, taught me so many things, and helped me to grow with his insights and encouragement.

I am grateful for Florian Jessen, from whom I have learned a lot about mechanical and opto-mechanical engineering. His patient and consistent help has been invaluable. Among many other things, he has designed all the vacuum systems related to the strontium experiment, and numerous electronic and opto-mechanical devices.

I would like to thank Helge Hattermann for teaching me the basics of ultracold atomic experiments, and for the many fruitful discussions we had during the years.

I would like to thank David Petrosyan for broadening my theoretical view, and for the enlightening discussions. They have shaped my way of thinking.

I am indebted to the fine mechanical workshop led by Norbert Stockmaier. Their excellent work, friendly help, numerous ideas and recommendations have always made them an integral part of the development we have managed to achieve.

I would like to express my gratitude to Hidetoshi Katori. I have been lucky for having the opportunity to learn from him, discuss new ideas and work in his laboratory in Riken, Japan. He has supported us in establishing the ultracold strontium experiment in Tübingen with know-how, hardware, and manpower. I am thankful for Shouichi Okaba for helping us setting up the first lasers, for Noriaki Ohmae for teaching me about optical engineering, and assembling the first cavity stabilization in the experiment, and for Tomoya Akatsuka for his assistance during my stay at Riken.

References

[PUB 1] L. Sárkány, P. Weiss, H. Hattermann, and J. Fortágh, “Controlling the magnetic-field sensitivity of atomic-clock states by microwave dressing”, Phys. Rev. A **90**, 053416 (2014).

[PUB 2] L. Sárkány, J. Fortágh, and D. Petrosyan, “Long-range quantum gate via Rydberg states of atoms in a thermal microwave cavity”, Phys. Rev. A **92**, 030303 (2015).

[PUB 3] L. Sárkány, J. Fortágh, and D. Petrosyan, “Faithful state transfer between two-level systems via an actively cooled finite-temperature cavity”, Phys. Rev. A **97**, 032341 (2018).

[PUB 4] P. Weiss, M. Knufinke, S. Bernon, D. Bothner, L. Sárkány, C. Zimmermann, R. Kleiner, D. Koelle, J. Fortágh, and H. Hattermann, “Sensitivity of ultracold atoms to quantized flux in a superconducting ring”, Phys. Rev. Lett. **114**, 113003 (2015).

[PUB 5] M. Mack, J. Grimmel, F. Karlewski, L. Sárkány, H. Hattermann, and J. Fortágh, “All-optical measurement of Rydberg-state lifetimes”, Phys. Rev. A **92**, 012517 (2015).

[PUB 6] H. Hattermann, D. Bothner, L. Y. Ley, B. Ferdinand, D. Wiedmaier, L. Sárkány, R. Kleiner, D. Koelle, and J. Fortágh, “Coupling ultracold atoms to a superconducting coplanar waveguide resonator”, Nature Communications **8**, 2254 (2017).

[1] R. P. Feynman, “Simulating physics with computers”, International Journal of Theoretical Physics **21**, 467 (1982).

[2] D. Deutsch, “Quantum theory, the Church-Turing principle and the universal quantum computer”, Proceedings of the Royal Society of London A: Mathematical, Physical and Engineering Sciences **400**, 97 (1985).

[3] S. Wiesner, “Conjugate coding”, SIGACT News **15**, 78 (1983).

[4] C. H. Bennett and G. Brassard, “Quantum cryptography: public key distribution and coin tossing”, Proceedings of IEEE International Conference on Computers, Systems and Signal Processing **175**, 8 (1984).

[5] A. Montanaro, “Quantum algorithms: an overview”, Npj Quantum Information **2**, Review Article, 15023 (2016).

[6] D. Deutsch and R. Jozsa, “Rapid solution of problems by quantum computation”, Proceedings of the Royal Society of London A: Mathematical, Physical and Engineering Sciences **439**, 553 (1992).

[7] P. W. Shor, “Polynomial-time algorithms for prime factorization and discrete logarithms on a quantum computer”, SIAM Journal on Computing **26**, 1484 (1997).

[8] A. W. Harrow, A. Hassidim, and S. Lloyd, “Quantum algorithm for linear systems of equations”, Phys. Rev. Lett. **103**, 150502 (2009).

[9] L. K. Grover, "A fast quantum mechanical algorithm for database search", in Proceedings of the 28th Annual ACM Symposium on Theory of Computing (1996), pp. 212–219.

[10] J. Simon, W. S. Bakr, R. Ma, M. E. Tai, P. M. Preiss, and M. Greiner, "Quantum simulation of antiferromagnetic spin chains in an optical lattice", Nature **472**, 307 (2011).

[11] K. Kim, M.-S. Chang, S. Korenblit, R. Islam, E. E. Edwards, J. K. Freericks, G.-D. Lin, L.-M. Duan, and C. Monroe, "Quantum simulation of frustrated Ising spins with trapped ions", Nature **465**, 590 (2010).

[12] J. Zhang, G. Pagano, P. W. Hess, A. Kyprianidis, P. Becker, H. Kaplan, A. V. Gorshkov, Z.-X. Gong, and C. Monroe, "Observation of a many-body dynamical phase transition with a 53-qubit quantum simulator", Nature **551** (2017).

[13] *D-wave systems inc.* `https://www.dwavesys.com/`.

[14] H. J. Briegel, D. E. Browne, W. Dur, R. Raussendorf, and M. Van den Nest, "Measurement-based quantum computation", Nat. Phys., 19 (2009).

[15] M. H. Freedman, A. Kitaev, M. J. Larsen, and Z. Wang, "Topological quantum computation", Bull. Amer. Math. Soc. **40**, 31 (2003).

[16] M. A. Nielsen and I. L. Chuang, *Quantum computation and quantum information, 10th anniversary edition* (Cambridge University Press, 2010).

[17] E. Rieffel and W. Polak, *Quantum computing: a gentle introduction*, 1st edition (The MIT Press, 2011).

[18] D. P. DiVincenzo, "The physical implementation of quantum computation", Fortschritte der Physik **48**, 771 (2000).

[19] W. H. Wootters W. K.and Zurek, "A single quantum cannot be cloned", Nature **299**, 802 (1982).

[20] B. M. Terhal, "Quantum error correction for quantum memories", Rev. Mod. Phys. **87**, 307 (2015).

[21] S. J. Devitt, W. J. Munro, and K. Nemoto, "Quantum error correction for beginners", Reports on Progress in Physics **76**, 076001 (2013).

[22] T. Monz, P. Schindler, J. T. Barreiro, M. Chwalla, D. Nigg, W. A. Coish, M. Harlander, W. Hänsel, M. Hennrich, and R. Blatt, "14-qubit entanglement: creation and coherence", Phys. Rev. Lett. **106**, 130506 (2011).

[23] G. Kurizki, P. Bertet, Y. Kubo, K. Mølmer, D. Petrosyan, P. Rabl, and J. Schmiedmayer, "Quantum technologies with hybrid systems", Proceedings of the National Academy of Sciences **112**, 3866 (2015).

[24] Z.-L. Xiang, S. Ashhab, J. Q. You, and F. Nori, "Hybrid quantum circuits: superconducting circuits interacting with other quantum systems", Rev. Mod. Phys. **85**, 623 (2013).

[25] M. Tavis and F. W. Cummings, "Exact solution for an N-molecule radiation-field Hamiltonian", Phys. Rev. **170**, 379 (1968).

[26] A. Aspuru-Guzik and P. Walther, “Photonic quantum simulators”, Nat. Phys. **8**, 285 (2012).

[27] I. Bloch, J. Dalibard, and S. Nascimbene, “Quantum simulations with ultracold quantum gases”, Nat. Phys. **8**, 267 (2012).

[28] R. Blatt and C. F. Roos, “Quantum simulations with trapped ions”, Nat. Phys. **8**, 277 (2012).

[29] J. I. Cirac and P. Zoller, “Quantum computations with cold trapped ions”, Phys. Rev. Lett. **74**, 4091 (1995).

[30] A. Andre, D. DeMille, J. M. Doyle, M. D. Lukin, S. E. Maxwell, P. Rabl, R. J. Schoelkopf, and P. Zoller, “A coherent all-electrical interface between polar molecules and mesoscopic superconducting resonators”, Nat. Phys. **2**, 636 (2006).

[31] P. Rabl, D. DeMille, J. M. Doyle, M. D. Lukin, R. J. Schoelkopf, and P. Zoller, “Hybrid quantum processors: molecular ensembles as quantum memory for solid state circuits”, Phys. Rev. Lett. **97**, 033003 (2006).

[32] J. Wrachtrup and F. Jelezko, “Processing quantum information in diamond”, Journal of Physics: Condensed Matter **18**, S807 (2006).

[33] P. C. Maurer, G. Kucsko, C. Latta, L. Jiang, N. Y. Yao, S. D. Bennett, F. Pastawski, D. Hunger, N. Chisholm, M. Markham, D. J. Twitchen, J. I. Cirac, and M. D. Lukin, “Room-temperature quantum bit memory exceeding one second”, Science **336**, 1283 (2012).

[34] J. J. Pla, K. Y. Tan, J. P. Dehollain, W. H. Lim, J. J. L. Morton, F. A. Zwanenburg, D. N. Jamieson, A. S. Dzurak, and A. Morello, “High-fidelity readout and control of a nuclear spin qubit in silicon”, Nature **496**, Letter, 334 (2013).

[35] R. J. Schoelkopf and S. M. Girvin, “Wiring up quantum systems”, Nature **451**, 664 (2008).

[36] A. A. Houck, H. E. Tureci, and J. Koch, “On-chip quantum simulation with superconducting circuits”, Nat. Phys. **8**, 292 (2012).

[37] M. H. Devoret and R. J. Schoelkopf, “Superconducting circuits for quantum information: an outlook”, Science **339**, 1169 (2013).

[38] M. Aspelmeyer, T. J. Kippenberg, and F. Marquardt, “Cavity optomechanics”, Rev. Mod. Phys. **86**, 1391 (2014).

[39] T. Niemczyk, F. Deppe, H. Huebl, E. P. Menzel, F. Hocke, M. J. Schwarz, J. J. Garcia-Ripoll, D. Zueco, T. Hummer, E. Solano, A. Marx, and R. Gross, “Circuit quantum electrodynamics in the ultrastrong-coupling regime”, Nat. Phys. **6**, 772 (2010).

[40] A. Imamoğlu, “Cavity QED based on collective magnetic dipole coupling: spin ensembles as hybrid two-level systems”, Phys. Rev. Lett. **102**, 083602 (2009).

[41] J. H. Wesenberg, A. Ardavan, G. A. D. Briggs, J. J. L. Morton, R. J. Schoelkopf, D. I. Schuster, and K. Mølmer, “Quantum computing with an electron spin ensemble”, Phys. Rev. Lett. **103**, 070502 (2009).

[42] Y. Kubo, C. Grezes, A. Dewes, T. Umeda, J. Isoya, H. Sumiya, N. Morishita, H. Abe, S. Onoda, T. Ohshima, V. Jacques, A. Dréau, J.-F. Roch, I. Diniz, A. Auffeves, D. Vion, D. Esteve, and P. Bertet, “Hybrid quantum circuit with a superconducting qubit coupled to a spin ensemble”, Phys. Rev. Lett. **107**, 220501 (2011).

[43] S. Saito, X. Zhu, R. Amsüss, Y. Matsuzaki, K. Kakuyanagi, T. Shimo-Oka, N. Mizuochi, K. Nemoto, W. J. Munro, and K. Semba, “Towards realizing a quantum memory for a superconducting qubit: storage and retrieval of quantum states”, Phys. Rev. Lett. **111**, 107008 (2013).

[44] X. Zhu, S. Saito, A. Kemp, K. Kakuyanagi, S.-i. Karimoto, H. Nakano, W. J. Munro, Y. Tokura, M. S. Everitt, K. Nemoto, M. Kasu, N. Mizuochi, and K. Semba, “Coherent coupling of a superconducting flux qubit to an electron spin ensemble in diamond”, Nature **478**, 221 (2011).

[45] S. Probst, H. Rotzinger, S. Wünsch, P. Jung, M. Jerger, M. Siegel, A. V. Ustinov, and P. A. Bushev, “Anisotropic rare-earth spin ensemble strongly coupled to a superconducting resonator”, Phys. Rev. Lett. **110**, 157001 (2013).

[46] D. I. Schuster, A. P. Sears, E. Ginossar, L. DiCarlo, L. Frunzio, J. J. L. Morton, H. Wu, G. A. D. Briggs, B. B. Buckley, D. D. Awschalom, and R. J. Schoelkopf, “High-cooperativity coupling of electron-spin ensembles to superconducting cavities”, Phys. Rev. Lett. **105**, 140501 (2010).

[47] P. Bushev, A. K. Feofanov, H. Rotzinger, I. Protopopov, J. H. Cole, C. M. Wilson, G. Fischer, A. Lukashenko, and A. V. Ustinov, “Ultralow-power spectroscopy of a rare-earth spin ensemble using a superconducting resonator”, Phys. Rev. B **84**, 060501 (2011).

[48] S. Bernon, H. Hattermann, D. Bothner, M. Knufinke, P. Weiss, F. Jessen, D. Cano, M. Kemmler, R. Kleiner, D. Koelle, and J. Fortágh, “Manipulation and coherence of ultra-cold atoms on a superconducting atom chip”, Nature Communications **4** (2013).

[49] A. G. Radnaev, Y. O. Dudin, R. Zhao, H. H. Jen, S. D. Jenkins, A. Kuzmich, and T. A. B. Kennedy, “A quantum memory with telecom-wavelength conversion”, Nat. Phys. **6**, 894 (2010).

[50] Y. O. Dudin, R. Zhao, T. A. B. Kennedy, and A. Kuzmich, “Light storage in a magnetically dressed optical lattice”, Phys. Rev. A **81**, 041805 (2010).

[51] H. P. Specht, C. Nolleke, A. Reiserer, M. Uphoff, E. Figueroa, S. Ritter, and G. Rempe, “A single-atom quantum memory”, Nature **473**, 190 (2011).

[52] S. Ritter, C. Nolleke, C. Hahn, A. Reiserer, A. Neuzner, M. Uphoff, M. Mucke, E. Figueroa, J. Bochmann, and G. Rempe, “An elementary quantum network of single atoms in optical cavities”, Nature **484**, 195 (2012).

[53] M. Hafezi, Z. Kim, S. L. Rolston, L. A. Orozco, B. L. Lev, and J. M. Taylor, "Atomic interface between microwave and optical photons", Phys. Rev. A **85**, 020302 (2012).

[54] B. T. Gard, K. Jacobs, R. McDermott, and M. Saffman, "Microwave-to-optical frequency conversion using a caesium atom coupled to a superconducting resonator", Phys. Rev. A **96**, 013833 (2017).

[55] M. D. Lukin, M. Fleischhauer, R. Cote, L. M. Duan, D. Jaksch, J. I. Cirac, and P. Zoller, "Dipole blockade and quantum information processing in mesoscopic atomic ensembles", Phys. Rev. Lett. **87**, 037901 (2001).

[56] M. Saffman, T. G. Walker, and K. Mølmer, "Quantum information with Rydberg atoms", Rev. Mod. Phys. **82**, 2313 (2010).

[57] D. Petrosyan, F. Motzoi, M. Saffman, and K. Mølmer, "High-fidelity Rydberg quantum gate via a two-atom dark state", Phys. Rev. A **96**, 042306 (2017).

[58] L. Isenhower, E. Urban, X. L. Zhang, A. T. Gill, T. Henage, T. A. Johnson, T. G. Walker, and M. Saffman, "Demonstration of a Neutral Atom Controlled-NOT Quantum Gate", Phys. Rev. Lett. **104**, 010503 (2010).

[59] T. Wilk, A. Gaëtan, C. Evellin, J. Wolters, Y. Miroshnychenko, P. Grangier, and A. Browaeys, "Entanglement of Two Individual Neutral Atoms Using Rydberg Blockade", Phys. Rev. Lett. **104**, 010502 (2010).

[60] G. Breit and I. I. Rabi, "Measurement of nuclear spin", Phys. Rev. **38**, 2082 (1931).

[61] P. Rosenbusch, "Magnetically trapped atoms for compact atomic clocks", Applied Physics B **95**, 227 (2009).

[62] D. M. Harber, H. J. Lewandowski, J. M. McGuirk, and E. A. Cornell, "Effect of cold collisions on spin coherence and resonance shifts in a magnetically trapped ultracold gas", Phys. Rev. A **66**, 053616 (2002).

[63] P. Treutlein, P. Hommelhoff, T. Steinmetz, T. W. Hänsch, and J. Reichel, "Coherence in microchip traps", Phys. Rev. Lett. **92**, 203005 (2004).

[64] V. Vuletić and J. Reichel, eds., *Atom chips* (Wiley-VCH Verlag GmbH & Co. KGaA, 2011).

[65] M. Mack, F. Karlewski, H. Hattermann, S. Höckh, F. Jessen, D. Cano, and J. Fortágh, "Measurement of absolute transition frequencies of ^{87}Rb to nS and nD Rydberg states by means of electromagnetically induced transparency", Phys. Rev. A **83**, 052515 (2011).

[66] A. Sanayei, N. Schopohl, J. Grimmel, M. Mack, F. Karlewski, and J. Fortágh, "Quasiclassical quantum defect theory and the spectrum of highly excited rubidium atoms", Phys. Rev. A **91**, 032509 (2015).

[67] B. W. Shore, K. Bergmann, A. Kuhn, S. Schiemann, J. Oreg, and J. H. Eberly, "Laser-induced population transfer in multistate systems: a comparative study", Phys. Rev. A **45**, 5297 (1992).

[68] J. Lim, H.-g. Lee, and J. Ahn, “Review of cold Rydberg atoms and their applications”, Journal of the Korean Physical Society **63**, 867 (2013).

[69] M. Gross and S. Haroche, “Superradiance: an essay on the theory of collective spontaneous emission”, Physics Reports **93**, 301 (1982).

[70] A. Gaetan, Y. Miroshnychenko, T. Wilk, A. Chotia, M. Viteau, D. Comparat, P. Pillet, A. Browaeys, and P. Grangier, “Observation of collective excitation of two individual atoms in the Rydberg blockade regime”, Nat. Phys. **5**, 115 (2009).

[71] J. Zeiher, P. Schauß, S. Hild, T. Macri, I. Bloch, and C. Gross, “Microscopic Characterization of Scalable Coherent Rydberg Superatoms”, Phys. Rev. X **5**, 031015 (2015).

[72] M. Ebert, M. Kwon, T. G. Walker, and M. Saffman, “Coherence and Rydberg Blockade of Atomic Ensemble Qubits”, Phys. Rev. Lett. **115**, 093601 (2015).

[73] Y. O. Dudin, L. Li, F. Bariani, and A. Kuzmich, “Observation of coherent many-body Rabi oscillations”, Nature Physics **8** (2012).

[74] D. Petrosyan, M. Höning, and M. Fleischhauer, “Spatial correlations of Rydberg excitations in optically driven atomic ensembles”, Phys. Rev. A **87**, 053414 (2013).

[75] T. G. Walker and M. Saffman, “Consequences of Zeeman degeneracy for the van der Waals blockade between Rydberg atoms”, Phys. Rev. A **77**, 032723 (2008).

[76] A. A. Kamenski, N. L. Manakov, S. N. Mokhnenko, and V. D. Ovsiannikov, “Energy of van der Waals and dipole-dipole interactions between atoms in Rydberg states”, Phys. Rev. A **96**, 032716 (2017).

[77] A. Reinhard, T. C. Liebisch, B. Knuffman, and G. Raithel, “Level shifts of rubidium Rydberg states due to binary interactions”, Phys. Rev. A **75**, 032712 (2007).

[78] A. Walz-Flannigan, J. R. Guest, J.-H. Choi, and G. Raithel, “Cold-Rydberg-gas dynamics”, Phys. Rev. A **69**, 063405 (2004).

[79] P. Nussenzveig, F. Bernardot, M. Brune, J. Hare, J. M. Raimond, S. Haroche, and W. Gawlik, “Preparation of high-principal-quantum-number “circular” states of rubidium”, Phys. Rev. A **48**, 3991 (1993).

[80] C. Deutsch, F. Ramirez-Martinez, C. Lacroûte, F. Reinhard, T. Schneider, J. N. Fuchs, F. Piéchon, F. Laloë, J. Reichel, and P. Rosenbusch, “Spin self-rephasing and very long coherence times in a trapped atomic ensemble”, Phys. Rev. Lett. **105**, 020401 (2010).

[81] D. Cano, H. Hattermann, B. Kasch, C. Zimmermann, R. Kleiner, D. Koelle, and J. Fortágh, “Experimental system for research on ultracold atomic gases near superconducting microstructures”, The European Physical Journal D **63**, 17 (2011).

[82] M. Aspelmeyer, T. J. Kippenberg, and F. Marquardt, "Cavity optomechanics", Rev. Mod. Phys. **86**, 1391 (2014).

[83] M. Poot and H. S. van der Zant, "Mechanical systems in the quantum regime", Physics Reports **511**, 273 (2012).

[84] S. Kuhr, S. Gleyzes, C. Guerlin, J. Bernu, U. B. Hoff, S. Deléglise, S. Osnaghi, M. Brune, J.-M. Raimond, S. Haroche, E. Jacques, P. Bosland, and B. Visentin, "Ultrahigh finesse Fabry-Pérot superconducting resonator", Applied Physics Letters **90**, 164101 (2007).

[85] J. M. Raimond, P. Goy, M. Gross, C. Fabre, and S. Haroche, "Statistics of millimeter-wave photons emitted by a Rydberg-atom maser: an experimental study of fluctuations in single-mode superradiance", Phys. Rev. Lett. **49**, 1924 (1982).

[86] M. Gross, P. Goy, C. Fabre, S. Haroche, and J. M. Raimond, "Maser oscillation and microwave superradiance in small systems of Rydberg atoms", Phys. Rev. Lett. **43**, 343 (1979).

[87] M. Brune, F. Schmidt-Kaler, A. Maali, J. Dreyer, E. Hagley, J. M. Raimond, and S. Haroche, "Quantum Rabi oscillation: a direct test of field quantization in a cavity", Phys. Rev. Lett. **76**, 1800 (1996).

[88] G. Rempe, H. Walther, and N. Klein, "Observation of quantum collapse and revival in a one-atom maser", Phys. Rev. Lett. **58**, 353 (1987).

[89] H. Ott, J. Fortagh, G. Schlotterbeck, A. Grossmann, and C. Zimmermann, "Bose-Einstein condensation in a surface microtrap", Phys. Rev. Lett. **87**, 230401 (2001).

[90] W. Hänsel, P. Hommelhoff, T. W. Hänsch, and J. Reichel, "Bose-Einstein condensation on a microelectronic chip", Nature **413**, 498 (2001).

[91] B. Kasch, H. Hattermann, D. Cano, T. E. Judd, S. Scheel, C. Zimmermann, R. Kleiner, D. Koelle, and J. Fortágh, "Cold atoms near superconductors: atomic spin coherence beyond the Johnson noise limit", New Journal of Physics **12**, 065024 (2010).

[92] D. Bothner, M. Knufinke, H. Hattermann, R. Wölbing, B. Ferdinand, P. Weiss, S. Bernon, J. Fortágh, D. Koelle, and R. Kleiner, "Inductively coupled superconducting half wavelength resonators as persistent current traps for ultracold atoms", New Journal of Physics **15**, 093024 (2013).

[93] H. Hattermann, "Interfacing cold atoms and superconductors", PhD thesis (Eberhard Karls Universität Tübingen, 2013).

[94] J. Halbritter, "Surface residual resistance of high-Q-superconducting resonators", Journal of Applied Physics **42**, 82 (1971).

[95] R. Doll and M. Näbauer, "Experimental proof of magnetic flux quantization in a superconducting ring", Phys. Rev. Lett. **7**, 51 (1961).

[96] B. S. Deaver and W. M. Fairbank, "Experimental evidence for quantized flux in superconducting cylinders", Phys. Rev. Lett. **7**, 43 (1961).

[97] D. Cano, B. Kasch, H. Hattermann, D. Koelle, R. Kleiner, C. Zimmermann, and J. Fortágh, “Impact of the Meissner effect on magnetic microtraps for neutral atoms near superconducting thin films”, Phys. Rev. A **77**, 063408 (2008).

[98] J. Fortágh and C. Zimmermann, “Magnetic microtraps for ultracold atoms”, Rev. Mod. Phys. **79**, 235 (2007).

[99] J. Denschlag, D. Cassettari, and J. Schmiedmayer, “Guiding neutral atoms with a wire”, Phys. Rev. Lett. **82**, 2014 (1999).

[100] A. Günther, M. Kemmler, S. Kraft, C. J. Vale, C. Zimmermann, and J. Fortágh, “Combined chips for atom optics”, Phys. Rev. A **71**, 063619 (2005).

[101] J. A. Stickney and A. A. Zozulya, “Influence of nonadiabaticity and nonlinearity on the operation of cold-atom beam splitters”, Phys. Rev. A **68**, 013611 (2003).

[102] W. Hänsel, J. Reichel, P. Hommelhoff, and T. W. Hänsch, “Magnetic conveyor belt for transporting and merging trapped atom clouds”, Phys. Rev. Lett. **86**, 608 (2001).

[103] W. Hansel, P. Hommelhoff, T. W. Hansch, and J. Reichel, “Bose-Einstein condensation on a microelectronic chip”, Nature **413**, 498 (2001).

[104] J. Reichel, W. Hänsel, and T. W. Hänsch, “Atomic micromanipulation with magnetic surface traps”, Phys. Rev. Lett. **83**, 3398 (1999).

[105] J. Verdú, H. Zoubi, C. Koller, J. Majer, H. Ritsch, and J. Schmiedmayer, “Strong magnetic coupling of an ultracold gas to a superconducting waveguide cavity”, Phys. Rev. Lett. **103**, 043603 (2009).

[106] J. Grimmel, M. Mack, F. Karlewski, F. Jessen, M. Reinschmidt, N. Sándor, and J. Fortágh, “Measurement and numerical calculation of rubidium Rydberg Stark spectra”, New Journal of Physics **17**, 053005 (2015).

[107] H. Hattermann, M. Mack, F. Karlewski, F. Jessen, D. Cano, and J. Fortágh, “Detrimental adsorbate fields in experiments with cold Rydberg gases near surfaces”, Phys. Rev. A **86**, 022511 (2012).

[108] K. S. Chan, M. Siercke, C. Hufnagel, and R. Dumke, “Adsorbate electric fields on a cryogenic atom chip”, Phys. Rev. Lett. **112**, 026101 (2014).

[109] J. M. Obrecht, R. J. Wild, and E. A. Cornell, “Measuring electric fields from surface contaminants with neutral atoms”, Phys. Rev. A **75**, 062903 (2007).

[110] J. M. McGuirk, D. M. Harber, J. M. Obrecht, and E. A. Cornell, “Alkali-metal adsorbate polarization on conducting and insulating surfaces probed with Bose-Einstein condensates”, Phys. Rev. A **69**, 062905 (2004).

[111] K. D. Sattler, *Handbook of nanophysics: clusters and fullerenes* (CRC Press, Taylor & Francis Group, 2011).

[112] C. Hermann-Avigliano, R. C. Teixeira, T. L. Nguyen, T. Cantat-Moltrecht, G. Nogues, I. Dotsenko, S. Gleyzes, J. M. Raimond, S. Haroche, and M. Brune, "Long coherence times for Rydberg qubits on a superconducting atom chip", Phys. Rev. A **90**, 040502 (2014).

[113] L. A. Jones, J. D. Carter, and J. D. D. Martin, "Rydberg atoms with a reduced sensitivity to dc and low-frequency electric fields", Phys. Rev. A **87**, 023423 (2013).

[114] I. I. Beterov, I. I. Ryabtsev, D. B. Tretyakov, and V. M. Entin, "Quasiclassical calculations of blackbody-radiation-induced depopulation rates and effective lifetimes of Rydberg nS, nP, and nD alkali-metal atoms with $n \leq 80$", Phys. Rev. A **79**, 052504 (2009).

[115] D. Petrosyan, G. Bensky, G. Kurizki, I. Mazets, J. Majer, and J. Schmiedmayer, "Reversible state transfer between superconducting qubits and atomic ensembles", Phys. Rev. A **79**, 040304 (2009).

[116] J. D. Pritchard, J. A. Isaacs, M. A. Beck, R. McDermott, and M. Saffman, "Hybrid atom-photon quantum gate in a superconducting microwave resonator", Phys. Rev. A **89**, 010301 (2014).

[117] P. Rabl, D. DeMille, J. M. Doyle, M. D. Lukin, R. J. Schoelkopf, and P. Zoller, "Hybrid quantum processors: molecular ensembles as quantum memory for solid state circuits", Phys. Rev. Lett. **97**, 033003 (2006).

[118] K. Tordrup and K. Mølmer, "Quantum computing with a single molecular ensemble and a Cooper-pair box", Phys. Rev. A **77**, 020301 (2008).

[119] F. Jessen, M. Knufinke, S. C. Bell, P. Vergien, H. Hattermann, P. Weiss, M. Rudolph, M. Reinschmidt, K. Meyer, T. Gaber, D. Cano, A. Günther, S. Bernon, D. Koelle, R. Kleiner, and J. Fortágh, "Trapping of ultracold atoms in a ^{3}He/^{4}He dilution refrigerator", Applied Physics B **116**, 665 (2014).

[120] G. Nogues, A. Rauschenbeutel, S. Osnaghi, M. Brune, J. M. Raimond, and S. Haroche, "Seeing a single photon without destroying it", Nature **400**, 239 (1999).

[121] A. Sørensen and K. Mølmer, "Quantum computation with ions in thermal motion", Phys. Rev. Lett. **82**, 1971 (1999).

[122] K. Mølmer and A. Sørensen, "Multiparticle entanglement of hot trapped ions", Phys. Rev. Lett. **82**, 1835 (1999).

[123] P. Lambropoulos and D. Petrosyan, *Fundamentals of quantum optics and quantum information* (Springer, Berlin, 2007).

[124] A. Sørensen and K. Mølmer, "Entanglement and quantum computation with ions in thermal motion", Phys. Rev. A **62**, 022311 (2000).

[125] F. Riehle, *Frequency standards, Basics and applications* (Wiley-VCH, Weinheim, 2004).

[126] D. Kleppner, H. M. Goldenberg, and N. F. Ramsey, "Theory of the hydrogen maser", Phys. Rev. **126**, 603 (1962).

[127] J. F. DeNatale, R. L. Borwick, C. Tsai, P. A. Stupar, Y. Lin, R. A. Newgard, R. W. Berquist, and M. Zhu, "Compact, low-power chip-scale atomic clock", in 2008 IEEE/ION Position, Location and Navigation Symposium (May 2008), pp. 67–70.

[128] M. J. Mescher, R. Lutwak, and M. Varghese, "An ultra-low-power physics package for a chip-scale atomic clock", in The 13th international conference on solid-state sensors, actuators and microsystems, 2005. digest of technical papers. Vol. 1 (June 2005), pp. 311–316.

[129] F. G. Major, *Quo vadis: evolution of modern navigation: the rise of quantum techniques*, 1st ed. (Springer-Verlag New York, 2014).

[130] S. Bregni, "Synchronization of digital telecommunications networks", in (John Wiley & Sons, Ltd, 2002).

[131] BIPM, *The International System of Units (SI)*, 8th ed. (BIPM, 2006).

[132] H. G. Dehmelt, Bull. Am. Phys. Soc. **18**, 1521 (1973).

[133] T. Rosenband, D. B. Hume, P. O. Schmidt, C. W. Chou, A. Brusch, L. Lorini, W. H. Oskay, R. E. Drullinger, T. M. Fortier, J. E. Stalnaker, S. A. Diddams, W. C. Swann, N. R. Newbury, W. M. Itano, D. J. Wineland, and J. C. Bergquist, "Frequency ratio of Al^+ and Hg^+ single-ion optical clocks; metrology at the 17th decimal place", Science **319**, 1808 (2008).

[134] W. M. Itano, J. C. Bergquist, J. J. Bollinger, J. M. Gilligan, D. J. Heinzen, F. L. Moore, M. G. Raizen, and D. J. Wineland, "Quantum projection noise: population fluctuations in two-level systems", Phys. Rev. A **47**, 3554 (1993).

[135] G. Wilpers, T. Binnewies, C. Degenhardt, U. Sterr, J. Helmcke, and F. Riehle, "Optical clock with ultracold neutral atoms", Phys. Rev. Lett. **89**, 230801 (2002).

[136] T. Udem, S. A. Diddams, K. R. Vogel, C. W. Oates, E. A. Curtis, W. D. Lee, W. M. Itano, R. E. Drullinger, J. C. Bergquist, and L. Hollberg, "Absolute frequency measurements of the Hg^+ and Ca optical clock transitions with a femtosecond laser", Phys. Rev. Lett. **86**, 4996 (2001).

[137] F. Ruschewitz, J. L. Peng, H. Hinderthür, N. Schaffrath, K. Sengstock, and W. Ertmer, "Sub-kilohertz optical spectroscopy with a time domain atom interferometer", Phys. Rev. Lett. **80**, 3173 (1998).

[138] H. Katori, M. Takamoto, V. G. Pal'chikov, and V. D. Ovsiannikov, "Ultrastable optical clock with neutral atoms in an engineered light shift trap", Phys. Rev. Lett. **91**, 173005 (2003).

[139] M. Takamoto, F.-L. Hong, R. Higashi, and H. Katori, "An optical lattice clock", Nature **435**, 321 (2005).

[140] S. L. Campbell, R. B. Hutson, G. E. Marti, A. Goban, N. Darkwah Oppong, R. L. McNally, L. Sonderhouse, J. M. Robinson, W. Zhang, B. J. Bloom, and J. Ye, "A fermi-degenerate three-dimensional optical lattice clock", Science **358**, 90 (2017).

[141] P. Delva, J. Lodewyck, S. Bilicki, E. Bookjans, G. Vallet, R. Le Targat, P.-E. Pottie, C. Guerlin, F. Meynadier, C. Le Poncin-Lafitte, O. Lopez, A. Amy-Klein, W.-K. Lee, N. Quintin, C. Lisdat, A. Al-Masoudi, S. Dörscher, C. Grebing, G. Grosche, A. Kuhl, S. Raupach, U. Sterr, I. R. Hill, R. Hobson, W. Bowden, J. Kronjäger, G. Marra, A. Rolland, F. N. Baynes, H. S. Margolis, and P. Gill, "Test of special relativity using a fiber network of optical clocks", Phys. Rev. Lett. **118**, 221102 (2017).

[142] C. W. Chou, D. B. Hume, T. Rosenband, and D. J. Wineland, "Optical Clocks and Relativity", Science **329**, 1630 (2010).

[143] S. Kolkowitz, I. Pikovski, N. Langellier, M. D. Lukin, R. L. Walsworth, and J. Ye, "Gravitational wave detection with optical lattice atomic clocks", Phys. Rev. D **94**, 124043 (2016).

[144] A. Derevianko, B. Obreshkov, and V. A. Dzuba, "Mapping out atom-wall interaction with atomic clocks", Phys. Rev. Lett. **103**, 133201 (2009).

[145] S. G. Karshenboim, "Some possibilities for laboratory searches for variations of fundamental constants", Canadian Journal of Physics **78**, 639 (2000).

[146] N. Nemitz, T. Ohkubo, M. Takamoto, I. Ushijima, M. Das, N. Ohmae, and H. Katori, "Frequency ratio of Yb and Sr clocks with 5×10^{-17} uncertainty at 150 seconds averaging time", Nat. Photon. **10**, Letter, 258 (2016).

[147] A. D. Ludlow, M. M. Boyd, J. Ye, E. Peik, and P. O. Schmidt, "Optical atomic clocks", Rev. Mod. Phys. **87**, 637 (2015).

[148] D. A. Jennings, K. M. Evenson, and D. J. E. Knight, "Optical frequency measurements", Proceedings of the IEEE **74**, 168 (1986).

[149] H. Schnatz, B. Lipphardt, J. Helmcke, F. Riehle, and G. Zinner, "First phase-coherent frequency measurement of visible radiation", Phys. Rev. Lett. **76**, 18 (1996).

[150] T. Udem, R. Holzwarth, and T. Hänsch, "Femtosecond optical frequency combs", The European Physical Journal Special Topics **172**, 69 (2009).

[151] M. Zimmermann, C. Gohle, R. Holzwarth, T. Udem, and T. W. Hänsch, "Optical clockwork with an offset-free difference-frequency comb: accuracy of sum- and difference-frequency generation", Opt. Lett. **29**, 310 (2004).

[152] H. Katori, T. Ido, Y. Isoya, and M. Kuwata-Gonokami, "Magneto-optical trapping and cooling of strontium atoms down to the photon recoil temperature", Phys. Rev. Lett. **82**, 1116 (1999).

[153] M. Takamoto and H. Katori, "Spectroscopy of the ${}^1S_0$–${}^3P_0$ clock transition of ^{87}Sr in an optical lattice", Phys. Rev. Lett. **91**, 223001 (2003).

[154] S. Stellmer and F. Schreck, "Reservoir spectroscopy of $5s5p\ {}^3P_2 - 5snd\ {}^3D_{1,2,3}$ transitions in strontium", Phys. Rev. A **90**, 022512 (2014).

[155] A. V. Taichenachev, V. I. Yudin, C. W. Oates, C. W. Hoyt, Z. W. Barber, and L. Hollberg, “Magnetic field-induced spectroscopy of forbidden optical transitions with application to lattice-based optical atomic clocks”, Phys. Rev. Lett. **96**, 083001 (2006).

[156] D. W. Allan, “Statistics of atomic frequency standards”, Proceedings of the IEEE **54**, 221 (1966).

[157] M. S. Safronova, S. G. Porsev, U. I. Safronova, M. G. Kozlov, and C. W. Clark, “Blackbody-radiation shift in the Sr optical atomic clock”, Phys. Rev. A **87**, 012509 (2013).

[158] T. L. Nicholson, S. L. Campbell, R. B. Hutson, G. E. Marti, B. J. Bloom, R. L. McNally, W. Zhang, M. D. Barrett, M. S. Safronova, G. F. Strouse, W. L. Tew, and J. Ye, “Systematic evaluation of an atomic clock at 2×10^{-18} total uncertainty”, **6**, Article, 6896 (2015).

[159] I. Ushijima, M. Takamoto, M. Das, T. Ohkubo, and H. Katori, “Cryogenic optical lattice clocks”, Nat. Photon. **9**, Letter, 185 (2015).

[160] M. S. Safronova, M. G. Kozlov, and C. W. Clark, “Blackbody radiation shifts in optical atomic clocks”, IEEE Transactions on Ultrasonics, Ferroelectrics, and Frequency Control **59**, 439 (2012).

[161] J. Dick, “Local oscillator induced instabilities in trapped ion frequency standards”, Proceedings of the 19th Precise Time and Time Interval Systems and Applications Meeting, 133 (1987).

[162] G. Santarelli, C. Audoin, A. Makdissi, P. Laurent, G. J. Dick, and A. Clairon, “Frequency stability degradation of an oscillator slaved to a periodically interrogated atomic resonator”, IEEE Transactions on Ultrasonics, Ferroelectrics, and Frequency Control **45**, 887 (1998).

[163] M. Takamoto, T. Takano, and H. Katori, “Frequency comparison of optical lattice clocks beyond the Dick limit”, Nat. Photon. **5**, 288 (2011).

[164] T. Akatsuka, M. Takamoto, and H. Katori, “Three-dimensional optical lattice clock with bosonic ^{88}Sr atoms”, Phys. Rev. A **81**, 023402 (2010).

[165] B. J. Bloom, T. L. Nicholson, J. R. Williams, S. L. Campbell, M. Bishof, X. Zhang, W. Zhang, S. L. Bromley, and J. Ye, “An optical lattice clock with accuracy and stability at the 10^{-18} level”, Nature **506**, 71 (2014).

[166] N. Hinkley, J. A. Sherman, N. B. Phillips, M. Schioppo, N. D. Lemke, K. Beloy, M. Pizzocaro, C. W. Oates, and A. D. Ludlow, “An atomic clock with 10^{-18} instability”, Science **341**, 1215 (2013).

[167] S. Falke, N. Lemke, C. Grebing, B. Lipphardt, S. Weyers, V. Gerginov, N. Huntemann, C. Hagemann, A. Al-Masoudi, S. Häfner, S. Vogt, U. Sterr, and C. Lisdat, “A strontium lattice clock with 3×10^{-17} inaccuracy and its frequency”, New Journal of Physics **16**, 073023 (2014).

[168] G. D. Cole, W. Zhang, M. J. Martin, J. Ye, and M. Aspelmeyer, “Tenfold reduction of Brownian noise in high-reflectivity optical coatings”, Nat. Photon. **7**, Article, 644 (2013).

[169] T. Kessler, C. Hagemann, C. Grebing, T. Legero, U. Sterr, F. Riehle, M. J. Martin, L. Chen, and J. Ye, "A sub-40-mhz-linewidth laser based on a silicon single-crystal optical cavity", Nat. Photon. **6**, 687 (2012).

[170] A. Quessada, R. P. Kovacich, I. Courtillot, A. Clairon, G. Santarelli, and P. Lemonde, "The Dick effect for an optical frequency standard", Journal of Optics B: Quantum and Semiclassical Optics **5**, S150 (2003).

[171] M. Schioppo, R. C. Brown, W. F. McGrew, N. Hinkley, R. J. Fasano, K. Beloy, T. H. Yoon, G. Milani, D. Nicolodi, J. A. Sherman, N. B. Phillips, C. W. Oates, and A. D. Ludlow, "Ultrastable optical clock with two cold-atom ensembles", Nat. Photon. **11**, 48 (2017).

[172] J. Lodewyck, P. G. Westergaard, and P. Lemonde, "Nondestructive measurement of the transition probability in a Sr optical lattice clock", Phys. Rev. A **79**, 061401 (2009).

[173] M. Yasuda and H. Katori, "Lifetime measurement of the $^3P_2$ metastable state of strontium atoms", Phys. Rev. Lett. **92**, 153004 (2004).

[174] J. Lee, J. H. Lee, J. Noh, and J. Mun, "Core-shell magneto-optical trap for alkaline-earth-metal-like atoms", Phys. Rev. A **91**, 053405 (2015).

[175] A. Kawasaki, B. Braverman, Q. Yu, and V. Vuletic, "Two-color magneto-optical trap with small magnetic field for ytterbium", Journal of Physics B: Atomic, Molecular and Optical Physics **48**, 155302 (2015).

[176] W. Ketterle, D. S. Durfee, and D. M. Stamper-Kurn, "Making, probing and understanding Bose-Einstein condensates", eprint arXiv:cond-mat/9904034 (1999).

[177] A. Farolfi, "Realization of a Magneto-Optical-Trap for Strontium", MSc thesis (Eberhard Karls Universität Tübingen, 2017).

[178] J. Fortágh, *Project 7: Long-range Rydberg interactions mediated by a microwave cavity at finite temperature*, `http://giryd.de/en/projects.php/_/7/`.

[179] M. Mohseni, P. Read, H. Neven, S. Boixo, V. Denchev, R. Babbush, A. Fowler, V. Smelyanskiy, and J. Martinis, *Commercialize quantum technologies in five years*, (Mar. 2017) `https://www.nature.com/news/commercialize-quantum-technologies-in-five-years-1.21583`.

[180] D. Meiser, J. Ye, D. R. Carlson, and M. J. Holland, "Prospects for a millihertz-linewidth laser", Phys. Rev. Lett. **102**, 163601 (2009).

[181] D. Meiser and M. J. Holland, "Steady-state superradiance with alkaline-earth-metal atoms", Phys. Rev. A **81**, 033847 (2010).

[182] M. A. Norcia and J. K. Thompson, "Cold-strontium laser in the superradiant crossover regime", Phys. Rev. X **6**, 011025 (2016).

A Appended publications

PHYSICAL REVIEW A **90**, 053416 (2014)

Controlling the magnetic-field sensitivity of atomic-clock states by microwave dressing

L. Sárkány, P. Weiss, H. Hattermann,* and J. Fortágh
CQ Center for Collective Quantum Phenomena and their Applications, Physikalisches Institut, Eberhard Karls Universität Tübingen,
Auf der Morgenstelle 14, D-72076 Tübingen, Germany
(Received 18 September 2014; published 13 November 2014)

We demonstrate control of the differential Zeeman shift between clock states of ultracold rubidium atoms by means of nonresonant microwave dressing. Using the dc field dependence of the microwave detuning, we suppress the first- and second-order differential Zeeman shift in magnetically trapped ^{87}Rb atoms. By dressing the state pair $5S_{1/2}$ $F=1$, $m_F=-1$ and $F=2$, $m_F=1$, a residual frequency spread of <0.1 Hz in a range of 100 mG around a chosen magnetic offset field can be achieved. This is one order of magnitude smaller than the shift of the bare states at the magic field of the Breit-Rabi parabola. We further identify *double magic* points, around which the clock frequency is insensitive to fluctuations both in the magnetic field and in the dressing Rabi frequency. The technique is compatible with chip-based cold-atom systems and allows the creation of clock and qubit states with reduced sensitivity to magnetic-field noise.

DOI: 10.1103/PhysRevA.90.053416 PACS number(s): 32.60.+i, 32.30.Bv, 37.25.+k, 06.30.Ft

I. INTRODUCTION

The sensitivity of atomic transitions to external field perturbations represents a major limitation for the accuracy and stability of atomic clocks [1,2] and for the time of quantum-information storage in ultracold atoms and atomic gases [3–5]. Electromagnetic-field fluctuations and inhomogeneous trapping potentials give rise to temporal and spatial variations of atomic transition frequency. A common approach to reduce the frequency broadening observed in the preparation and readout of atomic superposition states is the use of "magic" magnetic fields [6,7] and wavelengths [8–10] for which the differential Zeeman and Stark shifts of a state pair are minimized, respectively. In addition, density-dependent collisional shifts [11,12] and the effect of identical spin rotation [13–15] have been shown to counteract inhomogeneous dephasing of superposition states in trapped atomic clouds. Possible realizations of cold-atom quantum memories on atom chips [15–19] and chip-based atomic clocks [12,20–22] have to face additional perturbations due to the proximate solid surface [23]. Controlling differential shifts between clock states is one of the key requirements for the realization of a coherent interface between cold atoms and solid-state quantum electronic circuits [24–32]. It was recently shown that Rydberg states can be rendered insensitive to small variations of electric fields by microwave (MW) dressing [33]. Previously, radio-frequency dressing of nuclear spins has been proposed to cancel differential Zeeman shifts between optical clock transitions [34]. Microwave fields have further been used to suppress the magnetic-field dependency of qubit states in trapped ions [35] and nitrogen-vacancy centers with both pulsed [36,37] and continuous [38,39] decoupling schemes.

Here, we demonstrate the control and suppression of the differential Zeeman shift between atomic qubit states up to second order by microwave dressing, thereby reducing the magnetic-field sensitivity of the clock transition frequency. The technique does not require the state pair to be close to magic magnetic fields but can be applied for a wide range of chosen magnetic offset fields in the trap. By dressing the state pair $5S_{1/2}$ $F=1$, $m_F=-1$ and $F=2$, $m_F=1$ of ^{87}Rb, we demonstrate that a variation of <0.1 Hz over a magnetic field range of >100 mG can be achieved, one order of magnitude less than the differential shift of the bare states around the magic offset field. In addition, we demonstrate the existence of points where this dressing becomes insensitive to fluctuations in the dressing Rabi frequency, enabling the generation of noise-protected qubit states. Our model and experimental results show that the frequency of an atomic clock can be engineered by microwave dressing to achieve arbitrary curvatures, e.g., nearly zero differential shift, around a given magnetic offset field.

II. MICROWAVE DRESSING OF ATOMIC TRANSITIONS

In static magnetic fields, the degeneracy of the hyperfine levels of ground-state alkali-metal atoms is lifted according to the Breit-Rabi formula [40]. In small and intermediate fields, the Zeeman effect can be expanded in terms linear and quadratic in the magnetic-field strength. The interaction of the atom with nonresonant ac electromagnetic fields leads to the ac shift of the levels, which depends on the detuning, e.g., $\Delta E \propto \Omega_{\mathrm{dress}}^2/\Delta_{\mathrm{dress}}$. As this detuning depends on the dc Zeeman shift of the levels, a suitable choice of the microwave field allows for compensation of spatial and temporal variations of the differential Zeeman shift.

While the technique presented here can be applied for all alkali-metal elements, we now discuss this for the specific case of ^{87}Rb. The two-photon transition $5S_{1/2}$ $F=1, m_F=-1 \rightarrow F=2, m_F=1$ is commonly used as an atomic-clock transition for magnetically trapped ^{87}Rb. Both states exhibit nearly the same first-order Zeeman shift, starkly reducing the sensitivity of the transition to magnetic-field fluctuations and making the two states ideal candidates as atomic qubit states. The energy of the two states $|0\rangle \equiv 5S_{1/2}$ $F=1, m_F=-1$ and $|1\rangle \equiv 5S_{1/2}$ $F=2, m_F=1$ in a magnetic field of magnitude B is given by

$$E_0/\hbar = \mu_1 B - 3\beta B^2 \tag{1}$$

---

*hattermann@pit.physik.uni-tuebingen.de

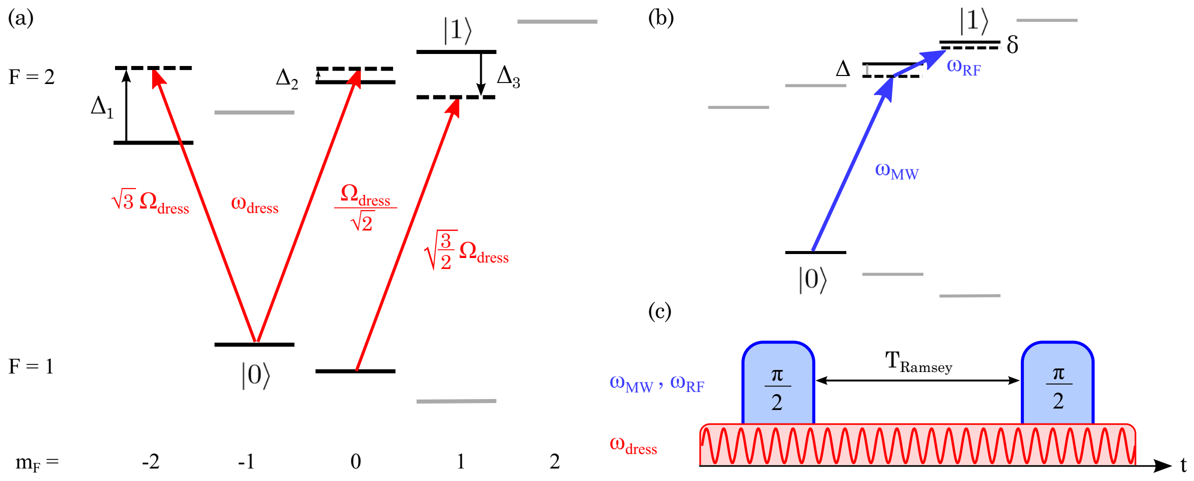

FIG. 1. (Color online) (a) Ground-state hyperfine structure and Zeeman sublevels of ^{87}Rb in a magnetic field. A microwave field of frequency ω_{dress} and Rabi frequency Ω_{dress} is used for dressing the clock transition. (b) The atomic transition is probed by means of Ramsey interferometry. A two-photon pulse with $\omega_{\text{MW}} \approx 6.833$ GHz and $\omega_{\text{RF}} \approx 2$ MHz is used to drive the transition. (c) Schematic of the experimental sequence. A $\pi/2$ pulse is used to prepare the atoms in a superposition state $1/\sqrt{2} \times (|0\rangle + |1\rangle)$. After a variable hold time T_{Ramsey}, the interferometer is closed by the application of a second $\pi/2$ pulse and the population of the two states, oscillating with frequency δ, is measured. The dressing field is left on throughout the interferometer sequence.

and

$$E_1/\hbar = \mu_2 B + 3\beta B^2 + \omega_0, \qquad (2)$$

where $\mu_1 = 2\pi \times 702.37$ kHz/G, $\mu_2 = 2\pi \times 699.58$ kHz/G, $\beta = 2\pi \times 71.89$ Hz/G^2, and $\omega_0 = 2\pi \times 6.8346826109$ GHz [41] is the frequency difference of the two states in the absence of any fields. The energy difference between the two levels can be expressed by

$$\Delta E_{0,1}/\hbar = 6\beta(B - B_0)^2 + 2\pi \times 6.8346781136\ \text{GHz}, \quad (3)$$

where $B_0 \approx 3.229$ G is the so-called magic offset field [42]. Using microwave dressing of the Zeeman sublevels with an appropriate frequency ω_{dress} and Rabi frequency Ω_{dress}, the second-order Zeeman shift can be compensated for.

The microwave field leads to a correction of the form

$$\Delta E_{\text{dress},i} = \hbar \sum_{i,\alpha} \frac{\Omega_{i,\alpha}^2}{\Delta_{i,\alpha}} \qquad (4)$$

for both of the states i, where $\alpha = \sigma_+,\sigma_-,\pi$ denotes all the possible polarizations of the dressing field, for which the relevant detuning Δ_α and Rabi frequency Ω_α need to be taken into account for each. If we consider a microwave field $B_{\text{dress}} \cos(\omega_{\text{dress}} t)$, which is linearly polarized perpendicular to the quantization axis (given by the magnetic offset field), the situation is simplified, as we only need to take into account σ_+ and σ_- transitions, as sketched in Fig. 1(a). In the rotating-wave approximation, the Hamiltonian relevant for the two states is

$$H_0 = \hbar \begin{bmatrix} 0 & \sqrt{3}\Omega_{\text{dress}} & \frac{1}{\sqrt{2}}\Omega_{\text{dress}} \\ \sqrt{3}\Omega_{\text{dress}} & -\Delta_1 & 0 \\ \frac{1}{\sqrt{2}}\Omega_{\text{dress}} & 0 & -\Delta_2 \end{bmatrix} \qquad (5)$$

and

$$H_1 = \hbar \begin{bmatrix} 0 & \sqrt{\frac{3}{2}}\Omega_{\text{dress}} \\ \sqrt{\frac{3}{2}}\Omega_{\text{dress}} & -\Delta_3 \end{bmatrix}, \qquad (6)$$

where we have defined Ω_{dress} as state-independent Rabi frequency

$$\Omega_{\text{dress}} = \frac{1}{2\sqrt{2}\hbar} \mu_B\, g_F\, |B_{\text{dress}}|, \qquad (7)$$

and the values of the detunings in Eqs. (5) and (6) and Fig. 1(a) are given by

$$\Delta_1 = \Delta_{\text{dress}} + (\mu_1 + 2\mu_2)B - 3\beta B^2, \qquad (8)$$

$$\Delta_2 = \Delta_{\text{dress}} + \mu_1 B - 7\beta B^2, \qquad (9)$$

$$\Delta_3 = \Delta_{\text{dress}} - \mu_2 B - 7\beta B^2, \qquad (10)$$

where $\Delta_{\text{dress}} = \omega_{\text{dress}} - \omega_0$. With this notation, we can write the frequency difference between the two states as

$$\Delta E_{0,1}/\hbar = \omega_0 + (\mu_2 - \mu_1)B + 6\beta B^2 + \cdots + \Omega_{\text{dress}}^2 \left(\frac{3}{\Delta_1(B)} + \frac{1/2}{\Delta_2(B)} - \frac{3/2}{\Delta_3(B)} \right). \qquad (11)$$

For a given offset field, it is now possible to find numerical solutions ω_{dress} and Ω_{dress} for which the first and second derivatives of Eq. (11) with respect to B disappear; i.e., the Zeeman shift of the transitions around that offset field is canceled up to second order. This is illustrated in Fig. 2, where the frequency difference is plotted as a function of the magnetic field for different values of the center of the plateau, B_{center}. For each curve, different optimized values for ω_{dress} and Ω_{dress} were calculated. The choice of B_{center} is completely arbitrary within the limits of Rabi frequencies Ω_{dress} that are achievable in experimental conditions.

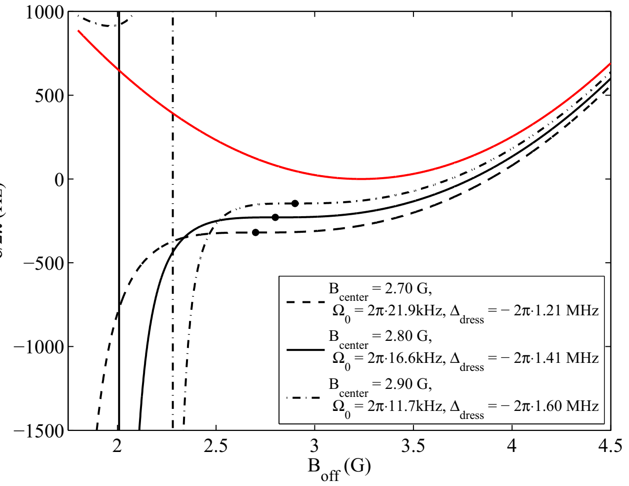

FIG. 2. (Color online) Calculated frequency difference of the clock transition as a function of the magnetic field. The Breit-Rabi parabola for the case without the dressing field is plotted in red. The three black curves show the cancellation of the B_{off} dependence around three different central values B_{center}. For an arbitrary value of B_{center}, the optimal detuning and Rabi frequency can be calculated.

III. EXPERIMENTAL PROCEDURE

The measurements are taken with atomic clouds magnetically trapped on a superconducting atom chip. Atoms are loaded into this trap as follows [15]: an ensemble of ultracold ^{87}Rb atoms is prepared in a magneto-optical trap and subsequently transferred into an Ioffe-Pritchard-type magnetic trap situated in the room-temperature environment of our setup [43]. The atomic cloud is cooled by forced radio-frequency evaporation and then loaded into an optical dipole trap used to transport the ensemble to a position below the superconducting atom chip at 4.2 K. We load an ensemble of $\sim 1 \times 10^6$ atoms at a temperature of $\sim 1\ \mu$K into the magnetic chip trap, which is based on a Z-wire geometry [23]. The oscillation frequencies in the trap are given by $\omega_x = 2\pi \times 30\ \mathrm{s}^{-1}$, $\omega_y = 2\pi \times 158\ \mathrm{s}^{-1}$, and $\omega_z = 2\pi \times 155\ \mathrm{s}^{-1}$, and the offset field B_{off}, which defines the quantization axis, is pointing along the x direction. The atomic cloud in the magnetic trap is cooled to a temperature of ~250 nK by evaporation. After this sequence, which is repeated every ~23 s, we end up with an ensemble of roughly 1×10^5 atoms. After a hold time of 2 s in the magnetic trap, which allows for damping of possible eddy currents in the metallic chip holder, a microwave field for dressing is applied.

The microwave field is irradiated from an antenna outside of the vacuum chamber and is counterpropagating to the quantization axis. We measured the polarization of the microwave by driving resonant σ_+ and σ_- Rabi oscillations. We found a ratio of $\sqrt{6}\Omega_{0,\sigma+}/\Omega_{0,\sigma-} \approx 0.81$, while for a linear (circular) polarization the expected ratio would be 1 (0). The factor $\sqrt{6}$ stems from the different transition strengths, as visible in the Hamiltonian in Eq. (5).

The frequency of the transition is measured by means of Ramsey interferometry. The interferometric sequence is started 100 ms after switching on the dressing field by applying a combined microwave and radio-frequency two-photon pulse with a pulse area of $\pi/2$ ($T_{\pi/2} = 137\ \mu$s), which prepares the atomic ensemble in a coherent superposition of states $|0\rangle$ and $|1\rangle$; see Figs. 1(b) and 1(c). The microwave pulses are irradiated from a second external antenna with a wave vector perpendicular to the quantization axis, while the radio-frequency field is generated by an alternating current in the trapping wire. Both frequencies are chosen with a detuning of $\Delta \sim 2\pi \times 310$ kHz with respect to the transition to the intermediate level $5S_{1/2}\ F = 2, m_F = 0$, so that the probability of populating this level is negligible. After a variable hold time T_{Ramsey}, the interferometer is closed by a second $\pi/2$ pulse and we measure the population of the two states $|0\rangle$ and $|1\rangle$, which oscillates with the angular frequency $\delta = |\omega_{\mathrm{MW}} + \omega_{\mathrm{RF}} - \Delta E_{0,1}/\hbar|$. We determine this frequency δ for different offset fields B_{off} and seek to eliminate the magnetic-field dependence of the transition.

IV. MEASUREMENTS AND DISCUSSION

To demonstrate the control over the differential Zeeman shift, we measure the frequency of the Ramsey interferometer as a function of the magnetic offset field B_{off} for different powers of the dressing field (Fig. 3). For each value of B_{off}, we adjust ω_{RF} and ω_{MW} in order to keep the detuning Δ to the intermediate-state constant, while keeping the sum frequency

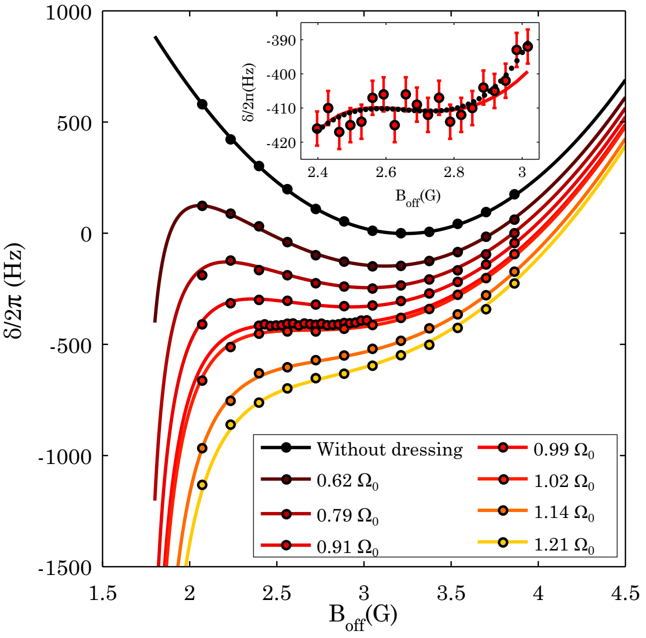

FIG. 3. (Color online) Measurement of the differential Zeeman shift between the states $|0\rangle$ and $|1\rangle$ for different Rabi frequencies. The frequency zero point was set to the frequency at the magic offset field without dressing. For a Rabi frequency $\Omega_{\mathrm{dress}} = \Omega_0 = 2\pi \times 20.1$ kHz, the frequency is nearly independent of the magnetic offset field in a range of ±100 mG around the chosen value $B_{\mathrm{center}} = 2.65$ G. Inset: Detail of the curve with $\Omega_{\mathrm{dress}} = 0.99\Omega_0$. We estimate a measurement error of ±5 Hz resulting from fluctuations of the MW power. The theory curve (solid red line) is plotted along a polynomial fit (dotted black line), showing the suppression of the first- and second-order Zeeman shift down to a level of -7.3 Hz/G and 5.0 Hz/G^2.

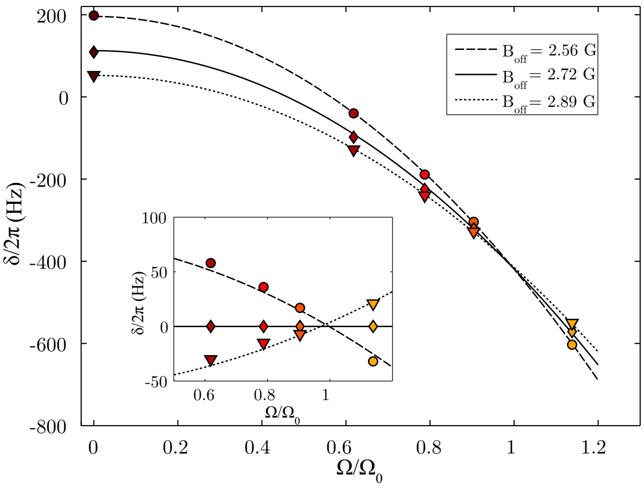

FIG. 4. (Color online) Frequency difference of the clock transition as a function of the Rabi frequency of the dressing for different magnetic fields. The data was extracted from the measurements in Fig. 3. *Inset*: Frequency difference for different offset fields with respect to the measurements at $B_{\mathrm{off}} = 2.72$ G as a function of the Rabi frequency. At the optimal Rabi frequency Ω_0, the three curves show nearly identical frequencies, proving the cancellation of the differential Zeeman shift up to second order.

$\omega_{\mathrm{RF}} + \omega_{\mathrm{MW}}$ fixed. The measurement without dressing field yields the expected Breit-Rabi parabola which we use to calibrate the magnetic field B_{off}.

For the cancellation of the magnetic-field dependence, a magnetic offset field $B_{\mathrm{off}} = 2.65$ G was chosen. For this B_{off}, we calculated the optimum detuning Δ_{dress} and Rabi frequency Ω_{dress} for the measured ratio between σ_+ and σ_- transition strengths. We measure δ vs B_{off} in the range 2.1–3.8 G for Rabi frequencies in the range of $2\pi \times 12$ to $2\pi \times 25$ kHz with a calculated optimal Rabi frequency $\Omega_0 = 2\pi \times 20.1$ kHz. The results of these measurements are plotted in Fig. 3 along with the results of the analytical calculations, taking into account the measured imbalance in the Rabi frequency. The theory lines are obtained by leaving the Rabi frequency as a free parameter in one of the curves and scaling the other curves according to the MW power applied in the experiment. The data demonstrate the compensation of the differential Zeeman shift around the field value of $B_{\mathrm{center}} = 2.65$ G.

The reduced sensitivity of the clock transition to magnetic-field variations is shown in Fig. 4. Here we plot the measured frequencies and the theory curves for three different offset fields as a function of the Rabi frequency, as extracted from the values in Fig. 3. For the optimum Rabi frequency Ω_0, all three curves show the same ac Zeeman shift. The inset in Fig. 4 shows the frequency difference between the curves measured for the three offset fields with respect to the value $B_{\mathrm{off}} = 2.72$ G. The three curves cross nearly at the same point, showing the strong suppression of the differential Zeeman shift over a field range larger than 0.2 G. The analysis of the theory curves in Fig. 3 shows that it is possible to generate plateaus where the frequency differs by less than 0.1 Hz over a magnetic-field range of more than 100 mG. As is visible in the inset of Fig. 3, the measurement does not reach this accuracy. We estimate a frequency uncertainty of ±5 Hz, based on the limited time between the Ramsey pulses and the uncertainty of the unstabilized microwave power.

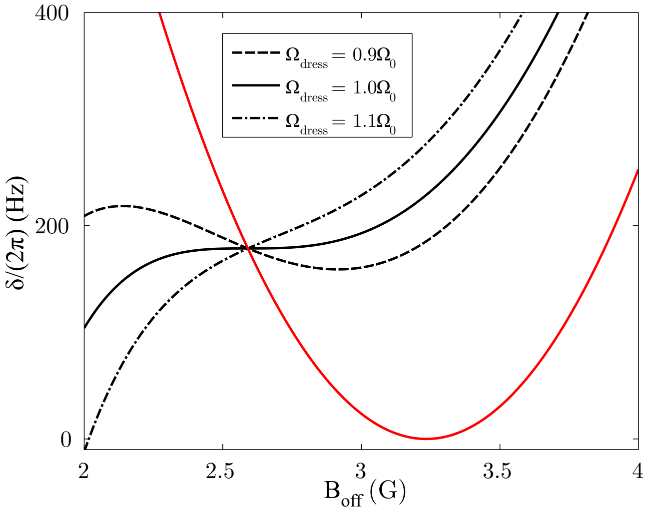

FIG. 5. (Color online) *Double magic* dressing of the atomic-clock transition, for which the dependence of the frequency on both the magnetic field and the Rabi frequency disappears around a field value of $B_{\mathrm{center}} = 2.59$ G. The calculation assumes a Rabi-frequency imbalance of $\sqrt{6}\Omega_{0,\sigma+}/\Omega_{0,\sigma-} = 1.25$, and the obtained optimal parameters are $\Omega_0 = 2\pi \times 86.7$ kHz, $\Delta_{\mathrm{dress}} = -2\pi \times 309$ kHz.

The stability of the microwave Rabi frequency is expected to be the strongest limitation on the frequency stability. In order to reach the 0.1-Hz range at the field point of 2.65 G, a power stability on the order of $\Delta\Omega_{\mathrm{dress}}/\Omega_{\mathrm{dress}} \sim 1 \times 10^{-4}$ would be required. For certain offset fields, however, it is possible to find solutions for Eq. (11) where both the B-field dependency as well as the dependency on the Rabi frequency Ω_{dress} disappear. An example for such a solution can be seen in Fig. 5: Here, we calculate that the transition frequency varies by less than ±0.1 Hz over a range of 100 mG around $B_{\mathrm{center}} = 2.59$ G. At the center of the plateau, the frequency δ becomes independent of the Rabi frequency for a detuning of $\Delta_{\mathrm{dress}} = -2\pi \times 309$ kHz. In a range of ±10 mG around B_{center}, a Rabi-frequency stabilization on the order of 1% would be sufficient to reach a level of 0.1-Hz stability. Such *double magic* dressing enables the employment of this technique with on-chip microwave devices, where Rabi frequencies are inversely proportional to the distance to the chip.

Manipulation of the differential Zeeman shift can be used to decrease the frequency spread over the size of the cloud. For a cloud of $N = 5 \times 10^4$ atoms at $T = 250$ nK and $B_{\mathrm{off}} = 2.65$ G, the standard deviation of the frequency distribution due to the inhomogeneity of the magnetic field without dressing is on the order of $\sigma_{\mathrm{inh}} \approx 4$ Hz, about an order of magnitude larger than the spread σ_{dens} caused by the inhomogeneous mean-field interaction due to the density distribution in the trap [12]. Microwave dressing can be employed to decrease σ_{inh} to a level on the order of σ_{dens}, thereby balancing the two effects and leading to a nearly homogeneous frequency over the size of the cloud. For the parameters above and our trap, we calculate that the differential Zeeman shift can be engineered to cancel the collisional frequency shift down to a level of $\sigma \approx 2\pi \times 0.25$ Hz.

In addition, our scheme can be used to prepare states with nearly arbitrary δ vs B_{off} curvatures around the desired field point, enabling one to suppress, enhance, or spatially structure the differential Zeeman shifts. Enhancing the B-field dependence could, for example, be used to counteract the strong mean-field shifts in a Bose-Einstein condensate. Further engineering of differential clock frequencies can be achieved by using multifrequency microwave fields. This opens up new possibilities for microwave and radio-frequency dressing of atomic transitions, which has previously been used for trapping and manipulation of cold atoms [44–48] and the generation of state-dependent potentials [49,50].

V. CONCLUSION

In summary, we have shown both experimentally and theoretically that dressing of Zeeman sublevels in magnetically trapped atoms can render hyperfine transitions insensitive to magnetic-field fluctuations around an arbitrary field value. We have furthermore identified double magic points, where the clock frequency becomes independent of the Rabi frequency. Microwave dressing can be used to enhance the coherence time of quantum superposition states in arbitrary magnetic fields and for the creation of noise-protected quantum memories. The scheme is further applicable in atomic-clock schemes in magnetically noisy environments or portable setups.

ACKNOWLEDGMENTS

The authors would like to thank Rainer Dumke and Thomas Judd for useful discussions. This work was supported by the Deutsche Forschungsgemeinschaft (SFB TRR21) and the European Commission (FP7 STREP project "HAIRS").

---

[1] B. J. Bloom, T. L. Nicholson, J. R. Williams, S. L. Campbell, M. Bishof, X. Zhang, W. Zhang, S. L. Bromley, and J. Ye, Nature (London) **506**, 71 (2014).

[2] I. Ushijima, M. Takamoto, M. Das, T. Ohkubo, and H. Katori, arXiv:1405.4071.

[3] R. Zhao, Y. O. Dudin, S. D. Jenkins, C. J. Campbell, D. N. Matsukevich, T. A. B. Kennedy, and A. Kuzmich, Nat. Phys. **5**, 100 (2009).

[4] X.-H. Bao, A. Reingruber, P. Dietrich, J. Rui, A. Dück, T. Strassel, L. Li, N.-L. Liu, B. Zhao, and J.-W. Pan, Nat. Phys. **8**, 517 (2012).

[5] Y. O. Dudin, L. Li, and A. Kuzmich, Phys. Rev. A **87**, 031801 (2013).

[6] D. M. Harber, H. J. Lewandowski, J. M. McGuirk, and E. A. Cornell, Phys. Rev. A **66**, 053616 (2002).

[7] A. Derevianko, Phys. Rev. Lett. **105**, 033002 (2010).

[8] H. Katori, M. Takamoto, V. G. Pal'chikov, and V. D. Ovsiannikov, Phys. Rev. Lett. **91**, 173005 (2003).

[9] H. Katori, Nat. Photonics **5**, 203 (2011).

[10] R. Chicireanu, K. D. Nelson, S. Olmschenk, N. Lundblad, A. Derevianko, and J. V. Porto, Phys. Rev. Lett. **106**, 063002 (2011).

[11] P. Treutlein, P. Hommelhoff, T. Steinmetz, T. W. Hänsch, and J. Reichel, Phys. Rev. Lett. **92**, 203005 (2004).

[12] P. Rosenbusch, Appl. Phys. B **95**, 227 (2009).

[13] C. Deutsch, F. Ramirez-Martinez, C. Lacroûte, F. Reinhard, T. Schneider, J. N. Fuchs, F. Piéchon, F. Laloë, J. Reichel, and P. Rosenbusch, Phys. Rev. Lett. **105**, 020401 (2010).

[14] G. Kleine Büning, J. Will, W. Ertmer, E. Rasel, J. Arlt, C. Klempt, F. Ramirez-Martinez, F. Piéchon, and P. Rosenbusch, Phys. Rev. Lett. **106**, 240801 (2011).

[15] S. Bernon, H. Hattermann, D. Bothner, M. Knufinke, P. Weiss, F. Jessen, D. Cano, M. Kemmler, R. Kleiner, D. Koelle, and J. Fortágh, Nat. Commun. **4**, 2380 (2013).

[16] J. Verdú, H. Zoubi, C. Koller, J. Majer, H. Ritsch, and J. Schmiedmayer, Phys. Rev. Lett. **103**, 043603 (2009).

[17] K. R. Patton and U. R. Fischer, Phys. Rev. A **87**, 052303 (2013).

[18] K. R. Patton and U. R. Fischer, Phys. Rev. Lett. **111**, 240504 (2013).

[19] Z.-L. Xiang, S. Ashhab, J. Q. You, and F. Nori, Rev. Mod. Phys. **85**, 623 (2013).

[20] D. M. Farkas, A. Zozulya, and D. Z. Anderson, Appl. Phys. B **101**, 705 (2010).

[21] V. Vuletić, I. D. Leroux, and M. H. Schleier-Smith, in *Atom Chips* (Wiley-VCH, Berlin, 2011), pp. 265–282.

[22] F. Ramírez-Martínez, C. Lacroûte, P. Rosenbusch, F. Reinhard, C. Deutsch, T. Schneider, and J. Reichel, Adv. Space Res. **47**, 247 (2011).

[23] J. Fortágh and C. Zimmermann, Rev. Mod. Phys. **79**, 235 (2007).

[24] P. Rabl, D. DeMille, J. M. Doyle, M. D. Lukin, R. J. Schoelkopf, and P. Zoller, Phys. Rev. Lett. **97**, 033003 (2006).

[25] M. Wallquist, K. Hammerer, P. Rabl, M. Lukin, and P. Zoller, Phys. Scr. **2009**, 014001 (2009).

[26] M. Hafezi, Z. Kim, S. L. Rolston, L. A. Orozco, B. L. Lev, and J. M. Taylor, Phys. Rev. A **85**, 020302 (2012).

[27] D. Petrosyan and M. Fleischhauer, Phys. Rev. Lett. **100**, 170501 (2008).

[28] D. Petrosyan, G. Bensky, G. Kurizki, I. Mazets, J. Majer, and J. Schmiedmayer, Phys. Rev. A **79**, 040304 (2009).

[29] D. Braun, J. Hoffman, and E. Tiesinga, Phys. Rev. A **83**, 062305 (2011).

[30] M. Gao, Y.-x. Liu, and X.-B. Wang, Phys. Rev. A **83**, 022309 (2011).

[31] K. Henschel, J. Majer, J. Schmiedmayer, and H. Ritsch, Phys. Rev. A **82**, 033810 (2010).

[32] B. Dóra, F. Pollmann, J. Fortágh, and G. Zaránd, Phys. Rev. Lett. **111**, 046402 (2013).

[33] L. A. Jones, J. D. Carter, and J. D. D. Martin, Phys. Rev. A **87**, 023423 (2013).

[34] T. Zanon-Willette, E. de Clercq, and E. Arimondo, Phys. Rev. Lett. **109**, 223003 (2012).

[35] N. Timoney, I. Baumgart, M. Johanning, A. F. Varón, M. B. Plenio, A. Retzker, and C. Wunderlich, Nature (London) **476**, 185 (2011).

[36] G. de Lange, Z. H. Wang, D. Ristè, V. V. Dobrovitski, and R. Hanson, Science **330**, 60 (2010).

[37] A. M. Souza, G. A. Álvarez, and D. Suter, Phys. Rev. Lett. **106**, 240501 (2011).

[38] X. Xu, Z. Wang, C. Duan, P. Huang, P. Wang, Y. Wang, N. Xu, X. Kong, F. Shi, X. Rong, and J. Du, Phys. Rev. Lett. **109**, 070502 (2012).

[39] J.-M. Cai, B. Naydenov, R. Pfeiffer, L. P. McGuinness, K. D. Jahnke, F. Jelezko, M. B. Plenio, and A. Retzker, New J. Phys. **14**, 113023 (2012).

[40] G. Breit and I. I. Rabi, Phys. Rev. **38**, 2082 (1931).

[41] D. Steck, http://steck.us/alkalidata.

[42] H. J. Lewandowski, D. M. Harber, D. L. Whitaker, and E. A. Cornell, Phys. Rev. Lett. **88**, 070403 (2002).

[43] D. Cano, H. Hattermann, B. Kasch, C. Zimmermann, R. Kleiner, D. Koelle, and J. Fortágh, Eur. Phys. J. D **63**, 17 (2011).

[44] O. Zobay and B. M. Garraway, Phys. Rev. Lett. **86**, 1195 (2001).

[45] Y. Colombe, E. Knyazchyan, O. Morizot, B. Mercier, V. Lorent, and H. Perrin, Europhys. Lett. **67**, 593 (2004).

[46] S. Hofferberth, I. Lesanovsky, B. Fischer, J. Verdu, and J. Schmiedmayer, Nat. Phys. **2**, 710 (2006).

[47] I. Lesanovsky, T. Schumm, S. Hofferberth, L. M. Andersson, P. Krüger, and J. Schmiedmayer, Phys. Rev. A **73**, 033619 (2006).

[48] W. H. Heathcote, E. Nugent, B. T. Sheard, and C. J. Foot, New J. Phys. **10**, 043012 (2008).

[49] P. W. Courteille, B. Deh, J. Fortágh, A. Günther, S. Kraft, C. Marzok, S. Slama, and C. Zimmermann, J. Phys. B: At. Mol. Opt. Phys. **39**, 1055 (2006).

[50] P. Böhi, M. F. Riedel, J. Hoffrogge, J. Reichel, T. W. Hänsch, and P. Treutlein, Nat. Phys. **5**, 592 (2009).

PHYSICAL REVIEW A **97**, 032341 (2018)

Faithful state transfer between two-level systems via an actively cooled finite-temperature cavity

Lőrinc Sárkány,[1] József Fortágh,[1] and David Petrosyan[1,2]
[1]*Physikalisches Institut, Eberhard Karls Universität Tübingen, D-72076 Tübingen, Germany*
[2]*Institute of Electronic Structure and Laser, FORTH, GR-71110 Heraklion, Crete, Greece*

(Received 21 December 2017; published 28 March 2018)

We consider state transfer between two qubits—effective two-level systems represented by Rydberg atoms—via a common mode of a microwave cavity at finite temperature. We find that when both qubits have the same coupling strength to the cavity field, at large enough detuning from the cavity mode frequency, quantum interference between the transition paths makes the SWAP of the excitation between the qubits largely insensitive to the number of thermal photons in the cavity. When, however, the coupling strengths are different, the photon-number-dependent differential Stark shift of the transition frequencies precludes efficient transfer. Nevertheless, using an auxiliary cooling system to continuously extract the cavity photons, we can still achieve a high-fidelity state transfer between the qubits.

DOI: 10.1103/PhysRevA.97.032341

I. INTRODUCTION

Quantum information protocols and quantum simulations with cold atomic systems extensively utilize strong dipole-dipole interaction between the laser-excited Rydberg states of atoms [1–8]. Atoms are routinely trapped and manipulated near the surfaces of superconducting atom chips [9,10] and can couple to on-chip microwave planar resonators [11,12]. Atom chips are typically cooled by liquid helium to the temperature of $T \simeq 4$ K. At such temperatures, the black-body radiation is sufficiently suppressed and does not detrimentally affect the Rydberg state lifetime [3,13,14]. Rydberg qubits then exhibit long coherence times on atom chips [15,16]. This should be contrasted with superconducting qubits that require chips at $T \lesssim 100$ mK temperature to operate [17–19].

Huge electric dipole transitions between the Rydberg states of atoms allow their strong coupling to microwave planar waveguides [20] and resonators [21]. The cavity field can then serve as a quantum bus to mediate long-distance interactions and quantum gates between the Rydberg qubits [22,23]. At $T \simeq 4$ K, however, the microwave cavity or waveguide has a large population of thermal photons. This would preclude long-distance quantum gates and coherent state transfer, unless inherently temperature-resistant schemes are used [24–26].

In this paper we consider a SWAP operation between a pair of Rydberg qubits exchanging a virtual photon via a thermally populated microwave cavity. We show that a high-fidelity state or excitation transfer is only possible if the coupling strengths of both atoms to the cavity mode is the same. In the general case of unequal couplings, the photon-number-dependent Stark shifts of the atomic transitions precludes the state transfer. In order to overcome this problem, we propose to continuously extract thermal photons from the cavity mode using a separate, laser-driven ensemble of cooling atoms. This breaks the symmetry between the cavity field population from the thermal environment and depopulation due to the photon decay and extraction, greatly reducing the effective mode temperature. We find that despite the increased rate of photon decay from the cavity, a high-fidelity SWAP operation between the Rydberg qubits is feasible with a realistic experimental setup.

The paper is organized as follows. In Sec. II we describe the system and show that the excitation transfer between two atoms in nonequivalent positions of a thermal cavity is suppressed. In Sec. III we present a method to reduce the number of thermal photons of the cavity by their continuous extraction with an optically pumped atomic ensemble. In Sec. IV we show that this leads to increased transfer probability between the two atoms, followed by conclusions in Sec. V

II. THE COMPOUND SYSTEM

A. Mathematical formalism

We consider a compound system consisting of two two-level (Rydberg) atoms $i = 1,2$ coupled to a common mode of a microwave resonator, as sketched in Fig. 1(a). The system is thus equivalent to the Jaynes-Cummings model for two atoms interacting with a cavity field [27,28]. In the frame rotating with the frequency of the cavity mode ω, the Hamiltonian is given by

$$\mathcal{H}/\hbar = \sum_{i=1,2} \left[\tfrac{1}{2}\Delta_i\left(\hat{\sigma}_{bb}^{(i)} - \hat{\sigma}_{aa}^{(i)}\right) + g_i\left(\hat{c}\hat{\sigma}_{ba}^{(i)} + \hat{\sigma}_{ab}^{(i)}\hat{c}^{\dagger}\right)\right]. \quad (1)$$

Here $\Delta_i \equiv \omega_{ba}^{(i)} - \omega$ is the detuning of atom i on the transition $|a\rangle \leftrightarrow |b\rangle$ from the cavity mode frequency, $\hat{\sigma}_{\mu\nu}^{(i)} \equiv |\mu\rangle_i\langle\nu|$ $(\mu,\nu = a,b)$ are atomic operators, and g_i is the coupling strength of atom i to the cavity mode described by the photon creation $\hat{c}^{\dagger}$ and annihilation $\hat{c}$ operators. The coupling strength $g_i = (\wp_{ab}/\hbar)\varepsilon_c u(\mathbf{r}_i)$ is proportional to the dipole matrix element $\wp_{ab}$ of the atom on the transition $|a\rangle \rightarrow |b\rangle$, field per photon ε_c within the cavity volume, and the cavity mode function $u(\mathbf{r}_i)$ at the position $\mathbf{r}_i$ of the atom. Since atoms 1 and 2 may be at nonequivalent positions, g_1 and g_2 are in general different. We also assume that the detunings Δ_1 and Δ_2 can be individually controlled by, e.g., spatially inhomogeneous electric (dc Stark) or magnetic (Zeeman) fields or by a focused

2469-9926/2018/97(3)/032341(6)

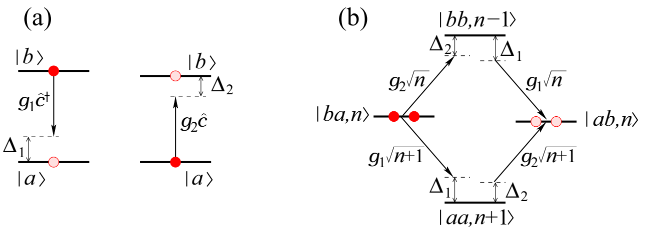

FIG. 1. Schematics of the system. (a) Two atoms with levels $|a\rangle$, $|b\rangle$ are coupled to the cavity field $\hat{c}$ with coupling strengths g_1 and g_2 and detunings Δ_1 and Δ_2, respectively. (b) Transitions between states $|ba,n\rangle$ and $|ab,n\rangle$ containing n cavity photons can occur via two paths involving intermediate, nonresonant states $|bb,n-1\rangle$ and $|aa,n+1\rangle$.

nonresonant laser inducing an ac Stark shift of one of the Rydberg states [29].

Several relaxation processes are affecting the system. We assume that both Rydberg states $|a\rangle$ and $|b\rangle$ decay with approximately the same rate Γ to some lower state(s) $|s\rangle$ which are decoupled from the cavity field. These decay processes are described by the Liouvillians [27,28]

$$\mathcal{L}_{a_i}\hat{\rho} = \tfrac{1}{2}\Gamma\big(2\hat{\sigma}_{sa}^{(i)}\hat{\rho}\hat{\sigma}_{as}^{(i)} - \hat{\sigma}_{aa}^{(i)}\hat{\rho} - \hat{\rho}\hat{\sigma}_{aa}^{(i)}\big) + \tfrac{1}{2}\Gamma\big(2\hat{\sigma}_{sb}^{(i)}\hat{\rho}\hat{\sigma}_{bs}^{(i)} - \hat{\sigma}_{bb}^{(i)}\hat{\rho} - \hat{\rho}\hat{\sigma}_{bb}^{(i)}\big) \tag{2}$$

acting on the density operator $\hat{\rho}$ of the total system. The relaxation of the cavity field toward thermal equilibrium with rate κ is described by

$$\mathcal{L}_c\hat{\rho} = \tfrac{1}{2}\kappa(1+\bar{n}_{\text{th}})(2\hat{c}\hat{\rho}\hat{c}^\dagger - \hat{c}^\dagger\hat{c}\hat{\rho} - \hat{\rho}\hat{c}^\dagger\hat{c}) + \tfrac{1}{2}\kappa\bar{n}_{\text{th}}(2\hat{c}^\dagger\hat{\rho}\hat{c} - \hat{c}\hat{c}^\dagger\hat{\rho} - \hat{\rho}\hat{c}\hat{c}^\dagger), \tag{3}$$

where $\bar{n}_{\text{th}} = (e^{\hbar\omega/k_B T} - 1)^{-1}$ is the mean number of thermal photons in the cavity mode at temperature T [27,28].

The density operator of the total system obeys the master equation

$$\partial_t\hat{\rho} = -\frac{i}{\hbar}[\mathcal{H},\hat{\rho}] + \mathcal{L}_{a_1}\hat{\rho} + \mathcal{L}_{a_2}\hat{\rho} + \mathcal{L}_c\hat{\rho}. \tag{4}$$

We solve numerically the equations for the density matrix of the system whose Hilbert space is a tensor product space of two three-state atoms, $\{|a\rangle, |b\rangle, |s\rangle\}_{i=1,2}$, and the cavity field with the photon number states $\{|n\rangle\}$ truncated at sufficiently large $n \leqslant 100$.

B. Adiabatic elimination of the cavity mode

We are interested in the state or excitation transfer between atoms 1 and 2 using the cavity mode as a quantum bus. Consider the states $|ba,n\rangle$ and $|ab,n\rangle$ with either one or the other atom excited, while the cavity mode contains n photons, see Fig. 1(b). There are two transition paths between these states via the intermediate states $|aa,n+1\rangle$ and $|bb,n-1\rangle$ involving a photon addition to or subtraction from the cavity mode. In order to minimize the effects of relaxation and thermalization of the cavity mode during the transfer, the atoms should exchange virtual cavity photons. We therefore choose the atomic detunings to be similar and large enough, $\Delta_{1,2} \gg |\Delta_1 - \Delta_2|, g_{1,2}\sqrt{n_{\max}}$, where $n_{\max}$ is the maximal number of photons that can be in the cavity with appreciable probability; typically, $n_{\max}$ can be taken as $10 \times \bar{n}_{\text{th}}$, and we recall that at thermal equilibrium the probability distribution of the cavity photon number is

$$P_n = \frac{\bar{n}_{\text{th}}^n}{(1+\bar{n}_{\text{th}})^{n+1}}. \tag{5}$$

Using the perturbation theory, we adiabatically eliminate the nonresonant intermediate states $|aa,n+1\rangle$ and $|bb,n-1\rangle$. We then obtain that the energies of states $|ba,n\rangle$ and $|ab,n\rangle$ are Stark shifted by the cavity field as

$$E_{ba,n} \simeq \tfrac{1}{2}\delta + \frac{g_1^2(n+1)}{\Delta_1 + S(n+1)} - \frac{g_2^2 n}{\Delta_2 + Sn}, \tag{6a}$$

$$E_{ab,n} \simeq -\tfrac{1}{2}\delta + \frac{g_2^2(n+1)}{\Delta_2 + S(n+1)} - \frac{g_1^2 n}{\Delta_1 + Sn}, \tag{6b}$$

where $\delta \equiv \Delta_1 - \Delta_2$ and $S \equiv \frac{g_1^2}{\Delta_1} + \frac{g_2^2}{\Delta_2}$. Simultaneously, the transition amplitude between the states $|ba,n\rangle$ and $|ab,n\rangle$ is given by

$$G(n) \simeq \frac{g_1 g_2(n+1)}{2}\left[\frac{1}{\Delta_1 + S(n+1)} + \frac{1}{\Delta_2 + S(n+1)}\right] - \frac{g_1 g_2 n}{2}\left[\frac{1}{\Delta_1 + Sn} + \frac{1}{\Delta_2 + Sn}\right], \tag{7}$$

where the first and the second terms correspond to the amplitudes of transitions via the states $|aa,n+1\rangle$ and $|bb,n-1\rangle$, respectively.

C. Transfer probability

States $|ba,n\rangle$ and $|ab,n\rangle$ have the energy difference $\delta E(n) \equiv E_{ba,n} - E_{ab,n}$ and are coupled with rate $G(n)$. Since we assumed $\Delta_1 \approx \Delta_2 = \Delta \gg \delta$, we can cast the energy difference and transition rate as

$$\delta E(n) \simeq \delta + \frac{g_1^2 - g_2^2}{\Delta}(2n+1), \tag{8}$$

$$G(n) \simeq \frac{g_1 g_2}{\Delta}\left(1 - \frac{\delta}{2\Delta} - \frac{g_1^2 + g_2^2}{\Delta^2}(2n+1)\right), \tag{9}$$

where we neglected terms of the order of $\delta\frac{g^2}{\Delta^2}$, $\frac{g^4}{\Delta^3}$ and higher. We thus see that both $\delta E(n)$ and $G(n)$ depend on the cavity photon number n. If the coupling strengths g_1 and g_2 are the same, the differential Stark shifts of levels $|ba,n\rangle$ and $|ab,n\rangle$ become n independent. Then, by choosing $\delta = 0$, we obtain that both atoms have the same transition frequency, $\delta E(n) = 0\,\forall\, n$. Simultaneously, due to interference between the two transition paths, $G(n)$ only weakly depends on the cavity photon number n, leading to resonant exchange of excitation between the atoms. In Fig. 2 upper panel, we show the oscillations between the states $|ba\rangle$ and $|ab\rangle$ of the two atoms with equal couplings $g_1 = g_2$ to the cavity, which has a large mean thermal photon number $\bar{n}_{\text{th}}$ corresponding to a broad photon number distribution P_n.

When, however, the coupling strengths g_1 and g_2 are different, the energy difference $\delta E(n)$ is photon number dependent. Then, in a thermal cavity, $\bar{n}_{\text{th}} > 0$, with a broad distribution P_n of photon numbers, $\delta E(n)$ cannot be made to vanish for all n.

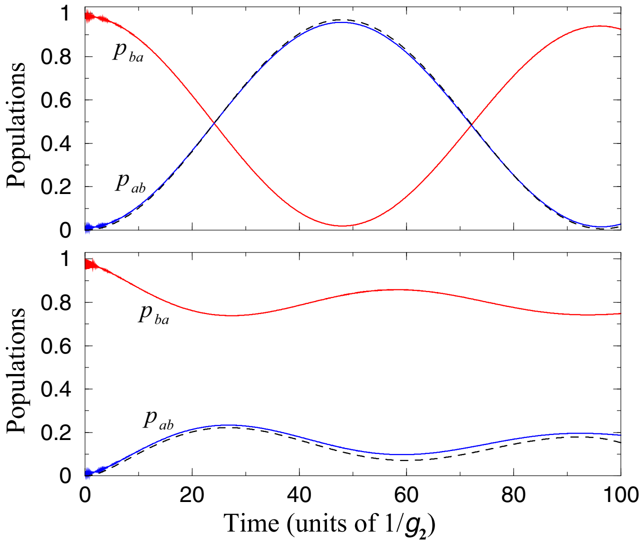

FIG. 2. Oscillations between the states $|ba\rangle$ (red solid line) and $|ab\rangle$ (blue solid line) in a cavity, as obtained from the numerical simulations of the master equation (4). The parameters are $\Delta_1 = \Delta_2 = 30g_2$, $\kappa = 10^{-3}g_2$, $\bar{n}_{\rm th} = 5$, $\Gamma = 3\times10^{-4}g_2$, while $g_1 = g_2$ (upper panel) and $g_1 = 1.4g_2$ (lower panel). The dashed black line results from the approximate expression (11).

In fact, the difference between $\delta E(n)$ for various n is of the order of the transition rate G, which suppresses the amplitude of oscillations between the states $|ba\rangle$ and $|ab\rangle$, as shown in Fig. 2, lower panel.

We can derive an approximate expression for the transfer probability between the states $|ba\rangle$ and $|ab\rangle$ as follows. Assume that we start in state $|ba,n\rangle$ at time $t=0$. Without relaxations, the probability for the system to be in state $|ab,n\rangle$ would be given by

$$p_{ab,n}(t) = \left|\frac{G(n)}{\bar{G}(n)}\right|^2 \sin^2[\bar{G}(n)t],$$

where $\bar{G}(n) = \sqrt{|G(n)|^2 + \frac{1}{4}|\delta E(n)|^2}$ is the generalized Rabi frequency for the oscillations between $|ba,n\rangle$ and $|ab,n\rangle$. Relaxations will result in exponential damping of the transfer probability. The decay of states $|a\rangle$ and $|b\rangle$ of each atom with rate Γ leads to multiplication by $e^{-\Gamma t}$. We neglect for now the cavity relaxation and will consider its effect later. Thus the transfer probability from state $|ba,n\rangle$ to state $|ab,n\rangle$ is given by

$$p_{ab,n}(t) = e^{-2\Gamma t}\left|\frac{G(n)}{\bar{G}(n)}\right|^2 \sin^2[\bar{G}(n)t]. \tag{10}$$

If initially there is an equilibrium photon number distribution P_n in the cavity, the total probability of transfer between $|ba\rangle$ and $|ab\rangle$ is given by

$$p_{ab}(t) = \sum_n P_n p_{ab,n}(t). \tag{11}$$

This expression approximates well the exact dynamics of the system for small $\kappa \ll G$, as verified in Fig. 2.

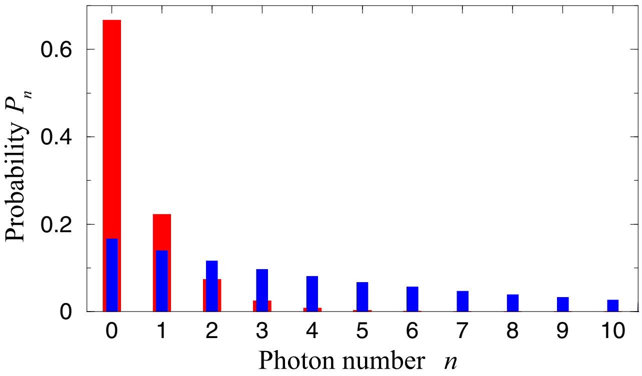

FIG. 3. Equilibrium photon number distribution P_n in the cavity with $\bar{n}_{\rm th} = 5$ (blue narrow bars) and with continuous photon extraction with rate $\gamma_{\rm c} = 9\kappa$ (red thicker bars) leading to $\bar{n}_{\rm eff} = 0.5$.

III. REDUCING THE NUMBER OF THERMAL PHOTONS

The thermal photons in the cavity thus preclude efficient state transfer between the atoms when their couplings to the cavity mode have, in general, different strength, $g_1 \neq g_2$. We now outline a method to reduce the number of photons in the cavity, which will significantly increase the transfer probability. We will use an ensemble of stationary trapped atoms extracting photons from the cavity by continuous optical pumping, attaining thereby an equilibrium with a smaller mean number of photons. We note a conceptually similar approach [30–32] to extract thermal photons from a microwave cavity by sending across it a sequence of atoms prepared in the lower Rydberg state, which is typically done in the transient regime to achieve a nearly empty cavity until it equilibrates with the thermal environment.

A. Cavity cooling by photon extraction

Our strategy to cool the cavity is to continuously extract the photons from it with a rate $\gamma_{\rm c} \gg \kappa$. This process is described by the Liouvillian

$$\mathcal{L}'_{\rm c}\hat{\rho} = \tfrac{1}{2}\gamma_{\rm c}(2\hat{c}\hat{\rho}\hat{c}^\dagger - \hat{c}^\dagger\hat{c}\hat{\rho} - \hat{\rho}\hat{c}^\dagger\hat{c}), \tag{12}$$

which should be added to $\mathcal{L}_{\rm c}\hat{\rho}$ in Eq. (3). The photon extraction thus breaks the balance between the usual photon decay to and addition from the thermal reservoir. It follows from the master equation for the cavity field that the photon number probabilities obey the equation

$$\partial_t P_n = d(n+1)P_{n+1} + anP_{n-1} - dnP_n - a(n+1)P_n,$$

where $a = \kappa\bar{n}_{\rm th}$ and $d = \kappa(\bar{n}_{\rm th}+1) + \gamma_{\rm c}$. In the steady state, $\partial_t P_n = 0$, we have the detailed balance $d(n+1)P_{n+1} = a(n+1)P_n$ [and $dnP_n = anP_{n-1}$] for any transition $n \leftrightarrow n\pm1$. This leads to $P_n = (a/d)^n P_0$, and upon normalization of the probability distribution P_n, we obtain the usual expression

$$P_n = \frac{\bar{n}_{\rm eff}^n}{(1+\bar{n}_{\rm eff})^{n+1}}, \tag{13}$$

corresponding to the equilibrium with the effective thermal photon number $\bar{n}_{\rm eff} = \frac{\bar{n}_{\rm th}}{1+\gamma_{\rm c}/\kappa}$ reduced from $\bar{n}_{\rm th}$ by a factor of $(1+\gamma_{\rm c}/\kappa)$. In Fig. 3 we show the equilibrium photon number distribution in a cavity at a temperature corresponding to large

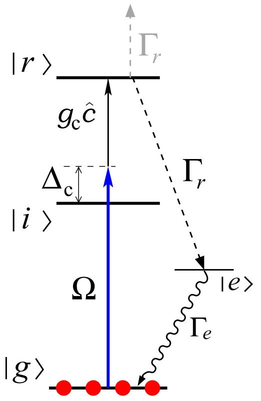

FIG. 4. Schematics of the cooling setup. Atoms in the ground state $|g\rangle$ are excited to the Rydberg state $|r\rangle$ by a two-photon transition via intermediate nonresonant state $|i\rangle$. The resonant two-photon transition involves a photon absorption from the laser field acting on the transition $|g\rangle \to |i\rangle$ with Rabi frequency Ω and detuning $\Delta_c \gg \Omega$, and a photon absorption from the cavity field coupled with strength $g_c \ll \Delta_c$ to the Rydberg transition $|i\rangle \to |r\rangle$ detuned by $-\Delta_c$. State $|r\rangle$ decays with rate Γ_r, either by ionization or by an induced cascade to state $|g\rangle$ via intermediate state $|e\rangle$, having large decay rate Γ_s.

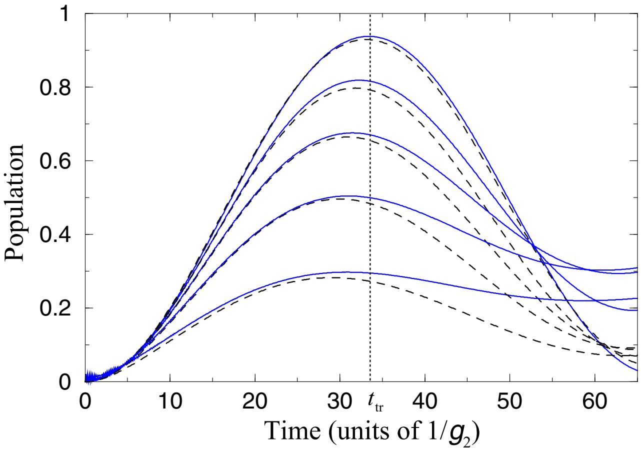

FIG. 5. Time dependence of population p_{ab} of state $|ab\rangle$ in the presence of continuous photon extraction with different rates γ_c, as obtained from exact numerical simulations of Eq. (4) (blue solid lines) and from the approximate Eq. (11) (black dashed lines), for the initial state $|ba\rangle$. Dotted vertical line indicates time $t_{tr} = \frac{\pi}{2G(0)}$ when the population of $|ab,0\rangle$ is peaked. The parameters are $g_1{=}1.4g_2$, $\Delta{=}30g_2$, $\delta = \frac{g_2^2-g_1^2}{\Delta}$, $\Gamma = 3 \times 10^{-4} g_2$, $\kappa = 10^{-2} g_2$, $\bar{n}_{th} = 5$, while $\gamma_c = (0,1.5,4,9,49)\kappa$, corresponding to the mean photon numbers $\bar{n}_{eff} = (5,2,1,0.5,0.1)$ for the graphs with progressively larger amplitudes.

$\bar{n}_{th}$. Upon continuous photon extraction with rate $\gamma_c \gg \kappa$, we obtain a thermal distribution, with a much smaller effective photon number $\bar{n}_{eff}$, which is highly peaked around $n = 0$.

B. Photon extraction by optical pumping

To extract the photons from the thermal cavity, we envision a system depicted in Fig. 4. An ensemble of N_c "cooling" atoms in the ground state $|g\rangle$ are trapped near the cavity antinode. A laser field acts on the transition from state $|g\rangle$ to a Rydberg state $|i\rangle$ with the Rabi frequency Ω and large detuning $\Delta_c \gg \Omega$. Each atom is coupled to the cavity field $\hat{c}$ on the Rydberg transition $|i\rangle \to |r\rangle$ with strength $g_c \ll \Delta_c$. Upon adiabatic elimination of the nonresonant intermediate state $|i\rangle$, we obtain an effective Rabi frequency $\Omega_n^{(2)} = \Omega g_c \sqrt{n}/\Delta_c$ for the two-photon transition $|g,n\rangle \to |r,n-1\rangle$, which involves absorption of a laser photon and a cavity photon.

We can write the equations for the amplitudes $A_{g,n}$ and $A_{r,n-1}$ of states $|g,n\rangle$ and $|r,n-1\rangle$ as

$$\partial_t A_{g,n} = -i\Omega_n^{(2)} A_{r,n-1}, \tag{14a}$$

$$\partial_t A_{r,n-1} = -\tfrac{1}{2}\Gamma_r A_{r,n-1} - i\Omega_n^{(2)} A_{g,n}, \tag{14b}$$

where Γ_r is the population decay rate of the Rydberg state $|r\rangle$ and we assume the two-photon resonance. Assuming $\Gamma_r \gg \Omega_n^{(2)}$ (see below), we can set $\partial_t A_{r,n-1} = 0$ and obtain the incoherent transition rate $\frac{1}{2}R_n = \frac{|\Omega_n^{(2)}|^2}{\Gamma_r/2}$ from $|g,n\rangle$ to $|r,n-1\rangle$. With N_c cooling atoms, we can then identify the photon extraction rate via $\gamma_c n = N_c R_n$, leading to

$$\gamma_c = N_c \frac{4\Omega^2 g_c^2}{\Delta_c^2 \Gamma_r}. \tag{15}$$

Note that contributions of individual atoms add incoherently to the total extraction rate γ_c, and the possible variation of the coupling strength g_c for different atoms can be absorbed into redefinition of the atom number N_c. In the above analysis, we have also neglected the (Rydberg blockade) interactions between the atoms in state $|r\rangle$. This approximation is justified for a moderate number of photons n and large enough $\Gamma_r \gg \Omega_n^{(2)}$, such that the probability of having simultaneously two or more atoms in state $|r\rangle$ is small.

Typically, Rydberg states have slow population decay rates. A larger decay rate Γ_r can be achieved by laser-induced ionization of state $|r\rangle$, which, however, will result in continuous depletion of the number N_c of cooling atoms. A better alternative is to use an auxiliary laser of Rabi frequency Ω_r to resonantly couple the Rydberg state $|r\rangle$ to a lower excited state $|e\rangle$ having large decay rate $\Gamma_e \gg \Omega_r$ back to the ground state $|g\rangle$, as shown in Fig. 4. This will induce a cascade from $|r\rangle$ to $|g\rangle$ with sufficiently rapid rate $\Gamma_r \simeq \frac{4\Omega_r^2}{\Gamma_e}$. Thus, each cooling cycle $|g,n\rangle \to |r,n-1\rangle \to |g,n-1\rangle$ will extract with rate γ_c a cavity photon, while the number of cooling atoms will be preserved. For $\gamma_c \gg \kappa\bar{n}_{th}$, we can then approach a cavity vacuum by optically pumping out thermal photons.

IV. STATE TRANSFER VIA COOLED CAVITY

In Fig. 5 we demonstrate significant enhancement of the amplitude of oscillations between the initial $|ba\rangle$ and the target $|ab\rangle$ states in the presence of rapid extraction of thermal photons from the cavity. Since the probability distribution of the cavity photons is now highly peaked at around $n = 0$, we set the frequency mismatch $\delta = \frac{g_2^2 - g_1^2}{\Delta}$ to satisfy the resonant condition $\delta E(0) = 0$ in Eq. (8).

A. Optimizing the transfer fidelity

From Eq. (9) we have for the transition rate $G(0) \simeq \frac{g_1 g_2}{\Delta}(1 - \frac{\delta}{2\Delta} - \frac{g_1^2+g_2^2}{\Delta^2})$. Our aim is to transfer the population of state $|ba\rangle$ to state $|ab\rangle$. Using Eq. (11), we can estimate the lower bound for the transfer probability as being determined mainly by the $n = 0$ term,

$$p_{ab}(t) > P_0 p_{ab,0}(t) = \frac{1}{1+\bar{n}_{\text{eff}}} e^{-2\Gamma t} \times \tfrac{1}{2}\{1 - \cos[2G(0)t]e^{-\kappa_{\text{eff}} t}\}, \quad (16)$$

where we included the effective damping rate $\kappa_{\text{eff}} = (\kappa + \gamma_{\text{c}})\frac{g_1^2+g_2^2}{2\Delta^2}$ of the oscillation amplitude, which can be intuitively understood as follows: During the transfer, states $|ba,0\rangle$ and $|ab,0\rangle$ have small admixture, $\sim\frac{g_{1,2}}{\Delta}$, of state $|aa,1\rangle$ containing the additional exchange photon which is damped with rate $(\kappa + \gamma_{\text{c}})$. The transfer probability is peaked at time $t_{\text{tr}} = \frac{\pi}{2G(0)}$ when $\cos[2G(0)t_{\text{tr}}] = -1$. Assuming $\bar{n}_{\text{eff}} \ll 1$ and $(\kappa_{\text{eff}},\Gamma)t_{\text{tr}} \ll 1$, the transfer fidelity is then

$$F \equiv P_0 p_{ab,0}(t_{\text{tr}}) \gtrsim \left[1 - \frac{\kappa \bar{n}_{\text{th}}}{\kappa + \gamma_{\text{c}}}\right]\left[1 - \pi\frac{\Gamma\Delta}{g_1 g_2}\right]\left[1 - \pi\frac{\kappa + \gamma_{\text{c}}}{4\Delta}\frac{g^2}{g_1 g_2}\right],$$

where $g^2 = \frac{1}{2}(g_1^2 + g_2^2)$. Although the right-hand side of this expression underestimates the maximal fidelity, we can still use it to optimize the parameters of the system. Thus, the transfer fidelity is reduced by three factors, and we therefore require that each of them be small:

(i) $\gamma_{\text{c}} + \kappa \gg \kappa \bar{n}_{\text{th}}$, i.e., the cooling rate γ_{c} should be sufficiently large to have the mean photon number small, $\bar{n}_{\text{eff}} \ll 1$;

(ii) $\frac{g_1 g_2}{\Delta} \gg \Gamma$, i.e., the transition rate $G(0)$ should be large enough to have small probability of the atomic decay during the transfer;

(iii) $\Delta \gg \gamma_{\text{c}} + \kappa$, i.e., the cavity field should be strongly detuned to have a small photon population and therefore decay during the transfer.

With $\gamma_{\text{c}} \gg \kappa$, the total reduction of the fidelity, or infidelity, can be estimated as

$$1 - F \simeq \frac{\kappa \bar{n}_{\text{th}}}{\gamma_{\text{c}}} + \pi\frac{\Gamma\Delta}{g_1 g_2} + \pi\frac{\gamma_{\text{c}}}{4\Delta}\frac{g^2}{g_1 g_2}. \quad (17)$$

We can minimize this expression with respect to Δ, with the other parameters fixed, obtaining

$$1 - F \simeq \frac{\kappa \bar{n}_{\text{th}}}{\gamma_{\text{c}}} + \frac{\pi g}{g_1 g_2}\sqrt{\Gamma \gamma_{\text{c}}} \quad (18)$$

for $\Delta = g\sqrt{\frac{\gamma_{\text{c}}}{4\Gamma}}$. Next, we minimize the resulting infidelity with respect to γ_{c}, finally obtaining

$$\min(1 - F) \leqslant 3(\kappa \bar{n}_{\text{th}})^{1/3}\left(\frac{\pi g\sqrt{\Gamma}}{2 g_1 g_2}\right)^{2/3} \quad (19)$$

for $\gamma_{\text{c}} = (\frac{2\kappa \bar{n}_{\text{th}} g_1 g_2}{\pi g\sqrt{\Gamma}})^{2/3}$.

B. Experimental considerations

We assume the following realistic parameters of the system: The cavity mode resonant frequency is $\omega = 2\pi \times 5$ GHz, and its quality factor is $Q = 10^5$, leading to the decay rate $\kappa \simeq 300$ kHz. The Rydberg atom-cavity coupling rates are $g_1 = 2\pi \times 5$ MHz and similar for g_2. The decay rates of the atoms are $\Gamma = 10$ kHz. With $\bar{n}_{\text{th}} \approx 10$ at cryogenic environment, we need to choose the cooling rate $\gamma_{\text{c}} \gtrsim 15$ MHz, which can be achieved with $N_{\text{c}} \approx 1000$ cooling atoms, with $\Omega \simeq g_{\text{c}} = 2\pi \times 0.1$ MHz, $\Delta_{\text{c}} = 10\Omega$, and $\Gamma_r = 1$ MHz. We then choose the detunings $\Delta_1 \simeq 30 g_1$ and $\Delta_2 = \Delta_1 + \frac{g_1^2 - g_2^2}{\Delta}$ for the resonant transfer of the excitation between the atoms. The resulting fidelity is $F \gtrsim 0.95$, which we verified numerically. To turn off the transfer, one of the atoms can be strongly detuned by $|\Delta_1 - \Delta_2| \gg G(0) \simeq \frac{g_1 g_2}{\Delta}$, which can be achieved by, e.g., Stark shifting the resonance with a focused laser beam [29].

V. CONCLUSIONS

We have elaborated the conditions for coherent state transfer between two two-level systems through a thermal microwave cavity. We have demonstrated that by actively cooling a cavity mode by continuously removing photons with a laser-driven ensemble of atoms, a high-fidelity SWAP operation between pairs of spatially separated Rydberg atom qubits is possible in state-of-the-art experimental systems [12,15,16,20]. The $\sqrt{\text{SWAP}}$ is a universal entangling quantum gate [27] which can also be realized by the present scheme.

Trapped ground-state atoms have good coherence properties and can serve as reliable qubits. The atoms can be excited on demand by focused lasers to the Rydberg states for realizing short-distance quantum communication and quantum logic gates. Our results will thus pave the way for the realization of scalable quantum information processing with cold atoms trapped on the integrated superconducting atom chips.

ACKNOWLEDGMENT

We acknowledge the financial support of the DFG Schwerpunktsprogramm Giant Interactions in Rydberg Systems (GiRyd SPP 1929).

---

[1] M. D. Lukin, M. Fleischhauer, R. Cote, L. M. Duan, D. Jaksch, J. I. Cirac, and P. Zoller, Dipole Blockade and Quantum Information Processing in Mesoscopic Atomic Ensembles, Phys. Rev. Lett. **87**, 037901 (2001).

[2] M. Saffman, T. G. Walker, and K. Mølmer, Quantum information with Rydberg atoms, Rev. Mod. Phys. **82**, 2313 (2010).

[3] M. Saffman, Quantum computing with atomic qubits and Rydberg interactions: Progress and challenges, J. Phys. B **49**, 202001 (2016).

[4] D. Petrosyan, F. Motzoi, M. Saffman, and K. Mølmer, High-fidelity Rydberg quantum gate via a two-atom dark state, Phys. Rev. A **96**, 042306 (2017).

[5] P. Schauß, J. Zeiher, T. Fukuhara, S. Hild, M. Cheneau, T. Macrì, T. Pohl, I. Bloch, and C. Gross, Crystallization in Ising quantum magnets, Science **347**, 1455 (2015).

[6] H. Labuhn, D. Barredo, S. Ravets, S. de Léséleuc, T. Macrì, T. Lahaye, and A. Browaeys, Tunable two-dimensional arrays of single Rydberg atoms for realizing quantum Ising models, Nature (London) **534**, 667 (2016).

[7] H. Bernien, S. Schwartz, A. Keesling, H. Levine, A. Omran, H. Pichler, S. Choi, A. S. Zibrov, M. Endres, M. Greiner, V. Vuletic, and M. D. Lukin, Probing many-body dynamics on a 51-atom quantum simulator, Nature (London) **551**, 579 (2017).

[8] V. Lienhard, S. de Léséleuc, D. Barredo, T. Lahaye, A. Browaeys, M. Schuler, L.-P. Henry, and A. M. Läuchli, Observing the space- and time-dependent growth of correlations in dynamically tuned synthetic Ising antiferromagnets, arXiv:1711.01185.

[9] J. Fortágh and C. Zimmermann, Magnetic microtraps for ultracold atoms, Rev. Mod. Phys. **79**, 235 (2007).

[10] S. Bernon, H. Hattermann, D. Bothner, M. Knufinke, P. Weiss, F. Jessen, D. Cano, M. Kemmler, R. Kleiner, D. Koelle, and J. Fortágh, Manipulation and coherence of ultra-cold atoms on a superconducting atom chip, Nat. Commun. **4**, 2380 (2013).

[11] J. Verdú, H. Zoubi, Ch. Koller, J. Majer, H. Ritsch, and J. Schmiedmayer, Strong Magnetic Coupling of An Ultracold Gas to a Superconducting Waveguide Cavity, Phys. Rev. Lett. **103**, 043603 (2009).

[12] H. Hattermann, D. Bothner, L. Y. Ley, B. Ferdinand, D. Wiedmaier, L. Sárkány, R. Kleiner, D. Koelle, and J. Fortágh, Coupling ultracold atoms to a superconducting coplanar waveguide resonator, Nat. Commun. **8**, 2254 (2017).

[13] I. I. Beterov, I. I. Ryabtsev, D. B. Tretyakov, and V. M. Entin, Quasiclassical calculations of blackbody-radiation-induced depopulation rates and effective lifetimes of Rydberg ns, np, and nd alkali-metal atoms with $n \leqslant 80$, Phys. Rev. A **79**, 052504 (2009).

[14] M. Mack, J. Grimmel, F. Karlewski, L. Sárkány, H. Hattermann, and J. Fortágh, All-optical measurement of Rydberg-state lifetimes, Phys. Rev. A **92**, 012517 (2015).

[15] C. Hermann-Avigliano, R. C. Teixeira, T. L. Nguyen, T. Cantat-Moltrecht, G. Nogues, I. Dotsenko, S. Gleyzes, J. M. Raimond, S. Haroche, and M. Brune, Long coherence times for Rydberg qubits on a superconducting atom chip, Phys. Rev. A **90**, 040502(R) (2014).

[16] R. C. Teixeira, C. Hermann-Avigliano, T. L. Nguyen, T. Cantat-Moltrecht, J. M. Raimond, S. Haroche, S. Gleyzes, and M. Brune, Microwaves Probe Dipole Blockade and Van der Waals Forces in a Cold Rydberg Gas, Phys. Rev. Lett. **115**, 013001 (2015).

[17] A. Wallraff, D. I. Schuster, A. Blais, L. Frunzio, R.-S. Huang, J. Majer, S. Kumar, S. M. Girvin, and R. J. Schoelkopf, Strong coupling of a single photon to a superconducting qubit using circuit quantum electrodynamics, Nature (London) **431**, 162 (2004).

[18] I. Chiorescu, P. Bertet, K. Semba, Y. Nakamura, C. J. P. M. Harmans, and J. E. Mooij, Coherent dynamics of a flux qubit coupled to a harmonic oscillator, Nature (London) **431**, 159 (2004).

[19] J. Q. You and F. Nori, Atomic physics and quantum optics using superconducting circuits, Nature (London) **474**, 589 (2011).

[20] S. D. Hogan, J. A. Agner, F. Merkt, T. Thiele, S. Filipp, and A. Wallraff, Driving Rydberg-Rydberg Transitions from a Coplanar Microwave Waveguide, Phys. Rev. Lett. **108**, 063004 (2012).

[21] D. Petrosyan, G. Bensky, G. Kurizki, I. Mazets, J. Majer, and J. Schmiedmayer, Reversible state transfer between superconducting qubits and atomic ensembles, Phys. Rev. A **79**, 040304 (2009).

[22] D. Petrosyan and M. Fleischhauer, Quantum Information Processing with Single Photons and Atomic Ensembles in Microwave Coplanar Waveguide Resonators, Phys. Rev. Lett. **100**, 170501 (2008).

[23] J. D. Pritchard, J. A. Isaacs, M. A. Beck, R. McDermott, and M. Saffman, Hybrid atom-photon quantum gate in a superconducting microwave resonator, Phys. Rev. A **89**, 010301 (2014).

[24] L. Sárkány, J. Fortágh, and D. Petrosyan, Long-range quantum gate via Rydberg states of atoms in a thermal microwave cavity, Phys. Rev. A **92**, 030303 (2015).

[25] Z.-L. Xiang, M. Zhang, L. Jiang, and P. Rabl, Intracity Quantum Communication via Thermal Microwave Networks, Phys. Rev. X **7**, 011035 (2017).

[26] B. Vermersch, P.-O. Guimond, H. Pichler, and P. Zoller, Quantum State Transfer Via Noisy Photonic and Phononic Waveguides, Phys. Rev. Lett. **118**, 133601 (2017).

[27] P. Lambropoulos and D. Petrosyan, *Fundamentals of Quantum Optics and Quantum Information* (Springer, New York, 2007).

[28] S. Haroche and J.-M. Raimond, *Exploring the Quantum: Atoms, Cavities, and Photons* (Oxford University Press, Oxford, UK, 2006).

[29] S. de Léséleuc, D. Barredo, V. Lienhard, A. Browaeys, and T. Lahaye, Optical Control of the Resonant Dipole-Dipole Interaction Between Rydberg Atoms, Phys. Rev. Lett. **119**, 053202 (2017).

[30] J. M. Raimond, M. Brune, and S. Haroche, Manipulating quantum entanglement with atoms and photons in a cavity, Rev. Mod. Phys. **73**, 565 (2001).

[31] G. Nogues, A. Rauschenbeutel, S. Osnaghi, M. Brune, J. M. Raimond, and S. Haroche, Manipulating quantum entanglement with atoms and photons in a cavity, Nature (London) **400**, 239 (1999).

[32] J. Bernu, S. Deléglise, C. Sayrin, S. Kuhr, I. Dotsenko, M. Brune, J. M. Raimond, and S. Haroche, Freezing Coherent Field Growth in a Cavity by the Quantum Zeno Effect, Phys. Rev. Lett. **101**, 180402 (2008).

RAPID COMMUNICATIONS

PHYSICAL REVIEW A **92**, 030303(R) (2015)

Long-range quantum gate via Rydberg states of atoms in a thermal microwave cavity

Lőrinc Sárkány,[1] József Fortágh,[1] and David Petrosyan[2,3]

[1]*CQ Center for Collective Quantum Phenomena and their Applications, Physikalisches Institut,*
Eberhard Karls Universität Tübingen, Auf der Morgenstelle 14, D-72076 Tübingen, Germany
[2]*Institute of Electronic Structure and Laser, FORTH, GR-71110 Heraklion, Crete, Greece*
[3]*Aarhus Institute of Advanced Studies, Aarhus University, DK-8000 Aarhus C, Denmark*

(Received 22 April 2015; revised manuscript received 14 August 2015; published 21 September 2015)

We propose an implementation of a universal quantum gate between pairs of spatially separated atoms in a microwave cavity at finite temperature. The gate results from reversible laser excitation of Rydberg states of atoms interacting with each other via exchange of virtual photons through a common cavity mode. Quantum interference of different transition paths between the two-atom ground and double-excited Rydberg states makes both the transition amplitude and resonance largely insensitive to the excitations in the microwave cavity quantum bus which can therefore be in any superposition or mixture of photon number states. Our scheme for attaining ultra-long-range interactions and entanglement also applies to mesoscopic atomic ensembles in the Rydberg blockade regime and is scalable to many ensembles trapped within a centimeter-sized microwave resonator.

DOI: 10.1103/PhysRevA.92.030303 PACS number(s): 03.67.Lx, 32.80.Ee, 37.30.+i

Quantum interfaces between solid-state devices and cold atoms are the backbone of a novel class of hybrid quantum systems [1–4] linking fast quantum gates [5,6] with long-lived quantum memories [7,8] and optical quantum communication channels [9–11]. Superconducting coplanar waveguide resonators operating in the microwave regime have been demonstrated to provide strong coupling between solid-state superconducting qubits [12–15] and to mediate quantum state transfer between superconducting qubits and spin ensembles [16–18]. Cold atoms trapped near the surface of an atom chip [19–23] possess good coherence properties and strong optical (Raman) transitions. Therefore, ensembles of trapped atoms or molecules interacting with on-chip microwave resonators were proposed as convenient systems [24–28] for realizing quantum gates and memories as well as optical interfaces. A promising approach to achieve strong coupling of atoms to microwave resonators [27–31] is to employ the atomic Rydberg states having huge electric dipole moments [32].

A common feature of all these schemes is that they require an initially empty microwave cavity which should be kept at very low temperatures of $T \lesssim 100$ mK. This is routinely achieved with solid-state superconducting circuits in dilution refrigerators but is challenging to realize and maintain in combination with ultracold atoms [33]. In turn, atoms are routinely trapped on atom chips at $T \simeq 4$ K [22,31], but then the integrated superconducting cavities have lower quality (Q) factor, and the presence of thermal cavity photons and their fluctuations would preclude high-fidelity quantum operations.

Here we present a scalable scheme for cavity-mediated coherent interactions between Rydberg states of atoms in a thermal microwave cavity. We show that a universal quantum gate between pairs of laser-driven atoms, or atomic ensembles in the Rydberg blockade regime [34,35], can be achieved with current cold-atom experimental technology [21,30,31,36,37].

Our work has been inspired by the seminal proposal of Sørensen and Mølmer [38] to realize quantum computation and entanglement with ions sharing a common vibrational mode subject to thermal fluctuations. Different from the ion trap, in our scheme the cavity mode exchanging photons with the thermal environment simultaneously interacts with atoms on the transitions between neighboring Rydberg states, playing the role of the so-called quantum bus for spatially separated qubits [Fig. 1(a)]. Now the photon-number uncertainty affects not only the amplitude of the laser-mediated transition between the atomic ground and Rydberg states, but also induces fluctuating ac-Stark shifts of atomic levels. By a suitable choice of the system parameters, we ensure that both the multiphoton transition amplitude and its resonant frequency are insensitive to the cavity photon number, making the gate operations immune to the exchange of photons with the thermal environment, which relaxes the need for a low-temperature high-Q cavity.

We first describe the scheme for individual atoms and later adapt it also to atomic ensembles forming Rydberg "superatoms" [34,35,39]. Consider a pair of identical atoms 1 and 2 with the ground state $|g\rangle$ and the highly excited Rydberg state $|r\rangle$ [Fig. 1(b)]. The atoms interact nonresonantly with a common mode of the microwave cavity via the dipole-allowed transitions to the adjacent Rydberg states $|a\rangle$ and $|b\rangle$; the corresponding coupling strengths are denoted by $g_{a,b}$. Two excitation lasers of optical frequencies $\omega_{1,2}$ act on the atomic transitions $|g\rangle_1 \to |a\rangle_1$ and $|g\rangle_2 \to |b\rangle_2$ with the Rabi frequencies $\Omega_{1,2}$. For simplicity we assume for now that each laser interacts only with the corresponding atom (see below for the symmetric coupling of both atoms). The total Hamiltonian of the system in the rotating wave approximation takes the form $H = H_c + \sum_{i=1,2}[H_a^{(i)} + V_{ac}^{(i)} + V_{al}^{(i)}]$. Here $H_c = \hbar\omega_c(\hat{c}^\dagger\hat{c} + \frac{1}{2})$ is the Hamiltonian for cavity field with the photon creation $\hat{c}^\dagger$ and annihilation $\hat{c}$ operators in the mode of frequency ω_c, $H_a^{(i)} = \hbar\sum_\mu \omega_\mu |\mu\rangle_i\langle\mu|$ is the Hamiltonian of the unperturbed atom i with the Bohr (excitation) frequencies ω_μ of the corresponding energy levels $|\mu\rangle$ ($\mu = g,r,a,b$), $V_{ac}^{(i)} = \hbar(g_a\hat{c}\,|a\rangle_i\langle r| + g_b\hat{c}^\dagger\,|b\rangle_i\langle r| + \text{H.c.})$ describes the atom-cavity interactions, and $V_{al}^{(1)} = \hbar\Omega_1 e^{-i\omega_1 t}\,|a\rangle_1\langle g| + \text{H.c.}$ and $V_{al}^{(2)} = \hbar\Omega_2 e^{-i\omega_2 t}\,|b\rangle_2\langle g| + \text{H.c.}$ describe the laser driving of atoms 1 and 2, respectively.

We assume that the two atoms initially in the ground state $|g\rangle$ are in spatially separated traps at equivalent positions,

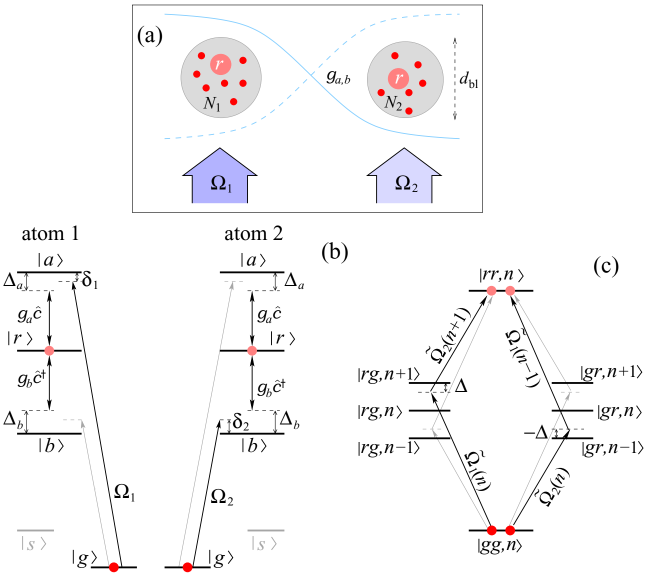

FIG. 1. (Color online) Schematics of the system. (a) Spatially separated atoms, or superatoms composed of $N_{1,2}$ atoms within the Rydberg blockade distance $d_{\rm bl}$, interact with a pair of optical lasers and a common mode of a microwave cavity. (b) Level scheme of two atoms interacting with the cavity field on the Rydberg transitions $|r\rangle \leftrightarrow |a\rangle, |b\rangle$ with strengths $g_{a,b}$ and driven by the laser fields with Rabi frequencies $\Omega_{1,2}$ on the transitions from the ground state $|g\rangle$ to states $|a\rangle, |b\rangle$. (c) Under appropriate conditions (see text for details), there are two interfering excitation pathways from the two-atom ground state $|gg,n\rangle$ to the double-excited Rydberg state $|rr,n\rangle$, which cancel the dependence of the total transition amplitude $\bar{\Omega}$ on the cavity photon number n.

close to field antinodes of the microwave cavity containing an arbitrary number of photons n. Our aim is to achieve coherent oscillations between the collective states $|gg,n\rangle$ and $|rr,n\rangle$ with maximal amplitude and oscillation frequency which do not depend on n. Denoting the detunings of the laser fields by $\delta_1 = \omega_{ag} - \omega_1$ and $\delta_2 = \omega_{bg} - \omega_2$ and taking Rabi frequencies $\Omega_{1,2} \ll |\delta_{1,2}|$, we adiabatically eliminate the intermediate atomic states $|a\rangle_1$ and $|b\rangle_2$, obtaining two-photon Rabi frequencies $\tilde{\Omega}_1(n) = \frac{\Omega_1 g_a\sqrt{n+1}}{\delta_1}$ and $\tilde{\Omega}_2(n) = \frac{\Omega_2 g_b\sqrt{n}}{\delta_2}$ on the transitions $|gg,n\rangle \to |rg,n+1\rangle$ and $|gg,n\rangle \to |gr,n-1\rangle$ accompanied by addition and subtraction of a cavity photon, respectively [Fig. 1(c)].

We next take large and unequal detunings $\Delta_a = \omega_{ar} - \omega_c$ and $\Delta_b = \omega_{rb} - \omega_c$ of the cavity field from the transition resonances between the atomic Rydberg states, $|\Delta_{a,b}| \gg g_{a,b}$. To avoid cavity-mediated Förster resonances $|rr,n\rangle \to |ab,n\rangle, |ba,n\rangle$ [27], we require that $|\Delta_a - \Delta_b| \gg g_a g_b |\frac{n+1}{\Delta_b} - \frac{n}{\Delta_a}|$ for all $n \lesssim n_{\max}$, where $n_{\max}$ is the maximal possible cavity photon number [typically $n_{\max} \approx 2\bar{n}_{\rm th}$ for a thermal field with the mean number of photons $\bar{n}_{\rm th} = (e^{\hbar\omega_c/k_{\rm B}T} - 1)^{-1}$]. If we now choose the two-photon detunings $\Delta_{1,2} \approx \delta_{1,2} \mp \Delta_{a,b}$ of states $|rg,n+1\rangle$ and $|gr,n-1\rangle$ to have equal magnitude but opposite sign, $\Delta_1 = -\Delta_2 = \Delta \gg \tilde{\Omega}_{1,2}$, we can also eliminate these intermediate states and obtain resonant multiphoton transitions between states $|gg,n\rangle$ and $|rr,n\rangle$ involving two laser photons and an exchange of a (virtual) cavity photon between the two atoms. With two equivalent excitation paths from $|gg,n\rangle$ to $|rr,n\rangle$ [Fig. 1(c)], the resulting transition amplitude (effective Rabi frequency) is

$$\bar{\Omega} = \frac{\tilde{\Omega}_1(n)\tilde{\Omega}_2(n+1)}{\Delta_1(n)} + \frac{\tilde{\Omega}_2(n)\tilde{\Omega}_1(n-1)}{\Delta_2(n)} = \frac{\Omega_1\Omega_2 g_a g_b}{\delta_1\delta_2\Delta}. \tag{1}$$

This is the photonic cavity analog of the Sørensen-Mølmer scheme [38] for the ion trap with phonons. The critical question now is how to precisely tune the detunings $\Delta_{1,2}$ and achieve the multiphoton resonance $|gg,n\rangle \leftrightarrow |rr,n\rangle$ for any n.

From the perturbative analysis, we obtain that the detunings $\Delta_{1,2}(n)$ depend on the cavity photon number n through the second-order (ac Stark) shifts of levels $|r\rangle_{1,2}$,

$$\Delta_1(n) \simeq \delta_1 + \frac{\Omega_1^2}{\delta_1} - \Delta_a - \frac{g_a^2(n+1)}{\delta_1} + \frac{g_b^2(n+2)}{\Delta_b},$$
$$\Delta_2(n) \simeq \delta_2 + \frac{\Omega_2^2}{\delta_2} + \Delta_b - \frac{g_a^2(n-1)}{\Delta_a} - \frac{g_b^2 n}{\delta_2}.$$

With an appropriate choice of $\delta_{1,2}$ and $\Omega_{1,2}$, and requiring that $\frac{g_a^2}{\Delta_a} = \frac{g_b^2}{\Delta_b}$, the n dependence of the detunings is greatly suppressed, $\Delta_{1,2}(n) \simeq \Delta_{1,2}(0)(1 + \frac{g_{a,b}^2}{\Delta_{a,b}^2}n)$, and we can satisfy the condition $|\Delta_1(n) + \Delta_2(n)| \ll \bar{\Omega}$ for any n. This leads to $\bar{\Omega}$ that only weakly depends on n, $\bar{\Omega}(n) \simeq \bar{\Omega}(0)(1 - \frac{g_a^2}{\Delta_a^2}n)$. In order to ensure the multiphoton resonance on the transition $|gg,n\rangle \to |rr,n\rangle$, we also need to consider higher-order level-shifts of $|gg,n\rangle$ and $|rr,n\rangle$. To fourth order in the laser and cavity field couplings, the largest contribution to the level shift of $|gg,n\rangle$ is given by $S_{gg}(n) = \frac{\Omega_1^2 g_a^2(n+1)}{\delta_1^2\Delta_1(n)} + \frac{\Omega_2^2 g_b^2 n}{\delta_2^2\Delta_2(n)}$, which, remarkably, has the same structure as $\bar{\Omega}$. Since $\Delta_1(n) \simeq -\Delta_2(n)$, we can choose $\frac{\Omega_1 g_a}{|\delta_1|} = \frac{\Omega_2 g_b}{|\delta_2|}$ to make S_{gg} nearly independent on n and absorb it into $\Delta_{1,2}(n)$. Finally, the fourth-order shifts of $|rr,n\rangle$, $S_{rr}(n) \propto \frac{g_{a,b}^4 n^2}{\Delta_{a,b}^3}$ [27] are small in comparison and can therefore be neglected, which we verify below through exact numerical simulations for the complete system.

In general, the atom-cavity couplings g_a and g_b are not equal, since they are proportional to the electric dipole matrix elements on different transitions $|r\rangle \to |a\rangle$ and $|r\rangle \to |b\rangle$, while the corresponding detunings Δ_a and Δ_b can be tuned by static electric (Stark) or magnetic (Zeeman) fields [32]. These, together with the flexibility to choose the laser detunings $\delta_{1,2}$ and Rabi frequencies $\Omega_{1,2}$, allows us to satisfy all of the above conditions for n-independent resonant Rabi oscillations between states $|gg\rangle$ and $|rr\rangle$. We can estimate the maximal attainable oscillation frequency $\bar{\Omega}$, assuming that the main limiting factor is the atom-cavity coupling strengths $g_{a,b}$ [28,30], since the laser Rabi frequencies can be collectively enhanced in the superatom regime [34,35,39]. Recall that we require the intermediate-state detunings $|\Delta_{1,2}(n)| \gg \tilde{\Omega}_{1,2}(n)$ for each $n \lesssim n_{\max}$. Then, with $\eta = |\delta_2|/\Omega_2$ and $\tilde{\eta} = |\Delta_1|/\tilde{\Omega}_1$ and all of the above conditions satisfied, we obtain $\bar{\Omega}_{\max} \leqslant \frac{g_b}{\eta\tilde{\eta}\sqrt{n_{\max}+1}}$. As an estimate, assuming $g_{a,b} \simeq 2\pi \times 10$ MHz, $\eta,\tilde{\eta} \simeq 10$ and a cavity mode with $\omega_c \simeq 2\pi \times 15$ GHz at $T = 4$ K, leading to $\bar{n}_{\rm th} \approx 5$ ($n_{\max} \approx 2\bar{n}_{\rm th}$), we have $\bar{\Omega}_{\max} \approx 2\pi \times 30$ kHz.

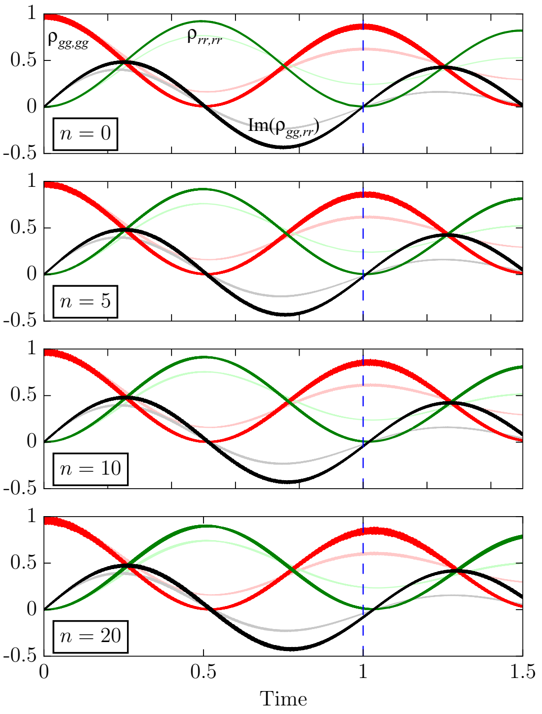

FIG. 2. (Color online) Rabi oscillation between states $|gg,n\rangle$ and $|rr,n\rangle$ for the cavity photon numbers $n = 0,5,10,20$. Thick (full) lines show coherent oscillations of populations $\rho_{gg,gg} = \langle gg|\,\hat{\rho}\,|gg\rangle$, $\rho_{rr,rr} = \langle rr|\,\hat{\rho}\,|rr\rangle$ and coherence $\rho_{gg,rr} = \langle gg|\,\hat{\rho}\,|rr\rangle$ for the Rydberg state decay $\Gamma = 0.142\,[\bar{\Omega}(0)/2\pi]$ and no dephasing, $\gamma = 0$, while thinner (shaded) lines show damped oscillations of the same quantities for large dephasing $\gamma = 0.4\,[\bar{\Omega}(0)/2\pi]$. Parameters are $\Omega_1 = 56.50, \Omega_2 = 60.00, \delta_1 = 663.8, \delta_2 = -742.0, g_a = 9.5, g_b = 10.0, \Delta_a = 722.0, \Delta_b = 800.0$ ($\times 2\pi$ MHz), leading to $\bar{\Omega}(0) \approx 2\pi \times 21.1$ kHz. Time is in units of $[2\pi/\bar{\Omega}(0)]$.

Note that, similarly to the ion trap scheme [38], our scheme would work in exactly the same way for the symmetric coupling of both atoms to both excitation lasers [Fig. 1(b)]. This opens two new excitation paths from $|gg,n\rangle$ to $|rr,n\rangle$ via states $|rg,n-1\rangle$ and $|gr,n+1\rangle$ [Fig. 1(c)], which enhances the transition amplitude $\bar{\Omega}$ by a factor of two. Care should be taken only to properly account for, and compensate for, the additional second- and fourth-order level shifts of the atomic ground states.

To validate our perturbative calculations, we numerically solve the master equation $\frac{\partial}{\partial t}\hat{\rho} = -\frac{i}{\hbar}[H,\hat{\rho}]$ for the density operator $\hat{\rho}$ using the exact Hamiltonian H for the pair of atoms initially in the ground state $|g\rangle$ and the cavity field with n photons. Results for different n are shown in Fig. 2, which verifies that with a proper choice of parameters, the transition resonance $|gg,n\rangle \leftrightarrow |rr,n\rangle$ and the effective Rabi frequency $\bar{\Omega}$ can simultaneously be made nearly independent of the number of photons in the cavity. We have examined various Fock, coherent and thermal states as the initial states of the cavity field, all yielding very similar results.

We include the realistic relaxation processes affecting the Rydberg states of atoms using the standard Liouvillians [40] with the Lindblad generators $\hat{L}_{\nu}^{(i)} = \sqrt{\Gamma}\,|g\rangle_i\langle\nu|$ for the decay with rate Γ (assumed the same for all $\nu = r,a,b$), and $\hat{L}_{g}^{(i)} = \sqrt{\gamma/2}(\,|g\rangle_i\langle g| - \sum_{\nu}\,|\nu\rangle_i\langle\nu|\,)$ for the dephasing (with respect to the ground state) with rate γ. In Fig. 2 we show strongly damped Rabi oscillations caused by the single-atom decay Γ and relatively large dephasing γ comparable to $\bar{\Omega}$.

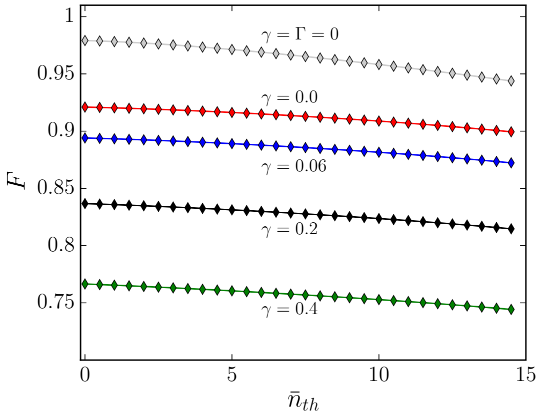

FIG. 3. (Color online) Transfer fidelity F at time $t_\pi = \pi/\bar{\Omega}(0)$ vs the mean number $\bar{n}_{\mathrm{th}}$ of thermal photons in the cavity, for the dephasing rates $\gamma = 0,0.06,0.2,0.4$ and the decay rates $\Gamma = 0$ (uppermost reference curve) and $\Gamma = 0.142$ (all other curves), in units of $[\bar{\Omega}(0)/2\pi]$. Other parameters are as in Fig. 2.

In Fig. 3 we plot the fidelity $F = \sum_n p(n|\bar{n}_{\mathrm{th}})\langle rr,n|\,\hat{\rho}(t_\pi)\,|rr,n\rangle$ of transfer $|gg\rangle \to |rr\rangle$ at time $t_\pi = \pi/\bar{\Omega}(0)$ (effective π pulse for $n = 0$) as a function of the dephasing rate γ and the mean number of thermal photons $\bar{n}_{\mathrm{th}}$ which determines the photon number probability distribution $p(n|\bar{n}_{\mathrm{th}}) = \bar{n}_{\mathrm{th}}^{n}/(\bar{n}_{\mathrm{th}}+1)^{n+1}$. We observe that large dephasing detrimentally affects the transfer fidelity by damping the amplitude of Rabi osculations between $|gg\rangle$ and $|rr\rangle$. On the other hand, the fidelity only weakly and nearly linearly decreases with increasing the cavity photon number, due to the slight decrease of the effective Rabi frequency $\bar{\Omega}(n)$ discussed above. This can be compensated for by appropriately correcting the transfer time t_π if $\bar{n}_{\mathrm{th}}$ is approximately known.

We now discuss the implications of our results for quantum information applications. Each atom can encode a qubit as a coherent superposition of long-lived states $|g\rangle$ and $|s\rangle$ [Fig. 1(b)]. Gate operation can be performed on any pair of atoms within the cavity by addressing the desired atoms with focused laser pulses $\Omega_{1,2}$. Assuming that state $|s\rangle$ is decoupled from the laser field(s), the two-atom state $|ss\rangle$ is immune to the lasers. If only one of the atoms is initially in state $|g\rangle$ and the other atom is in $|s\rangle$, both atoms remain in their initial states due to the absence of multiphoton resonances to any Rydberg state. Finally, if both atoms are in state $|g\rangle$, the application of lasers for time $t_{2\pi} = 2\pi/\bar{\Omega}$ will drive a complete Rabi cycle on the transition $|gg\rangle \leftrightarrow |rr\rangle$, resulting in the sign change of $|gg\rangle$. Since the other initial states remain unaltered, this transformation corresponds to the universal two-qubit CPHASE logic gate [40,41].

Our scheme is also applicable to ensembles of trapped atoms in the Rydberg blockade regime [34,35]. Individual ensembles, each containing $N_i \gg 1$ atoms, can encode qubits in the collective ground $|G\rangle \equiv$

$|g_1,g_2,\dots,g_{N_i}\rangle$ and symmetric single spin-flip (hyperfine) $|S\rangle \equiv \frac{1}{\sqrt{N_i}}\sum_{k=1}^{N_i}|g_1,\dots,s_k,\dots,g_{N_i}\rangle$ states. For optically dense ensembles, the qubit encoding superposition of states $|G\rangle$ and $|S\rangle$ can be reversibly mapped onto photonic qubits via stimulated Raman techniques [8]. We assume that each ensemble of linear dimension smaller than a certain blockade distance d_{bl} [Fig. 1(a)] behaves as a Rydberg superatom [34,35,39], wherein multiple excitations are suppressed by the strong Rydberg-state interactions. This allows implementation of arbitrary single-qubit and universal two-qubit quantum gates as follows. In each ensemble, before and after the gate execution, we apply a single-atom π pulse on the transition $|s\rangle \to |r'\rangle$, where $|r'\rangle$ is a Rydberg state which can block excitation of any other atom from state $|g\rangle$ to states $|r'\rangle, |r\rangle$ (and, possibly, to $|a\rangle, |b\rangle$) due to the strong dipole-dipole or van der Waals interactions [35]. This operation reversibly maps the qubit state $|S\rangle$ onto the symmetric single Rydberg excitation state $|R'\rangle \equiv \frac{1}{\sqrt{N_i}}\sum_{k=1}^{N_i}|g_1,\dots,r'_k,\dots,g_{N_i}\rangle$. Single-qubit transformations are then performed in the two-state subspace of $|G\rangle$ and $|R'\rangle$ by resonant lasers with collectively enhanced Rabi frequencies $\Omega = \sqrt{N_i}\Omega^{(1)}$, where $\Omega^{(1)}$ is the single-atom Rabi frequency on the transition $|g\rangle \leftrightarrow |r'\rangle$ [34]. For the two-qubit operations, any pair of atomic ensembles i,j trapped within the cavity can be addressed by appropriate lasers with collectively enhanced Rabi frequencies $\Omega_{1,2} = \sqrt{N_{i,j}}\Omega_{1,2}^{(1)}$. Then, during time $t_{2\pi}$, the initial state $|G\rangle_i|G\rangle_j$ will undergo a complete Rabi cycle to $|R\rangle_i|R\rangle_j$ and back, acquiring a π phase shift (sign change), assuming that in each ensemble multiple excitations of $|r\rangle$ are blocked by strong Rydberg-state interactions. If any, or both, of the ensembles were initially in state $|S\rangle$ mapped onto $|R'\rangle$, the atom in $|r'\rangle$ would preclude the transfer of ground-state atoms $|g\rangle$ to $|r\rangle$, and therefore such initial states will remain unaltered. This completes the implementation of the CPHASE logic gate with Rydberg superatoms.

To conclude, our scheme to implement long-range quantum gates is feasible with present-day experimental technologies [21,22,30,31,33] involving optical excitation of Rydberg states of trapped atoms and their interactions with microwave resonators. This gate is largely insensitive to the number of cavity photons and it can therefore operate in a finite-temperature microwave cavity with modest photon lifetimes $1/\kappa \gtrsim 1\,\mu$s. The main decoherence mechanisms reducing the achievable gate fidelity $F \simeq 1-(\Gamma+\gamma)\tau$ during time $\tau = 2\pi/\bar{\Omega}(0) \sim 50\,\mu$s are the decay $\Gamma \simeq 3$ kHz of Rydberg states and dephasing $\gamma \lesssim 5$ kHz of the nonresonant multiphoton transitions [with $\Delta \gg \tilde{\Omega}_{1,2}(n)$], which are slow by construction [38]. It would thus be interesting to explore the near-resonant excitations [with $\Delta/\tilde{\Omega}_1(0) = 2\sqrt{m}$ ($m = 1,2,\dots$)] analogous to the fast-gate regime of the ion traps [42]. Unlike our present gate, however, such a fast-gate scheme will be sensitive to the change of cavity photon number [43] during the gate time $\tau = 2\pi\sqrt{m}/\tilde{\Omega}_1(0) \sim 10\,\mu$s requiring cavities with longer photon lifetimes $1/\kappa \gg \tau$.

We thank Klaus Mølmer for useful comments and suggestions. This work was supported by the Deutsche Forschungsgemeinschaft SFB TRR21, the European Union FP7 STREP Project HAIRS, and H2020 FET Proactive Project RySQ. D.P. is grateful to the University of Kaiserslautern for hospitality and to the Alexander von Humboldt Foundation for support during his stay in Germany.

[1] M. Wallquist, K. Hammerer, P. Rabl, M. Lukin, and P. Zoller, Phys. Scr., **T137**, 014001 (2009).
[2] G. Bensky, R. Amsüss, J. Majer, D. Petrosyan, J. Schmiedmayer, and G. Kurizki, Quant. Info. Proc. **10**, 1037 (2011).
[3] Z.-L. Xiang, S. Ashhab, J. Q. You, and F. Nori, Rev. Mod. Phys. **85**, 623 (2013).
[4] G. Kurizki, P. Bertet, Y. Kubo, K. Mølmer, D. Petrosyan, P. Rabl, and J. Schmiedmayer, PNAS **112**, 3866 (2015).
[5] R. J. Schoelkopf and S. M. Girvin, Nature (London) **451**, 664 (2008).
[6] M. H. Devoret and R. J. Schoelkopf, Science **339**, 1169 (2013).
[7] A. I. Lvovsky, B. C. Sanders, and W. Tittel, Nat. Photon. **3**, 706 (2009).
[8] M. Fleischhauer, A. Imamoglu, and J. P. Marangos, Rev. Mod. Phys. **77**, 633 (2005).
[9] A. V. Sergienko, *Quantum Communications and Cryptography*, edited by A. V. Sergienko (Taylor and Francis, Boca Raton, FL, 2006).
[10] K. Hammerer, A. S. Sørensen, and E. S. Polzik, Rev. Mod. Phys. **82**, 1041 (2010).
[11] N. Sangouard, C. Simon, H. de Riedmatten, and N. Gisin, Rev. Mod. Phys. **83**, 33 (2011).
[12] A. Blais, R.-S. Huang, A. Wallraff, S. M. Girvin, and R. J. Schoelkopf, Phys. Rev. A **69**, 062320 (2004).
[13] M. A. Sillanpaa, J. I. Park, and R. W. Simmonds, Nature (London) **449**, 438 (2007).
[14] L. DiCarlo, J. M. Chow, J. M. Gambetta, L. S. Bishop, B. R. Johnson, D. I. Schuster, J. Majer, A. Blais, L. Frunzio, S. M. Girvin, and R. J. Schoelkopf, Nature (London) **460**, 240 (2009).
[15] M. D. Reed, L. DiCarlo, S. E. Nigg, L. Sun, L. Frunzio, S. M. Girvin, and R. J. Schoelkopf, Nature (London) **482**, 382 (2012).
[16] X. Zhu, S. Saito, A. Kemp, K. Kakuyanagi, S.-i. Karimoto, H. Nakano, W. J. Munro, Y. Tokura, M. S. Everitt, K. Nemoto, M. Kasu, N. Mizuochi, and K. Semba, Nature (London) **478**, 221 (2011).
[17] Y. Kubo, C. Grezes, A. Dewes, T. Umeda, J. Isoya, H. Sumiya, N. Morishita, H. Abe, S. Onoda, T. Ohshima, V. Jacques, A. Dréau, J.-F. Roch, I. Diniz, A. Auffeves, D. Vion, D. Esteve, and P. Bertet, Phys. Rev. Lett. **107**, 220501 (2011).
[18] S. Saito, X. Zhu, R. Amsüss, Y. Matsuzaki, K. Kakuyanagi, T. Shimo-Oka, N. Mizuochi, K. Nemoto, W. J. Munro, and K. Semba, Phys. Rev. Lett. **111**, 107008 (2013).
[19] P. Treutlein, P. Hommelhoff, T. Steinmetz, T. W. Hänsch, and J. Reichel, Phys. Rev. Lett. **92**, 203005 (2004).
[20] J. Fortágh and C. Zimmermann, Rev. Mod. Phys. **79**, 235 (2007).

[21] C. Roux, A. Emmert, A. Lupascu, T. Nirrengarten, G. Nogues, M. Brune, J.-M. Raimond, and S. Haroche, Europhys. Lett. **81**, 56004 (2008).

[22] S. Bernon, H. Hattermann, D. Bothner, M. Knufinke, P. Weiss, F. Jessen, D. Cano, M. Kemmler, R. Kleiner, D. Koelle, and J. Fortágh, Nat. Commun. **4**, 2380 (2013).

[23] L. Sárkány, P. Weiss, H. Hattermann, and J. Fortágh, Phys. Rev. A **90**, 053416 (2014).

[24] P. Rabl, D. DeMille, J. M. Doyle, M. D. Lukin, R. J. Schoelkopf, and P. Zoller, Phys. Rev. Lett. **97**, 033003 (2006).

[25] K. Tordrup and K. Mølmer, Phys. Rev. A **77**, 020301 (2008).

[26] J. Verdú, H. Zoubi, C. Koller, J. Majer, H. Ritsch, and J. Schmiedmayer, Phys. Rev. Lett. **103**, 043603 (2009).

[27] D. Petrosyan and M. Fleischhauer, Phys. Rev. Lett. **100**, 170501 (2008).

[28] D. Petrosyan, G. Bensky, G. Kurizki, I. Mazets, J. Majer, and J. Schmiedmayer, Phys. Rev. A **79**, 040304 (2009).

[29] J. D. Pritchard, J. A. Isaacs, M. A. Beck, R. McDermott, and M. Saffman, Phys. Rev. A **89**, 010301 (2014).

[30] S. D. Hogan, J. A. Agner, F. Merkt, T. Thiele, S. Filipp, and A. Wallraff, Phys. Rev. Lett. **108**, 063004 (2012).

[31] C. Hermann-Avigliano, R. C. Teixeira, T. L. Nguyen, T. Cantat-Moltrecht, G. Nogues, I. Dotsenko, S. Gleyzes, J. M. Raimond, S. Haroche, and M. Brune, Phys. Rev. A **90**, 040502 (2014); R. C. Teixeira, C. Hermann-Avigliano, T. L. Nguyen, T. Cantat-Moltrecht, J. M. Raimond, S. Haroche, S. Gleyzes, and M. Brune, Phys. Rev. Lett. **115**, 013001 (2015).

[32] T. Gallagher, *Rydberg Atoms* (Cambridge University Press, Cambridge, UK, 1994).

[33] F. Jessen, M. Knufinke, S. Bell, P. Vergien, H. Hattermann, P. Weiss, M. Rudolph, M. Reinschmidt, K. Meyer, T. Gaber, D. Cano, A. Günther, S. Bernon, D. Koelle, R. Kleiner, and J. Fortágh, Appl. Phys. B **116**, 665 (2014).

[34] M. D. Lukin, M. Fleischhauer, R. Cote, L. M. Duan, D. Jaksch, J. I. Cirac, and P. Zoller, Phys. Rev. Lett. **87**, 037901 (2001).

[35] M. Saffman, T. G. Walker, and K. Mølmer, Rev. Mod. Phys. **82**, 2313 (2010); D. Comparat and P. Pillet, J. Opt. Soc. Am. B **27**, A208 (2010).

[36] T. Mukai, C. Hufnagel, A. Kasper, T. Meno, A. Tsukada, K. Semba, and F. Shimizu, Phys. Rev. Lett. **98**, 260407 (2007).

[37] D. Cano, H. Hattermann, B. Kasch, C. Zimmermann, R. Kleiner, D. Koelle, and J. Fortágh, Eur. Phys. J. D **63**, 17 (2011).

[38] A. Sørensen and K. Mølmer, Phys. Rev. Lett. **82**, 1971 (1999); K. Mølmer and A. Sørensen, *ibid.* **82**, 1835 (1999).

[39] T. M. Weber, M. Honing, T. Niederprum, T. Manthey, O. Thomas, V. Guarrera, M. Fleischhauer, G. Barontini, and H. Ott, Nat. Phys. **11**, 157 (2015); M. Ebert, M. Kwon, T. G. Walker, and M. Saffman, Phys. Rev. Lett. **115**, 093601 (2015); J. Zeiher, P. Schauß, S. Hild, T. Macrì, I. Bloch, and C. Gross, Phys. Rev. X **5**, 031015 (2015).

[40] P. Lambropoulos and D. Petrosyan, *Fundamentals of Quantum Optics and Quantum Information* (Springer, Berlin, 2007).

[41] M. Nielsen and I. Chuang, *Quantum Computation and Quantum Information* (Cambridge University Press, Cambridge, UK, 2000).

[42] A. Sørensen and K. Mølmer, Phys. Rev. A **62**, 022311 (2000); C. A. Sackett, D. Kielpinski, B. E. King, C. Langer, V. Meyer, C. J. Myatt, M. Rowe, Q. A. Turchette, W. M. Itano, D. J. Wineland, and C. Monroe, Nature (London) **404**, 256 (2000).

[43] C. F. Roos, New J. Phys. **10**, 013002 (2008).

PRL **114,** 113003 (2015) PHYSICAL REVIEW LETTERS week ending 20 MARCH 2015

Sensitivity of Ultracold Atoms to Quantized Flux in a Superconducting Ring

P. Weiss,[*] M. Knufinke, S. Bernon,[†] D. Bothner, L. Sárkány, C. Zimmermann,
R. Kleiner, D. Koelle, J. Fortágh,[‡] and H. Hattermann
*CQ Center for Collective Quantum Phenomena and their Applications in LISA$^+$, Physikalisches Institut,
Eberhard Karls Universität Tübingen, Auf der Morgenstelle 14, D-72076 Tübingen, Germany*

(Received 4 September 2014; published 17 March 2015)

We report on the magnetic trapping of an ultracold ensemble of ^{87}Rb atoms close to a superconducting ring prepared in different states of quantized magnetic flux. The niobium ring of 10 μm radius is prepared in a flux state $n\,\Phi_0$, where $\Phi_0 = h/2e$ is the flux quantum and n varying between ± 6. An atomic cloud of 250 nK temperature is positioned with a harmonic magnetic trapping potential at $\sim$18 μm distance below the ring. The inhomogeneous magnetic field of the supercurrent in the ring contributes to the magnetic trapping potential of the cloud. The induced deformation of the magnetic trap impacts the shape of the cloud, the number of trapped atoms, as well as the center-of-mass oscillation frequency of Bose-Einstein condensates. When the field applied during cooldown of the chip is varied, the change of these properties shows discrete steps that quantitatively match flux quantization.

DOI: 10.1103/PhysRevLett.114.113003 PACS numbers: 37.10.Gh, 74.25.Ha, 85.25.-j

The coherent coupling between atoms and single flux quanta in a superconducting circuit is an important ingredient of future cold atom—superconductor hybrid quantum systems in which quantum states are transferred from one system to the other. The construction of such a hybrid quantum system is targeted in a number of recent experiments and proposals [1–13], and should allow the study of fundamental interactions between the two systems [14–19]. One of the most prominent consequences of the existence of a macroscopic wave function in superconductors is the quantization of the magnetic fluxoid, which has been shown, e.g., in superconducting rings and cylinders [20,21]. In superconducting atom chip experiments, trapped Abrikosov vortices have been used to magnetically trap atoms in spatially inhomogeneous fields [22–27]. These traps are affected by the motion of the vortices that potentially cause heating and losses of the cold atoms [28,29]. Pinning the vortices would suppress this noise source and could be used to generate subwavelength magnetic lattices [30], as well as hybrid quantum systems based on atom traps formed by single pinned flux quanta [31]. The creation of a flux superposition state could give rise to a superposition of the magnetic trapping potential and therefore of the position of an atomic ensemble [32]. Ultrafast state transfer (10 ns) between cold Rydberg atoms and superconducting quantum interference devices has also been theoretically predicted [33]. It is therefore crucial to understand the impact of single flux quanta onto an ensemble of trapped ultracold atoms.

In this Letter, we report on how a discrete number of flux quanta stored in a superconducting ring affects the trapping parameters of a superimposed magnetic trap. The discrete nature of the magnetic flux in the ring is observed both in the atom number and the oscillation frequency of atoms in the trap.

We magnetically trap an ensemble of cold ^{87}Rb atoms on a superconducting atom chip and guide it to the vicinity of a superconducting ring, as sketched in Fig. 1(a). The atom chip [Fig. 1(b)] is a sapphire substrate ($\sim$330 μm thick) with patterned niobium thin film structures (thickness $d = 500$ nm). The chip contains several Z-shaped lines (“trapping wires”) of different widths used for trapping and moving the atoms, the broadest of which (100 μm wide) is used to trap atoms in the experiments described in this Letter. The ring has an inner radius $r_i = 9$ μm and an outer radius $r_o = 11$ μm. It is placed 70 μm from the edge of the trapping wire in the y direction. The superconducting atom chip [5] is attached to the cold finger of a helium flow cryostat at temperature $T = 4.2$ K. The atoms are prepared in the hyperfine ground state $5S_{1/2}F = 1$, $m_F = -1$ in a room temperature part of the setup and subsequently transported to a position below the superconducting chip by means of optical tweezers, as detailed in Ref. [34].

The microtrap is realized by the superposition of the fields generated by a current in the trapping wire and a homogeneous external bias field $\vec{B}_{\text{bias}}$. An ensemble of $N \sim 1.5 \times 10^6$ atoms at $T_{\text{atom}} \sim 1$ μK is loaded from the optical tweezers into this superconducting microtrap, formed at 400 μm from the chip surface. After adiabatic compression, the cloud is evaporatively cooled to achieve either a thermal cloud or a nearly pure Bose-Einstein condensate. The ensemble is then magnetically transported to a position $z \sim 18$ μm below the superconducting ring by rotating $\vec{B}_{\text{bias}}$ around the x axis [Fig. 1(b)] and adjusting the current in the wire. The longitudinal position of the cloud along x is controlled by an additional field $\vec{B}_{\text{conf}}$ created by a confinement wire on the back side of the chip, see Ref. [5] for details.

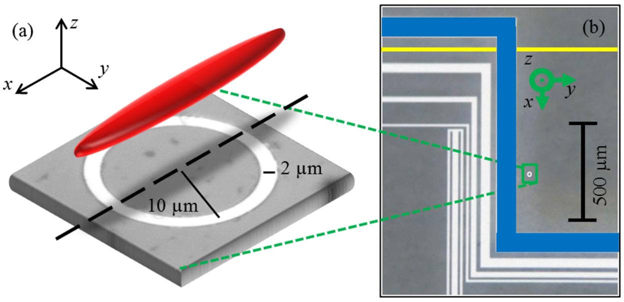

FIG. 1 (color online). (a) Sketch of an atomic ensemble trapped at the superconducting ring. (b) Optical image of parts of the superconducting chip. Shown are four trapping wires; the 100 μm wide trapping wire used for the present experiment is highlighted in blue. The location of the confinement wire is sketched in yellow. The center of the superconducting ring is located 70 μm from the right edge of the trapping wire. The chip is mounted upside down on the cryostat, so gravity points in the $+z$ direction.

The macroscopic superconducting ring exhibits quantum behavior that impacts the cold atomic cloud. In the superconducting state the fluxoid is quantized [35] as

$$n \cdot \Phi_0 = \mu_0 \lambda_L^2 \oint \vec{j} \cdot d\vec{s} + \Phi. \tag{1}$$

This follows from the fact that the single-valuedness of the wave function requires any closed integral over the wave vector to be an integer multiple of 2π. Here, $\Phi_0 = h/2e$ is the magnetic flux quantum and the right hand side needs to be evaluated along a closed contour within the superconductor. λ_L ($\sim$100 nm for our Nb thin films) is the London penetration depth, $\vec{j}$ is the supercurrent density, and Φ is the total magnetic flux through the closed contour. If the superconductor is large compared to λ_L, which is the case for our geometry at temperatures well below the transition temperature T_c, the integral over $\vec{j}$ can be neglected. Then, Φ is quantized in multiples of Φ_0:

$$n \cdot \Phi_0 = \Phi = \int \vec{B} \cdot d\vec{A}. \tag{2}$$

Φ is given by the sum of the flux applied above T_c, $\Phi_{\text{freeze}} = \int \vec{B}_{\text{freeze}} \cdot d\vec{A}$, and the flux LJ created by the supercurrents J circulating around the ring

$$n \cdot \Phi_0 = \Phi_{\text{freeze}} + LJ. \tag{3}$$

Here, L is the inductance of the ring and $\vec{B}_{\text{freeze}}$ is the magnetic field applied to the ring during cooling. After cooling through T_c the value of n is defined as the integer closest to $\Phi_{\text{freeze}}/\Phi_0$.

Using $\Phi_0 = \Delta B_{\text{freeze}} \pi r_i r_o$ [36], we expect for our geometry a field increment ΔB_{freeze} of about 66.5 mG to change the flux in the ring by $1\Phi_0$. Having turned off $\vec{B}_{\text{freeze}}$, the (quantized) flux through the ring is conserved by the induced circulating current J_{freeze}. Any fields applied to the ring in the superconducting state, for instance, by the magnetic trap, are compensated by screening currents J_{screen}, so that the total current is $J = J_{\text{freeze}} + J_{\text{screen}}$.

The magnetic (dipole) field $\vec{B}_{\text{ring}}$ created by currents J locally modifies the magnetic trapping potential for the atoms in the vicinity of the structure. To estimate the contribution of $\vec{B}_{\text{ring}}$ and its impact on the trapping potential, let us consider a cigar-shaped harmonic trap with oscillation frequencies $\omega_x \ll \omega_{y,z}$, whose radial axis y is centered above the ring and whose size is on the order of the ring diameter. The offset field B_x at the minimum of the trap is considered to point along the x axis. The x component of $\vec{B}_{\text{ring}}$ increases B_x on one side of the ring and reduces it on the other [Fig. 2(a)], which leads to an asymmetric double well potential for the cold atomic cloud [Figs. 2(b) and 2(c)]. Hence, $\vec{B}_{\text{ring}}$ leads to a position shift of the minimum of the magnetic trapping potential along the longitudinal axis. In addition, the position of the potential minimum is shifted towards the surface with increasing number of flux quanta in the ring and the barrier height (trap depth) between the dimple and the surface is reduced.

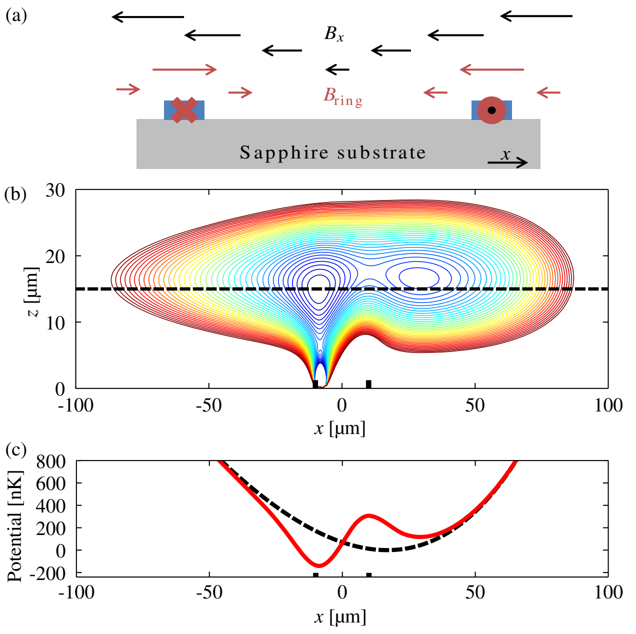

FIG. 2 (color online). (a) Cross section along the dashed line in Fig. 1(a) with the principal magnetic x field components of the trap and the ring in the longitudinal direction. (b) Isopotential plot of the calculated trapping potential for four flux quanta in the ring. An asymmetric potential with two local minima is created, with the lower minimum (dimple) above the ring structure (black markers on the x axis). Each contour line corresponds to an energy change of $k_B \times 50$ nK. (c) Calculated potential along the longitudinal axis [black line Fig. 2(b)] with four flux quanta in the ring (solid red) and the unperturbed harmonic trap (dashed).

This effect leads to a decrease in the number and temperature of atoms trappable in this dimple. Using the method described in Ref. [37] for the simulation of the supercurrent densities in the trapping wire and the ring, we numerically calculate the field distribution composed of the ring field and the trapping field with Biot-Savart's law. The results of these calculations are in good agreement with simulations based on inductance calculations (3D-MLSI software package) [38]. Below the ring structure, the ring field for $1\Phi_0$ leads to a field shift of ~3 mG as compared with the unperturbed harmonic trap [Fig. 2(c)], corresponding to a dimple with a depth on the order of 100 nK. Furthermore, the alteration of the potential landscape caused by the circular supercurrents leads to a longitudinal center-of-mass oscillation frequency that depends on the number of flux quanta n in the ring.

For the measurements, we first prepare the flux state of the ring by heating up the chip to a temperature above T_c and subsequently cool it to $T = 4.2$ K in a homogeneous magnetic field $\vec{B}_{\mathrm{freeze}}$, applied perpendicular to the surface and ranging from -500 to 500 mG. The magnetic fields are calibrated by microwave spectroscopy; i.e., the atoms are prepared in the state $F = 1, m_F = -1$ and the number of atoms in the state $F = 2, m_F = 0$ is measured after application of a microwave pulse with variable frequency. Limited by fluctuations of the magnetic field in the laboratory, the absolute value of B_{freeze} is known within ± 5 mG.

A thermal cloud of $N \sim 2 \times 10^5$ atoms with a temperature of ~250 nK is prepared below the trapping wire and brought close to the ring, where it is held for 1 s. For each value of B_{freeze} we take nine absorption images in situ by reflection imaging [39] along the y direction. After averaging over the images, we integrate the calculated column density along the z direction to obtain a one-dimensional profile of the atomic cloud along the axis of weak confinement to reveal the impact of the ring field along x. In Fig. 3(a) the density profiles are plotted versus B_{freeze}. We observe steps in the integrated density profile occurring when the number of flux quanta in the ring changes. For certain flux states, two distinct density peaks, which indicate the double well potential, are discernible. By further integration of the profiles shown in Fig. 3(a), we obtain the atom number N as a function of B_{freeze}. The atom number is normalized to the maximum number measured in the trap and plotted in Fig. 3(b). There are clearly visible equidistant steps with a width of $\Delta B_{\mathrm{freeze}} = 65.9 \pm 2.3$ mG, indicated by the blue vertical lines. The theoretically predicted value of $\Delta B_{\mathrm{freeze}} = 66.5$ mG per flux quantum is well within the error bars of the measurement. In Fig. 3(b) it is visible that we achieve a resolution better than single flux quanta.

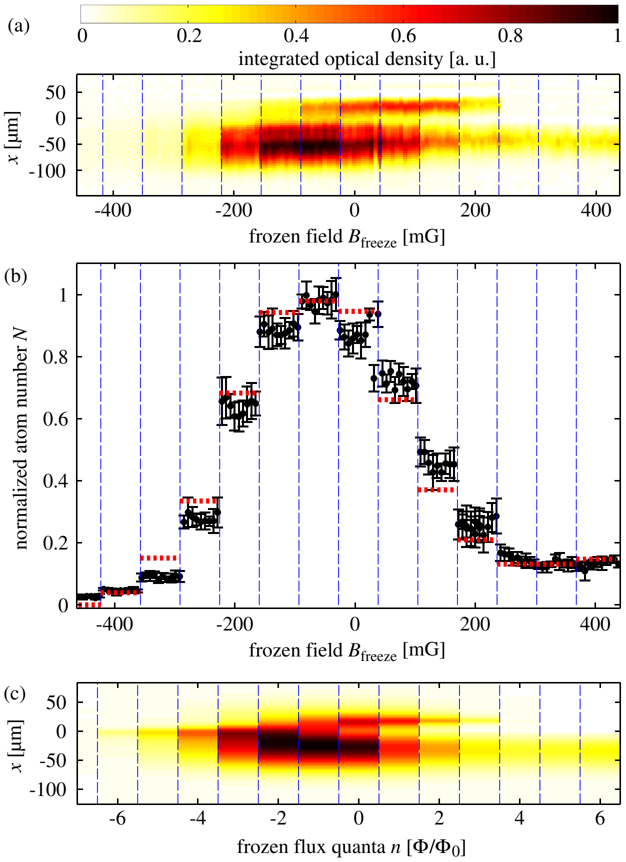

FIG. 3 (color online). (a) Measured integrated density profile for different freezing fields. Each column represents the integrated density profile averaged over nine absorption images. Adjacent lines differ by 7 mG in the field applied during cooling. The split in the density profile shows the emergence of the double well potential due to the ring field. (b) Relative atom number of an ensemble trapped at the superconducting ring, obtained by integrating the density profile along the x axis shown in (a). The mean atom number is calculated from nine pictures per frozen field applied during cooling. The dashed vertical lines have a spacing of 65.9 mG, which is the measured value for one flux quantum. The atom number is normalized to the maximum number measured in the trap. The red dotted lines indicate the calculated atom numbers obtained from the numerical simulation of the Boltzmann distribution. (c) Integrated density profile calculated from the predicted trapping potential using Boltzmann distributed atoms.

The measurements in Fig. 3(b) are not symmetric around the value $B_{\mathrm{freeze}} = 0$. As the magnetic trap itself has a magnetic field component perpendicular to the surface, a screening current J_{screen} is induced in the ring to compensate this field. The screening current contributes to the trapping potential even for $B_{\mathrm{freeze}} = 0$. Only if the sum of the fields perpendicular to the ring is equal to the number of trapped flux quanta, the harmonic trap is unperturbed by the screening currents. In this case, there is no net current around the ring, i.e., $J_{\mathrm{screen}} = -J_{\mathrm{freeze}}$, and only Meissner currents, which keep the superconducting film itself field free, are present [37].

To gain a qualitative understanding of the impact of the screening currents on the density profile, we set up a simplified model and numerically calculate the modification of the trapping potential for different numbers of flux quanta in the ring. We simulate the atomic density in the trap using a Maxwell-Boltzmann distribution for the energy, assuming a maximum temperature of $T_{\max} = 230$ nK. As the barrier height between the trap and the surface (trap depth) depends on the number of flux quanta n in the ring, we truncate the energy in the Boltzmann distribution to the trap depth, which changes the volume occupied by the cloud [40–42]. Furthermore, we incorporate the loss of atoms according to a heuristic scaling of the atomic density, assuming $\rho(n)/\rho_{\max} = T_{\text{depth}}(n)/T_{\text{depth}}(0)$. The simulations take into account the existence of a double well potential, in which both traps have different trap depths. To compare the calculations with the observed density profiles, we sum over the calculated atomic density along the y and z directions and plot the result versus the number of frozen flux quanta n. The result is shown in Fig. 3(c), which closely resembles the experimental data in Fig. 3(a). The number of trapped atoms is estimated by additionally summing up the density distribution [Fig. 3(c)] along the x direction, which leads to the red dashed lines in Fig. 3(b). Our simple model qualitatively and moderately quantitatively matches the behavior of the measured atom number for different flux quanta n and justifies the assumed scaling in the densities. We attribute the discrepancies between experiment and simulation to losses during the loading process of the double well, which are not taken into account in the calculations.

In order to obtain additional information on the number of frozen flux quanta, we have performed a measurement of the center-of-mass oscillation frequency of the trap at the ring for various values of B_{freeze}. For this measurement, we prepared a Bose-Einstein condensate filling only the low-lying dimple of the potential with atoms, where the trap frequency is expected to vary significantly with the number of flux quanta. To measure the frequency, a center-of-mass oscillation of the atoms along the longitudinal axis of the trap was excited by rapidly displacing the minimum of the magnetic potential using the current in the confinement wire. After a variable hold time (0 to 200 ms), a microwave pulse was applied to transfer the atoms into the untrapped $F = 2, m_F = 0$ state and the oscillation frequency was extracted from the position of the cloud after a time of flight of 12 ms. Figure 4 shows the measured oscillation frequencies along the expected values extracted from our simulation of the potential. The dashed vertical lines are based on an atom number measurement similar to that in Fig. 3(b) and show the expected values of B_{freeze} at which the number of flux quanta in the ring changes. The simulations are in qualitative agreement with the measurement and show our resolution on the level of single flux quanta; deviations between experiment and calculation can be attributed to uncertainties in the applied magnetic fields.

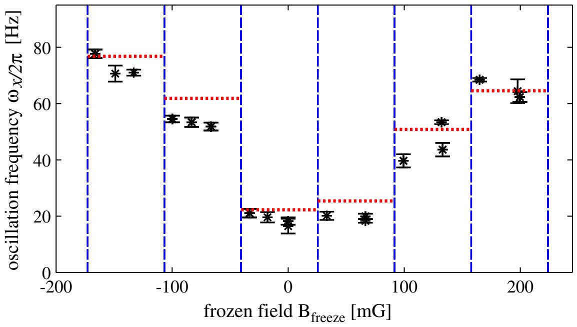

FIG. 4 (color online). Trapping frequencies measured for different freezing fields. The dashed vertical lines indicate the jumps in the number of flux quanta. The black dots with error bars were obtained from the measurement. The dotted horizontal lines are calculated values for different numbers of frozen flux quanta.

In summary, we have demonstrated that a cold atomic cloud of ^{87}Rb atoms positioned close to a superconducting ring is sensitive to the magnetic field created by single flux quanta. The modification of the trapping potential by this field is detectable in two trap characteristics: first, in the trap depth and therefore in the atom number of the ensemble, and, second, in the trapping frequency inside the created dimple trap. We also expect that the variation of the number of flux quanta in the ring will impact internal degrees of freedom of the trapped atoms, such as the energy difference between Zeeman sublevels, which is accessible by means of Ramsey interferometry. This sensitivity paves the way towards future experiments that, e.g., interface superconducting quantum interference devices and cold atomic clouds and exploit the atomic ensemble as a robust quantum memory [43]. Strong coupling, as demonstrated for example with nitrogen vacancy centers [44], could be achieved for cold atoms by reducing the loop size, resulting in larger fields per flux quantum, or by bosonic enhancement of the coupling strength between two macroscopically populated atomic states [33]. The impact of the applied magnetic fields, trapped flux within the superconducting structures, and stray light on the coherence of the superconducting circuits is yet to be studied, but is not expected to fundamentally limit the coupling between the two systems.

The authors would like to thank Thomas Dahm and Igor Sapina for useful discussions. This work was supported the Deutsche Forschungsgemeinschaft (SFB TRR21) and by the European Research Council (Socathes). The authors acknowledge additional support from the ev. Studienwerk Villigst e.V., and the Carl Zeiss Stiftung.

---

[*] pweiss@pit.physik.uni-tuebingen.de

[†] Present address: Laboratoire Photonique, Numérique et Nanosciences-LP2N Université Bordeaux-IOGS-CNRS: UMR 5298-Rue François Mitterrand, 33400 Talence, France.

[‡] fortagh@uni-tuebingen.de

[1] P. Rabl, D. DeMille, J. M. Doyle, M. D. Lukin, R. J. Schoelkopf, and P. Zoller, Phys. Rev. Lett. **97**, 033003 (2006).

[2] D. Petrosyan and M. Fleischhauer, Phys. Rev. Lett. **100**, 170501 (2008).

[3] D. Petrosyan, G. Bensky, G. Kurizki, I. Mazets, J. Majer, and J. Schmiedmayer, Phys. Rev. A **79**, 040304 (2009).

[4] J. Verdú, H. Zoubi, C. Koller, J. Majer, H. Ritsch, and J. Schmiedmayer, Phys. Rev. Lett. **103**, 043603 (2009).

[5] S. Bernon, H. Hattermann, D. Bothner, M. Knufinke, P. Weiss, F. Jessen, D. Cano, M. Kemmler, R. Kleiner, D. Koelle, and J. Fortágh, Nat. Commun. **4**, 2380 (2013).

[6] K. R. Patton and U. R. Fischer, Phys. Rev. A **87**, 052303 (2013).

[7] S. D. Hogan, J. A. Agner, F. Merkt, T. Thiele, S. Filipp, and A. Wallraff, Phys. Rev. Lett. **108**, 063004 (2012).

[8] Z. Kim, C. P. Vlahacos, J. E. Hoffman, J. A. Grover, K. D. Voigt, B. K. Cooper, C. J. Ballard, B. S. Palmer, M. Hafezi, J. M. Taylor, J. R. Anderson, A. J. Dragt, C. J. Lobb, L. A. Orozco, S. L. Rolston, and F. C. Wellstood, AIP Adv. **1**, 042107 (2011).

[9] M. Wallquist, K. Hammerer, P. Rabl, M. Lukin, and P. Zoller, Phys. Scr. **T137**, 014001 (2009).

[10] M. Hafezi, Z. Kim, S. L. Rolston, L. A. Orozco, B. L. Lev, and J. M. Taylor, Phys. Rev. A **85**, 020302 (2012).

[11] F. Jessen, M. Knufinke, S. Bell, P. Vergien, H. Hattermann, P. Weiss, M. Rudolph, M. Reinschmidt, K. Meyer, T. Gaber, D. Cano, A. Günther, S. Bernon, D. Koelle, R. Kleiner, and J. Fortágh, Appl. Phys. B **116**, 665 (2014).

[12] S. Minniberger, F. Diorico, S. Haslinger, C. Hufnagel, C. Novotny, N. Lippok, J. Majer, C. Koller, S. Schneider, and J. Schmiedmayer, Appl. Phys. B **116**, 1017 (2014).

[13] J. D. Pritchard, J. A. Isaacs, M. A. Beck, R. McDermott, and M. Saffman, Phys. Rev. A **89**, 010301 (2014).

[14] S. Scheel, P. K. Rekdal, P. L. Knight, and E. A. Hinds, Phys. Rev. A **72**, 042901 (2005).

[15] B. K. Skagerstam, U. Hohenester, A. Eiguren, and P. K. Rekdal, Phys. Rev. Lett. **97**, 070401 (2006).

[16] D. Cano, B. Kasch, H. Hattermann, R. Kleiner, C. Zimmermann, D. Koelle, and J. Fortágh, Phys. Rev. Lett. **101**, 183006 (2008).

[17] B. Kasch, H. Hattermann, D. Cano, T. E. Judd, S. Scheel, C. Zimmermann, R. Kleiner, D. Koelle, and J. Fortágh, New J. Phys. **12**, 065024 (2010).

[18] I. Sapina and T. Dahm, New J. Phys. **15**, 073035 (2013).

[19] M. A. Naides, R. W. Turner, R. A. Lai, J. M. DiSciacca, and B. L. Lev, Appl. Phys. Lett. **103**, 251112 (2013).

[20] R. Doll and M. Näbauer, Phys. Rev. Lett. **7**, 51 (1961).

[21] B. S. Deaver and W. M. Fairbank, Phys. Rev. Lett. **7**, 43 (1961).

[22] F. Shimizu, C. Hufnagel, and T. Mukai, Phys. Rev. Lett. **103**, 253002 (2009).

[23] A. Emmert, A. Lupaşcu, M. Brune, J.-M. Raimond, S. Haroche, and G. Nogues, Phys. Rev. A **80**, 061604 (2009).

[24] T. Müller, B. Zhang, R. Fermani, K. S. Chan, Z. W. Wang, C. B. Zhang, M. J. Lim, and R. Dumke, New J. Phys. **12**, 043016 (2010).

[25] T. Müller, B. Zhang, R. Fermani, K. S. Chan, M. J. Lim, and R. Dumke, Phys. Rev. A **81**, 053624 (2010).

[26] B. Zhang, M. Siercke, K. S. Chan, M. Beian, M. J. Lim, and R. Dumke, Phys. Rev. A **85**, 013404 (2012).

[27] M. Siercke, K. S. Chan, B. Zhang, M. Beian, M. J. Lim, and R. Dumke, Phys. Rev. A **85**, 041403 (2012).

[28] S. Scheel, R. Fermani, and E. A. Hinds, Phys. Rev. A **75**, 064901 (2007).

[29] G. Nogues, C. Roux, T. Nirrengarten, A. Lupaşcu, A. Emmert, M. Brune, J.-M. Raimond, S. Haroche, B. Plaçais, and J.-J. Greffet, Eur. Phys. Lett. **87**, 13002 (2009).

[30] O. Romero-Isart, C. Navau, A. Sanchez, P. Zoller, and J. I. Cirac, Phys. Rev. Lett. **111**, 145304 (2013).

[31] V. Sokolovsky, D. Rohrlich, and B. Horovitz, Phys. Rev. A **89**, 053422 (2014).

[32] M. Singh, Opt. Express **17**, 2600 (2009).

[33] K. R. Patton and U. R. Fischer, Phys. Rev. Lett. **111**, 240504 (2013).

[34] D. Cano, H. Hattermann, B. Kasch, C. Zimmermann, R. Kleiner, D. Koelle, and J. Fortágh, Eur. Phys. J. D **63**, 17 (2011).

[35] F. London, Phys. Rev. **74**, 562 (1948).

[36] E. H. Brandt and J. R. Clem, Phys. Rev. B **69**, 184509 (2004).

[37] D. Cano, B. Kasch, H. Hattermann, D. Koelle, R. Kleiner, C. Zimmermann, and J. Fortágh, Phys. Rev. A **77**, 063408 (2008).

[38] M. Khapaev, A. Kidiyarova-Shevchenko, P. Magnelind, and M. Y. Kupriyanov, IEEE Trans. Appl. Supercond. **11**, 1090 (2001).

[39] D. A. Smith, S. Aigner, S. Hofferberth, M. Gring, M. Andersson, S. Wildermuth, P. Krüger, S. Schneider, T. Schumm, and J. Schmiedmayer, Opt. Express **19**, 8471 (2011).

[40] W. Ketterle and N. J. Van Druten, Adv. At., Mol., Opt. Phys. **37**, 181 (1996).

[41] K. B. Davis, M.-O. Mewes, and W. Ketterle, Appl. Phys. B **60**, 155 (1995).

[42] J. Märkle, A. J. Allen, P. Federsel, B. Jetter, A. Günther, J. Fortágh, N. P. Proukakis, and T. E. Judd, Phys. Rev. A **90**, 023614 (2014).

[43] K. R. Patton and U. R. Fischer, Europhys. Lett. **102**, 20001 (2013).

[44] X. Zhu, S. Saito, A. Kemp, K. Kakuyanagi, S.-I. Karimoto, H. Nakano, W. J. Munro, Y. Tokura, M. S. Everitt, K. Nemoto, M. Kasu, N. Mizuochi, and K. Semba, Nature (London) **478**, 221 (2011).

PHYSICAL REVIEW A **92**, 012517 (2015)

All-optical measurement of Rydberg-state lifetimes

Markus Mack,[*] Jens Grimmel, Florian Karlewski, Lőrinc Sárkány, Helge Hattermann, and József Fortágh[†]
CQ Center for Collective Quantum Phenomena and Their Applications, Physikalisches Institut, Eberhard-Karls-Universität Tübingen,
Auf der Morgenstelle 14, D-72076 Tübingen, Germany

(Received 26 May 2015; published 24 July 2015)

We have developed an all-optical method for measuring the lifetimes of nS and nD Rydberg states and demonstrate its capabilities with measurements on a dilute cloud of ultracold ^{87}Rb atoms in a cryogenic environment. The method is based on the time-resolved observation of resonant light absorption by ground-state atoms and selective transfer of Rydberg atoms into the ground state at varying delay times in order to reconstruct Rydberg decay curves. Our measurements of the ^{87}Rb $30S_{1/2}$ state indicate an increase of the lifetime at lowered environment temperatures, as expected due to decreased blackbody radiation. For the $38D_{5/2}$ state with an attractive dipole-dipole interaction, ionization and lifetime reduction due to collisional effects are observed.

DOI: 10.1103/PhysRevA.92.012517 PACS number(s): 32.10.−f, 32.80.Ee, 32.80.Rm

I. LIFETIMES OF RYDBERG ATOMS

Rydberg atoms are promising for quantum information processing due to their strong and highly tunable interaction properties [1]. High-fidelity quantum gates and coherent-state transfer between Rydberg and long-living ground states have been proposed [2,3]. The fidelity of these operations is, however, fundamentally limited by the finite lifetime of Rydberg states [1]. Besides the natural decay of the Rydberg excitation, blackbody-radiation-induced transitions [4,5], collisions [6], and superradiance [7] may also limit the lifetime. The characterization of the Rydberg-state decay is thus of significant interest.

For individual Rydberg atoms at an environment temperature $T = 0$ the lifetime of an excited state is given by the inverse sum over all spontaneous decay rates into lower-lying states [8]. Due to the highest energy difference, the lowest-lying states contribute most to the decay. This is a limiting factor for calculations because the potentials for low-lying states cannot be described as accurately as those of higher states, which become more and more hydrogenlike with increasing n and l quantum numbers. In a finite-temperature environment, transitions induced by blackbody radiation (BBR) occur. The strongest transitions are those to nearby dipole-allowed Rydberg states both above and below in energy. For a perfect Planck photon distribution and well-known temperature the corresponding rates can be calculated with high accuracy [4,5]. The experimental verification of BBR-induced transition rates is possible not only through Rydberg lifetime measurements [9] but also indirectly by, e.g., measurements of Stark maps [10], which depend on the same dipole matrix elements. Any incoherent repopulation of the originally excited Rydberg state by multiple BBR transitions can be easily included in theoretical models but is usually negligible in magnitude. Also, blackbody-induced ionization by transitions to continuum states can be taken into account [11].

Direct lifetime measurements at lowered environment temperatures, as well as measurements of temperature-dependent BBR transfer rates, have been conducted for Na atoms [9,12]. The most accurate values for Rb Rydberg lifetimes to date have been measured in a room-temperature environment, relying on the knowledge of BBR transition rates in order to extract zero-temperature natural lifetimes. Measurements of nS and nD states in the range of $n = 27$ to 44 were conducted by exciting Rydberg atoms from a cloud of ultracold atoms prepared in a magneto-optical trap (MOT), waiting some varying delay time, and then applying an electric-field pulse while monitoring the time-dependent ionization signals (selective field ionization, SFI) [13,14]. Due to the difficulty of accurately distinguishing between close-lying Rydberg states which are populated because of BBR (see discussion in [15,16]), the technique was improved in [17]. By adding a microwave transfer of the "target" Rydberg atoms to a higher-lying state which can be accurately discriminated, this potential source of systematic error was eliminated. The results of [17] generally agree with previous work and cover Rb nS, nP, and nD states in the range $28 \leqslant n \leqslant 45$. To our knowledge, neither lifetimes of Rb at lowered environment temperatures nor any BBR transition rates have yet been measured. Consequently, an experimental verification of the BBR rate calculations [4] for Rb is still required.

In general, the lifetime of Rydberg atoms in ultracold gases is altered by several effects. Any electric fields lead to state mixing and ionization [8]. Collisions between atoms, as well as dipole-dipole and higher-order interaction between Rydberg atoms, which may also lead to collisions [18], cause changes of the atomic states and ionization [6,19]. Furthermore, depending on atomic density and cloud geometry, microwave superradiance is likely to occur, which can be triggered by blackbody radiation [7,20]. Due to such effects, the lifetimes of Rydberg atoms can differ greatly from the undisturbed values, as well as from one experiment to another. Therefore, measuring Rydberg lifetimes under the given conditions is necessary.

While the SFI methods mentioned above can be used when an electron or ion detector is present, an increasing number of recent cold-atom experiments have relied solely on optical detection, mostly employing electromagnetically induced transparency (EIT) instead [21–24]. In order to enable the determination of Rydberg lifetimes in such systems, as well as in cases where a reduced complexity of the setup

---

[*] markus.mack@uni-tuebingen.de

[†] fortagh@uni-tuebingen.de

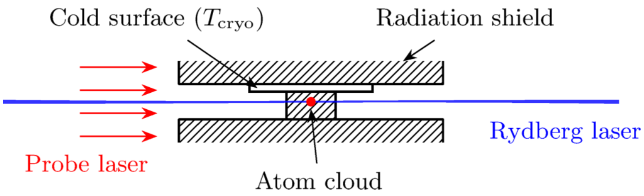

FIG. 1. (Color online) Cloud of ultracold ^{87}Rb atoms (center) inside the radiation shield of a cryostat (hatched). The radiation shield is cylindrical in shape with a 4.5-mm gap and 35-mm diameter. While the cold surface is at $T_{\rm cryo}$, the temperature of the radiation shield is slightly higher. The outside temperature is assumed to be close to 300 K.

compared to that of the SFI approach with the additional microwave is desired, we developed a similarly powerful, all-optical method for measuring state-specific lifetimes. The approach is technologically simplified as the same lasers that are used for Rydberg excitation are employed for detection, requiring only an additional photodiode for the measurement of resonant absorption.

We describe the optical lifetime measurement of Rydberg states in Sec. II and demonstrate its application in a setup with cold ^{87}Rb atoms (see Fig. 1) at cryogenic environmental temperatures in Sec. III. Factors influencing the accuracy of the method are discussed in Sec. IV.

II. OPTICAL LIFETIME MEASUREMENT METHOD

The optical measurements presented in this article rely on time-resolved resonant absorption detection in an effective three-level ladder-type system, as shown in the inset of Fig. 2, similar to the scheme in [25]. The transmission of a *probe laser* pulse resonant to a closed cycling transition between a ground state $|g\rangle$ and a quickly decaying intermediate excited state $|e\rangle$ is monitored with a photodiode. The duration of this pulse should be several times the expected Rydberg lifetime. The lifetime of $|e\rangle$ must be shorter than the expected time resolution of the final Rydberg decay curves. For Rydberg excitation a *Rydberg laser* resonant to the transition between $|e\rangle$ and the target Rydberg state $|r_1\rangle$ is used simultaneously with the probe laser. In principle, this configuration allows excitation by means of a stimulated Raman adiabatic passage pulse [26]. The experimental sequence, aimed at measuring changes in the optical density due to the laser pulses, consists of several steps. In each step, a cloud of ultracold atoms is prepared and released from the trap, and after a given time of flight a series of laser pulses depending on the current step is applied, as shown in Fig. 2.

As a baseline calibration, the probe laser-light-intensity signals without any atoms [step I, signal $I_0(t)$] and with ground-state atoms [step II, $I_{\rm g}(t)$] are recorded, giving the time-dependent optical density (Lambert-Beer law):

$$D^{\rm opt}_{\rm noexc.}(t) = -\ln[I_{\rm g}(t)/I_0(t)], \qquad (1)$$

In general, during the relevant time scales, the optical density is proportional to the number of atoms in the volume of the cloud “seen” by the probe laser beam.

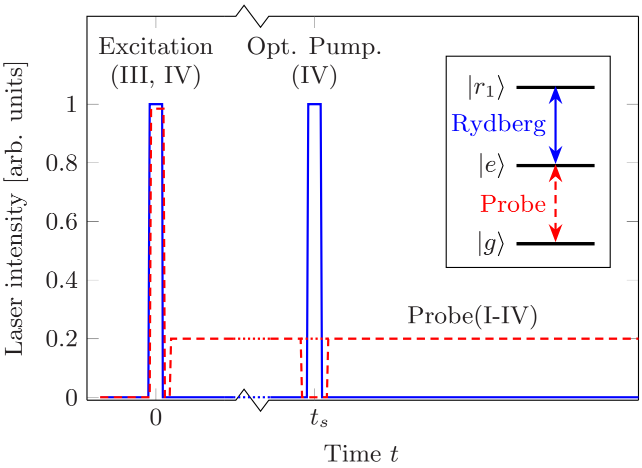

FIG. 2. (Color online) Illustration of the pulse sequence for steps I to IV used for the optical lifetime measurement for the probe (dashed red lines) and Rydberg (solid blue lines) lasers, resonant to the $|g\rangle \leftrightarrow |e\rangle$ and $|e\rangle \leftrightarrow |r_1\rangle$ transitions. For the calibration (step I without atoms and step II with atoms), only the probe laser is turned on after $t = 0$ for a duration of several hundred microseconds (much greater than the Rydberg lifetime; only the initial part is shown in the plot). Starting at step III, at $t = 0$ atoms are excited to the Rydberg state $|r_1\rangle$ (Excitation). For step IV, which is repeated several times, the long probe pulse is interrupted at time t_s for a short duration, during which an optical pumping pulse of the Rydberg laser is applied (Opt. Pump.). t_s is varied with each repetition of step IV.

In step III, the Rydberg excitation at $t = 0$ just before the start of the probe pulse is added. Due to excited atoms that are missing from the ground state, there will be increased transmission compared to that in step II. Again, the optical density of ground-state atoms $D^{\rm opt}_{\rm w/exc.}(t)$ can be calculated as in (1). In combination with the result from step II, an additional quantity

$$p_{\neq {\rm g}}(t) = 1 - D^{\rm opt}_{\rm w/exc.}(t)/D^{\rm opt}_{\rm noexc.}(t) \qquad (2)$$

can be determined, which gives the number of atoms *not* in the ground state due to the excitation pulse, normalized to the total number of atoms in the detection volume. The value of $p_{\neq {\rm g}}$ in the beginning is the fraction of atoms that have been excited to the Rydberg state, except for transitions to other states that have already happened due to BBR and possible superradiance, as was noted in [25]. The whole $p_{\neq {\rm g}}$ curve represents an effective decay of all directly and indirectly excited states, which is nearly, but generally not perfectly, exponential in shape because of the differing lifetimes of the constituent Rydberg states that become populated. Also, if ionizing effects played a role, the curve will not return to zero for long times but converge towards a finite value. The resulting $p_{\rm ion} = p_{\neq {\rm g}}(t \to \infty)$ is a measure for the strength of any ionizing effects if other mechanisms can be excluded that specifically remove Rydberg atoms, but not ground-state atoms, from the detection volume or, alternatively, transfer them into other stable states outside the probe transition. In general, the decay curve must consist of the (as yet unknown) parts

$$p_{\neq {\rm g}}(t) = p_{{\rm r}_1}(t) + p_{{\rm r}_{\neq 1}}(t) + p_{\rm ion}(t), \qquad (3)$$

i.e., the population of the originally excited Rydberg state, other Rydberg states, and the number of ionized atoms.

In order to separate the decay of the originally excited Rydberg state $|r_1\rangle$ from others that become populated, a state transfer similar to the microwave transfer in [17] is employed in step IV. However, instead of the additional microwave, the same Rydberg laser which was used for the excitation is used for a short optical pumping pulse at various times t_s during the expected decay of $|r_1\rangle$. This pumps a fraction of atoms still in the $|r_1\rangle$ state down to the intermediate $|e\rangle$ state. During this pulse, the probe laser needs to be turned off to prevent any reexcitation of the Rydberg state. Because the lifetime of the intermediate state is short, the atoms pumped back in this fashion will reappear as ground-state atoms as soon as the probe laser is turned on again after the optical pumping pulse. Following the same evaluation procedure as for step III, using (1) and (2), decay curves $p_{\neq g,s}(t)$ can be obtained. These must consist of the same parts with equal values as (3), except for a change in $p_{r_1}(t)$ at $t \geqslant t_s$, which has been reduced by some fraction α by the optical pumping pulse due to the Rydberg population in $|r_1\rangle$ at time $t = t_s$, leaving

$$p_{r_1,s}(t_s) = (1-\alpha)p_{r_1}(t_s). \tag{4}$$

Thus, by subtracting the decay curves $p_{\neq g,s}(t)$ from the curve without optical pumping $p_{\neq g}(t)$ of step III, information about the original $|r_1\rangle$ population at time $t = t_s$ can be obtained:

$$\alpha p_{r_1}(t_s) = p_{\neq g}(t_s) - p_{\neq g,s}(t_s). \tag{5}$$

As long as the optical density of the Rydberg atoms for the Rydberg laser is small or the optical pumping is fast enough to transfer all of the $|r_1\rangle$ atoms ($\alpha = 1$), α will be a constant fraction for each t_s. Repetition of step IV for different t_s and evaluation of $\alpha p_{r_1}(t_s)$ yields the decay of the population p_{r_1}, giving the lifetime of the Rydberg state $|r_1\rangle$. In the case only spontaneous decay and BBR contribute to the lifetime, this will be an exponential decay with a decay parameter τ independent of α.

III. CONDUCTED MEASUREMENTS AND RESULTS

We employed the method in a series of experiments in a setup where a cloud of 4×10^5 to 8×10^5 ^{87}Rb atoms with a temperature of 1.5 μK is transferred into a gap of the radiation shield of a tunable temperature cryostat by means of optical tweezers (detailed in [27]). Details of the geometry are shown in Fig. 1. For excitation and detection we used the ^{87}Rb $5S_{1/2}(F=2) \leftrightarrow 5P_{3/2}(F=3)$ transition and a circular polarization, which is commonly used for imaging purposes. A repumping laser resonant to $5S_{1/2}(F=1) \leftrightarrow 5P_{3/2}(F=2)$, which was needed for the MOT operation as well, was used to effectively keep the $F=1$ ground state unpopulated at all times. The Rydberg excitation to $|r_1\rangle$ is done by a pulse of the probe laser, with a higher intensity (approximately five times) than in actual probing, and, simultaneously, the Rydberg laser pulse resonant to the $5P_{3/2}(F=3) \leftrightarrow 30S_{1/2}$ or $38D_{5/2}$ state. The probe and Rydberg lasers are frequency stabilized to a frequency comb and arranged as described in [25]. The Rydberg laser was focused down to a size of $\approx$100 μm with a total power of $\approx$20 mW. The measurement sequence as described in Sec. II was conducted at times of flight (TOFs) of 12.0 and 20.5 ms in order to reduce the atom density to $7(3) \times 10^9/\mathrm{cm}^{-3}$ and $1.5(5) \times 10^9/\mathrm{cm}^{-3}$, respectively. The setup did not allow for controlled compensation of stray electric fields (which have been investigated in detail elsewhere [28]), leaving residual fields of 6.6 V cm^{-1} for the $30S$ state measurements and, after optimizing the cloud position, 0.5V/cm for those in the $38D$ state. Due to limited Rydberg laser power, pulse durations of 1μs were chosen for both the excitation and optical pumping pulses. In order to reduce the statistical errors, mainly a result of photodiode and other technical noise, $\geqslant$30 shots per step were averaged. The time resolution of the photodiode signal of each shot was digitally reduced to 0.5μs by temporal averaging. Furthermore, because of atom-number fluctuations, (1) and (2) were individually calculated for each single-shot measurement and corrected for atom-number drifts. In order to decrease statistical noise, the results of shots belonging to the same step (and repetition number s for step IV) were averaged.

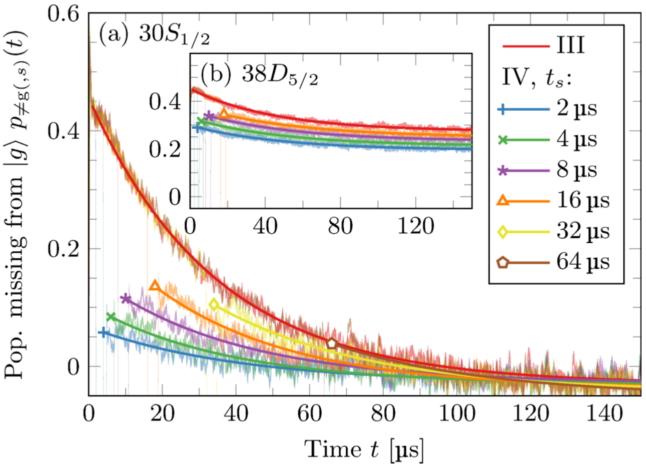

FIG. 3. (Color online) (a) Time-dependent populations of states not contributing to the probe transition, $p_{\neq g}$ (step III) and $p_{\neq g,s}(t)$ (step IV with repetition number s and corresponding optical pumping time t_s), representing an intermediate result of the evaluation of the measurement of the $30S_{1/2}$ state at $T_{\mathrm{cryo}} = 300$ K and a TOF of 20.5 ms. Shaded areas show statistical errors of the signal at each instant of time. Solid lines show exponential fits corresponding to each measurement step. Markers show the values $p_{\neq g,s}(t_s)$ obtained from the fit. (b) $38D_{5/2}$ state at $T_{\mathrm{cryo}} = 160$ K, showing only a fraction of atoms returning to the ground state depending on the optical pumping time t_s, converging towards values up to $p_{\mathrm{ion}} \approx 0.3$.

Figure 3 shows exemplary results for the number of atoms missing from the ground state, $p_{\neq g}(t)$ and $p_{\neq g,s}(t)$, where up to six values of t_s have been used at increasing intervals. For both states, an approximation of the curves by exponential functions, which were used for fitting in order to determine the points $p_{\neq g,s}(t_s)$, was sufficient. While for $30S_{1/2}$ all atoms eventually return to the ground state, for the $38D_{5/2}$ state this is clearly not the case. This is most probably caused by ionizing collisions due to the known attractive dipole-dipole interaction for this state [29]. While more than half of the Rydberg atoms are apparently already lost at $t < 2\mu$s, a small fraction was prevented from being ionized by the optical pumping pulses.

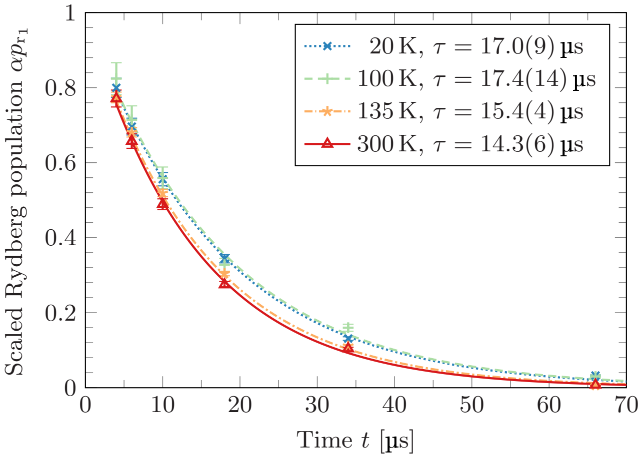

FIG. 4. (Color online) Measured populations $\alpha p_{r_1}(t_s)$ of the $30S_{1/2}$ state, proportional to the decays of $|r_1\rangle$, at several cryostat temperatures in the range 20 to 300 K. The lines are exponential fits to the data, giving the decay parameters τ and their estimated error based on the fit (add $\pm 1.0\mu$s systematic error common to all measurements for absolute uncertainty).

The final evaluation step yielding $\alpha p_{r_1}(t_s)$ is shown in Fig. 4 for the state $|r_1\rangle = 30S_{1/2}$, measured at cryostat temperatures in the range of 20 to 300 K, at a TOF of 20.5 ms, resulting in values $\tau = 14.3(6)\mu$s ($T_{\text{cryo}} = 300$ K) up to $\tau = 17.0(8)\mu$s ($T_{\text{cryo}} = 20$ K) with an additional common systematic error of $\pm 1.0\mu$s. Compared with the established measured value $\tau = 14.5(12)\mu$s ($30S_{1/2}, T = 300$ K, Fig. 2 in [14]), our result is very compatible.

However, while in our measurements there is a clear tendency for increased lifetimes at lowered temperatures, the effect is not as pronounced as expected from the calculated values from [4], giving $\tau = 26.6$ μs at $T = 0$ K. In order to check for any systematic dependencies on geometrical effects arising due to the falling and expanding cloud, as well as the presence of any density-dependent lifetime-reducing effects, the measurements for $30S_{1/2}$ were repeated with a time of flight of 12 ms. This resulted in an increase of the atom density and the optical density by roughly a factor of 2. The resulting lifetimes for $30S_{1/2}$ were $\tau = 14.1(14)\mu$s ($T_{\text{cryo}} = 300$ K) up to $\tau = 16.0(7)\mu$s ($T_{\text{cryo}} = 20$ K), i.e., no discernible difference compared to the measurements with TOF of 20.5 ms. Therefore, we suspect insufficient shielding from outside thermal radiation in our setup as the main cause for the discrepancy in comparison to theory at low temperatures. The geometry as shown in Fig. 1 leads to a solid angle of $4\pi \times 0.87$ covered by cold surfaces. Also, the lower part of the radiation shield is not ideally thermally coupled to the cryostat and is estimated to be at least 20 K warmer than the upper surface at temperatures near $T_{\text{cryo}} = 4.2$ K, causing the effective temperature relevant for BBR to be significantly higher than the cryostat temperature.

The lifetime of the $38D_{5/2}$ state, with a TOF of 20.5 ms, was measured to be 13(4) μs ($T_{\text{cryo}} = 160$ K) and 19(3) μs ($T_{\text{cryo}} = 20$ K), much lower than the reference value of $\tau = 30(2)\mu$s ($T = 300$ K; Fig. 2 in [14]). This lifetime reduction comes as no surprise due to the interaction-induced ionizing collisions already observed in Fig. 3.

IV. ACCURACY CONSIDERATIONS

The time resolution of the method presented in Sec. II is limited by the length and timing accuracy of the excitation and optical pumping pulses, effectively adding uncertainty to times $t = 0$ and t_s. For our 1-μs pulses with a timing accuracy of <10 ns, this results in a systematic uncertainty of $\pm 1.0\mu$s common to all measurements taken under the same excitation conditions, limiting their absolute, but not differential, accuracy. Higher laser intensities, particularly of the Rydberg laser, would allow for shorter pulses. When choosing the sizes for both laser beams, geometry effects need to be considered: If there is any significant atomic motion due to time of flight or atomic temperature, the excitation volume should be smaller than the detection volume in order to avoid any Rydberg atoms leaving the detection volume during the measurement time. However, the measured Rydberg signal will be lower for increased detection volumes, affecting the signal-to-noise ratio. Furthermore, prolonged acceleration of the atoms due to radiation pressure will lead to Doppler shifts which can lead to systematical errors, especially with regard to the narrow Rydberg transitions. This is particularly relevant for the probe laser, which must be well below the saturation intensity of the probe transition ($I_0 \lesssim 0.2 I_{\text{sat}}$ in our experiments).

If, like in our experiments, the pulses are created using an acousto-optical modulator (AOM) in the laser-beam path, the probe pulse will have a certain switching time of ≈100 ns and will show intensity drifts resulting from polarization drifts during some device-dependent warm-up time. As long as the signal remains proportional to the light level seen by the atoms and the pulse shapes are well reproducible, these drifts cancel out when calculating the $D^{\text{opt}}(t)$ terms. The optical density itself will not be constant over the duration of the laser pulse since the atomic cloud is expanding, as well as being accelerated downwards by gravity; however, these effects cancel out as well in $p_{\neq \text{g}}(t)$.

The measured optical densities depend on the probe light polarization and Zeeman substates of the atoms. For low Rabi frequencies, optical pumping effects can become visible in the dynamic parts of the measured signals, particularly when turning the probe laser back on after the Rydberg laser pulses at times t_s, which in turn limits the accuracy of the determination of $p_{r_1,s}(t_s)$. These effects become especially pronounced when any stray magnetic fields split up the Zeeman sublevels, which would need to be compensated well below the magnitude of the earth's magnetic field for high accuracy. Stray electric fields, if sufficiently strong, would additionally lead to state mixing affecting the underlying physical lifetime of the measured state. According to our calculations (detailed in [10]), this would become relevant on a 1% (probability) level at 30 V/cm for the $30S_{1/2(|m_j|=1/2)}$ state and 2.2 V/cm for $38D_{5/2(|m_j|=1/2)}$, i.e., not leading to significant state mixing in our setup.

Regarding the measurements taken at a lowered environment temperature, mainly two sources of systematic error need to be taken into account: First, as mentioned before and discussed in [8], the effective temperature as seen by the atoms will not be the temperature of the cryostat unless the full 4π solid angle is covered. Second, the geometry of conducting parts of the experimental setup, like the radiation shield of the cryostat, can form an effective microwave resonator altering the BBR spectrum. This becomes especially relevant if their dimensions are close to the strongest transition wavelengths (like the $30S \leftrightarrow 30P$ transition with a wavelength of 1.9 mm or $30S \leftrightarrow 29P$ with a wavelength of 1.7 mm).

V. CONCLUSION AND OUTLOOK

We have presented an optical method for the measurement of Rydberg atom lifetimes, providing information about how they are influenced by effects like blackbody radiation and interactions between Rydberg atoms. Because no detector parts or high voltages are needed inside the vacuum chamber of the experimental setup, this method might prove particularly useful in otherwise complex systems, including atom-chip setups such as the one used here [27], or millikelvin systems [30], which might eventually lead to the realization of proposed quantum gate schemes such as those in [31,32].

While the use of an additional microwave population transfer such as the one in [17] is not necessary for state selectivity, it might be employed to measure the populations of neighboring Rydberg nP and nF states by generalizing the scheme to measure signal differences due to the microwave transfer. This way, both the populations of, e.g., a Rydberg nS and close-lying nP states could be monitored. This would, for example, allow for the distinction between superradiance, which highly depends on the population of such strongly coupled states, and other lifetime-reducing effects.

ACKNOWLEDGMENTS

This work was financially supported by the FET-Open Xtrack Project HAIRS and the Carl Zeiss Stiftung.

[1] M. Saffman, T. G. Walker, and K. Mølmer, Rev. Mod. Phys. **82**, 2313 (2010).

[2] D. Jaksch, J. I. Cirac, P. Zoller, S. L. Rolston, R. Côté, and M. D. Lukin, Phys. Rev. Lett. **85**, 2208 (2000).

[3] M. M. Müller, M. Murphy, S. Montangero, T. Calarco, P. Grangier, and A. Browaeys, Phys. Rev. A **89**, 032334 (2014).

[4] I. I. Beterov, I. I. Ryabtsev, D. B. Tretyakov, and V. M. Entin, Phys. Rev. A **79**, 052504 (2009).

[5] I. I. Beterov, I. I. Ryabtsev, D. B. Tretyakov, and V. M. Entin, Phys. Rev. A **80**, 059902(E) (2009).

[6] A. Walz-Flannigan, J. R. Guest, J.-H. Choi, and G. Raithel, Phys. Rev. A **69**, 063405 (2004).

[7] T. Wang, S. F. Yelin, R. Côté, E. E. Eyler, S. M. Farooqi, P. L. Gould, M. Koštrun, D. Tong, and D. Vrinceanu, Phys. Rev. A **75**, 033802 (2007).

[8] T. F. Gallagher, *Rydberg Atoms* (Cambridge University Press, Cambridge, 1994).

[9] W. P. Spencer, A. G. Vaidyanathan, D. Kleppner, and T. W. Ducas, Phys. Rev. A **25**, 380 (1982).

[10] J. Grimmel, M. Mack, F. Karlewski, F. Jessen, M. Reinschmidt, N. Sándor, and J. Fortágh, New J. Phys. **17**, 053005 (2015).

[11] I. I. Beterov, D. B. Tretyakov, I. I. Ryabtsev, V. M. Entin, A. Ekers, and N. N. Bezuglov, New J. Phys. **11**, 013052 (2009).

[12] W. P. Spencer, A. G. Vaidyanathan, D. Kleppner, and T. W. Ducas, Phys. Rev. A **24**, 2513 (1981).

[13] A. L. de Oliveira, M. W. Mancini, V. S. Bagnato, and L. G. Marcassa, Phys. Rev. A **65**, 031401 (2002).

[14] V. A. Nascimento, L. L. Caliri, A. L. de Oliveira, V. S. Bagnato, and L. G. Marcassa, Phys. Rev. A **74**, 054501 (2006).

[15] D. A. Tate, Phys. Rev. A **75**, 066502 (2007).

[16] L. L. Caliri and L. G. Marcassa, Phys. Rev. A **75**, 066503 (2007).

[17] D. B. Branden, T. Juhasz, T. Mahlokozera, C. Vesa, R. O. Wilson, M. Zheng, A. Kortyna, and D. A. Tate, J. Phys. B **43**, 015002 (2010).

[18] W. Li, P. J. Tanner, and T. F. Gallagher, Phys. Rev. Lett. **94**, 173001 (2005).

[19] R. A. D. S. Zanon, K. M. F. Magalhães, A. L. de Oliveira, and L. G. Marcassa, Phys. Rev. A **65**, 023405 (2002).

[20] J. O. Day, E. Brekke, and T. G. Walker, Phys. Rev. A **77**, 052712 (2008).

[21] A. Tauschinsky, R. M. T. Thijssen, S. Whitlock, H. B. van Linden van den Heuvell, and R. J. C. Spreeuw, Phys. Rev. A **81**, 063411 (2010).

[22] G. Günter, H. Schempp, M. Robert-de Saint-Vincent, V. Gavryusev, S. Helmrich, C. S. Hofmann, S. Whitlock, and M. Weidemüller, Science **342**, 954 (2013).

[23] D. Maxwell, D. J. Szwer, D. Paredes-Barato, H. Busche, J. D. Pritchard, A. Gauguet, M. P. A. Jones, and C. S. Adams, Phys. Rev. A **89**, 043827 (2014).

[24] H. Gorniaczyk, C. Tresp, J. Schmidt, H. Fedder, and S. Hofferberth, Phys. Rev. Lett. **113**, 053601 (2014).

[25] F. Karlewski, M. Mack, J. Grimmel, N. Sándor, and J. Fortágh, Phys. Rev. A **91**, 043422 (2015).

[26] T. Cubel, B. K. Teo, V. S. Malinovsky, J. R. Guest, A. Reinhard, B. Knuffman, P. R. Berman, and G. Raithel, Phys. Rev. A **72**, 023405 (2005).

[27] D. Cano, H. Hattermann, B. Kasch, C. Zimmermann, R. Kleiner, D. Koelle, and J. Fortágh, Eur. Phys. J. D **63**, 17 (2011).

[28] H. Hattermann, M. Mack, F. Karlewski, F. Jessen, D. Cano, and J. Fortágh, Phys. Rev. A **86**, 022511 (2012).

[29] A. Reinhard, T. C. Liebisch, B. Knuffman, and G. Raithel, Phys. Rev. A **75**, 032712 (2007).

[30] F. Jessen, M. Knufinke, S. Bell, P. Vergien, H. Hattermann, P. Weiss, M. Rudolph, M. Reinschmidt, K. Meyer, T. Gaber, D. Cano, A. Günther, S. Bernon, D. Koelle, R. Kleiner, and J. Fortágh, Appl. Phys. B **116**, 665 (2014).

[31] D. Petrosyan and M. Fleischhauer, Phys. Rev. Lett. **100**, 170501 (2008).

[32] J. D. Pritchard, J. A. Isaacs, M. A. Beck, R. McDermott, and M. Saffman, Phys. Rev. A **89**, 010301 (2014).

nature COMMUNICATIONS

ARTICLE

DOI: 10.1038/s41467-017-02439-7 OPEN

Coupling ultracold atoms to a superconducting coplanar waveguide resonator

H. Hattermann[1], D. Bothner[1,2], L.Y. Ley[1], B. Ferdinand[1], D. Wiedmaier[1], L. Sárkány[1], R. Kleiner[1], D. Koelle[1] & J. Fortágh[1]

Ensembles of trapped atoms interacting with on-chip microwave resonators are considered as promising systems for the realization of quantum memories, novel quantum gates, and interfaces between the microwave and optical regime. Here, we demonstrate coupling of magnetically trapped ultracold Rb ground-state atoms to a coherently driven superconducting coplanar resonator on an integrated atom chip. When the cavity is driven off-resonance from the atomic transition, the microwave field strength in the cavity can be measured through observation of the AC shift of the atomic hyperfine transition frequency. When driving the cavity in resonance with the atoms, we observe Rabi oscillations between hyperfine states, demonstrating coherent control of the atomic states through the cavity field. These observations enable the preparation of coherent atomic superposition states, which are required for the implementation of an atomic quantum memory.

---

[1] CQ Center for Quantum Science in LISA+, Physikalisches Institut, Eberhard Karls Universität Tübingen, Auf der Morgenstelle 14, D-72076 Tübingen, Germany. [2] Present address: Kavli Institute of Nanoscience, Delft University of Technology, PO Box 5046, 2600 GA, Delft, The Netherlands. Correspondence and requests for materials should be addressed to H.H. (email: hattermann@pit.physik.uni-tuebingen.de)

Hybrid quantum systems of superconductors and atomic spin ensembles have been proposed[1–3] for quantum information processing to overcome the limited coherence of superconducting qubits[4,5]. In the envisioned hybrid system, information is processed by fast superconducting circuits and stored in a cloud of cold atoms, which serves as a quantum memory[6–8]. Information is transferred between the two quantum systems using a superconducting coplanar waveguide resonator as a quantum bus. In recent years, coupling between superconducting structures and spin systems such as nitrogen vacancy centers[9–13] and ions in solid-state systems[14,15] has been observed. Cold atoms coupled to superconducting resonators would, furthermore, enable the implementation of novel quantum gates[16–19], the realization of a microwave-to-optical transducer[20,21], and on-chip micromasers[22]. The interaction between Rydberg atoms and three-dimensional superconducting microwave resonators has been a rich research topic, especially with regard to atom–photon interactions on the fundamental level[23]. Research on planar superconducting structures, however, holds the promise of switchable interactions between the subsystems, integration with scalable solid-state circuitry[24–26], and long information storage times in the atomic ensemble. While long coherence times in cold atoms have been studied extensively[27–31] and trapping and manipulation of atoms in the vicinity of superconducting chips has been demonstrated in a series of experiments[32–37], coupling between trapped atoms and planar superconducting resonators has not been shown yet.

In this article, we demonstrate magnetic coupling of ultracold magnetically trapped atoms to a superconducting coplanar waveguide resonator operated at temperatures around 6 K. The cavity is near resonant with the atomic hyperfine splitting of ^{87}Rb and coherently driven by an external microwave synthesizer. We investigate both the dispersive and the resonant coupling regime. By driving the cavity off-resonantly with respect to the atoms, the atomic states reveal an AC-Zeeman shift under the influence of the microwave (MW) field[38]. This leads to a shift of the atomic transition frequency, which is measured by Ramsey interferometry. We use the AC-Zeeman shift to reconstruct the microwave intensity in the coplanar resonator. In contrast, when the cavity is driven at a frequency corresponding to an atomic transition, Rabi oscillations between atomic hyperfine states are observed.

Our measurements present a vital step toward the realization of an atom–superconductor hybrid system, paving the way toward the implementation of an atomic quantum memory coupled to a superconducting quantum circuit and the realization of microwave-to-optical transducers.

Results

Atomic ensembles trapped in a coplanar waveguide resonator. For our experiments, we magnetically trap an ensemble of ultracold ^{87}Rb atoms in the state $5S_{1/2}F = 1$, $m_F = -1 := |1, -1\rangle$ close to a coplanar microwave resonator on an integrated atom chip. The chip comprises two essential structures: i) a Z-shaped wire for magnetic trapping of neutral atoms and ii) a superconducting coplanar waveguide (CPW) resonator (Fig. 1a, b).

The CPW resonator is an inductively coupled half-wavelength cavity[39] with a fundamental mode resonance frequency of $\omega_{\mathrm{Res}} \approx 2\pi \cdot 6.84$ GHz and a linewidth of $\kappa \approx 2\pi \cdot 3$ MHz corresponding to a quality factor of $Q \approx 2200$ in the temperature range ($T = 6$–7 K) relevant for the experiments described here. By varying the temperature of the atom chip, the resonance frequency of the microwave cavity can be tuned by about 30 MHz, where the atomic hyperfine transition frequency $\omega_{\mathrm{HF}} = 2\pi \cdot 6.8347$ GHz lies within this tuning range. Details on the chip design and fabrication methods can be found in Supplementary Note 1 of this article, and details on the cavity parameters and their temperature dependence in Supplementary Notes 2 and 3.

With the coupling inductors (Fig. 1c, d), the microwave cavity gap close to the Z trap provides a closed superconducting loop on the chip, in which the total magnetic flux is conserved. The other resonator gap does not form a closed loop, as the lower ground plane has been cut to avoid flux trapping. We take advantage of the flux conservation by freezing a well-defined amount of magnetic flux into the closed loop during the chip cooldown. A conservative magnetic trapping potential for the Rb atoms in the vicinity of the cavity mode is formed by the combination of flux-conserving loop currents and a homogeneous external field[31,40]. A homogeneous offset field along the y-axis $B_{\mathrm{off}} = 0.323$ mT is additionally applied to ensure a nonzero magnetic field amplitude in the trap minimum to avoid spin-flip losses.

$N_{\mathrm{at}} \sim 10^5$ atoms are magnetically trapped at a distance of ~20 μm above one of the CPW gaps and close to one of the ends of the cavity, where the antinodes of the standing microwave magnetic fields are located, cf. Fig. 1b, e. At this position, the magnetic MW field of the transversal wave in the cavity is oriented perpendicular to the quantization axis of the atomic spins (y direction). Figure 1f depicts the coupling to the magnetic MW field of the cavity, obtained from finite-element simulations (Supplementary Note 4), in a cross-sectional view of the resonator. Solid white lines indicate the calculated positions of equal atomic density for an atomic cloud of 800 nK. From the MW field amplitude at the position of the atoms, we estimate an average single-atom single-photon coupling strength of $g = \vec{\mu} \cdot \vec{B}_{\mathrm{ph}} \approx 2\pi \cdot 0.5\,\mathrm{Hz}$. The magnetic MW field and thus the coupling can be considered constant along the atomic cloud with an extension of ~100 μm in y direction, which is about two orders of magnitude smaller than the cavity and thus the wavelength. For the experiments described in this article, the cavity is driven by an external microwave synthesizer. In the limit of high photon numbers $n_{\mathrm{ph}} \gg N_{\mathrm{at}}$ explored in this article, the cavity field can be treated classically, and the collective coupling between an atom and the cavity is small compared to the damping rate. In the classical regime, the atoms couple individually to the cavity field, hence, the Rabi frequency is independent of the number of atoms in the cavity[41].

Sensing the cavity field with cold atoms. When driving the resonator at a frequency ω_{dress} off-resonant to the atoms, the atomic transition is shifted by the MW field. This AC-Zeeman shift can be experimentally detected and used to reconstruct the intensity of the cavity field. We measure the frequency of the atomic transition between the magnetically trapped states $|1, -1\rangle$ and $|2, 1\rangle$ using time-domain Ramsey interferometry. The two states exhibit the same first-order Zeeman shift, thereby strongly reducing the sensitivity of the transition frequency to magnetic fields. For the Ramsey measurements, the atoms are prepared in a coherent superposition driven by a pulsed MW field ω_{extMW} from an external antenna and an additional radio frequency of ω_{RF} fed to the Z-shaped trapping wire (green arrows in Fig. 2a). After a variable time T_{Ramsey}, a second MW + RF pulse is applied and the relative population in the two states is measured. The populations in the two states oscillate with the difference between the atomic frequency and the external frequency, $\omega_{\mathrm{at}} - (\omega_{\mathrm{extMW}} + \omega_{\mathrm{RF}})$. During the Ramsey sequence, the CPW cavity is driven by a field with a variable angular frequency ω_{dress} that is off-resonant to the atomic transition (Fig. 2b). This leads to an AC shift of the levels which depends on the detuning Δ between ω_{dress} and the atomic transition frequency. For a simple two-level system,

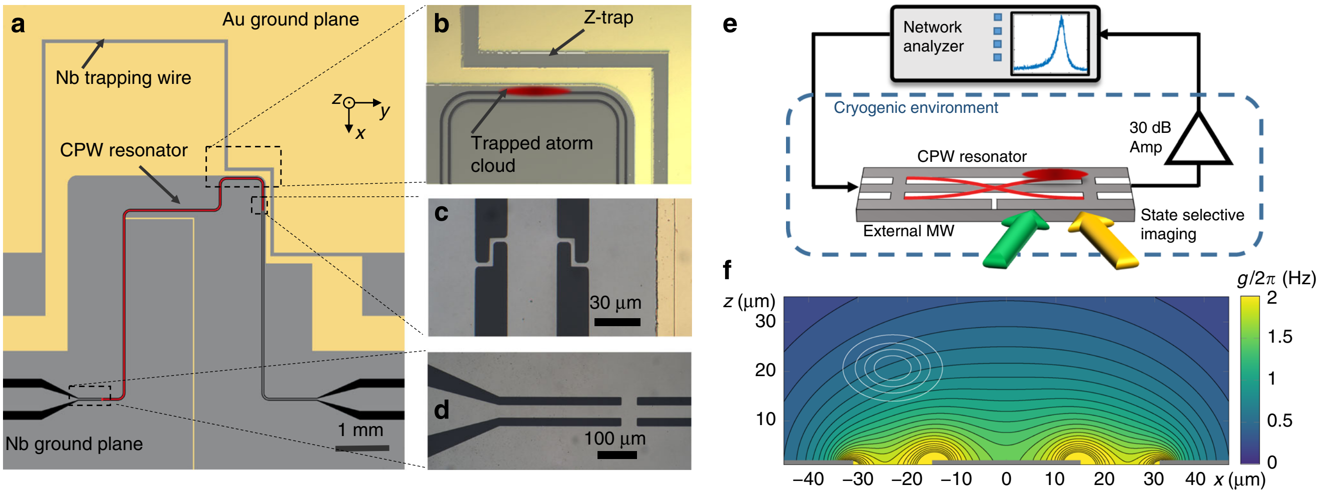

Fig. 1 A superconducting atom chip for coupling ultracold atoms to a coplanar resonator. **a** Schematic top view of the superconducting atom chip, comprising a Z-shaped trapping wire and a coplanar microwave resonator (center conductor marked in red). Parts of the niobium ground planes have been replaced by gold to circumvent the Meissner effect and facilitate magnetic trapping. The slit in the lower ground plane prevents the formation of a closed superconducting loop. **b** Optical microscope image of the trapping region with the position of the atoms trapped close to the antinode of the resonator. During the measurements, trapping is purely provided by persistent supercurrents around the upper cavity gap and external fields. **c** Microscope image of the coupling inductances at the output of the resonator and **d** at the input of the resonator. **e** Scheme of the measurement setup. Atoms are coupled to a driven coplanar waveguide resonator and detected by state-selective absorption imaging. For Ramsey experiments in the dispersive regime, additional external microwave fields are used to manipulate the atoms. **f** Simulated coupling strength $g/2\pi$ (Hz) between a single ground-state atom and a single photon in the cavity, resonant to the $|1, -1\rangle \rightarrow |2, 0\rangle$ transition. The white lines indicate positions of equal density for an atomic cloud of temperature $T_{\mathrm{at}} = 800$ nK in the trap, corresponding to 20, 40, 60, and 80% of the density in the center

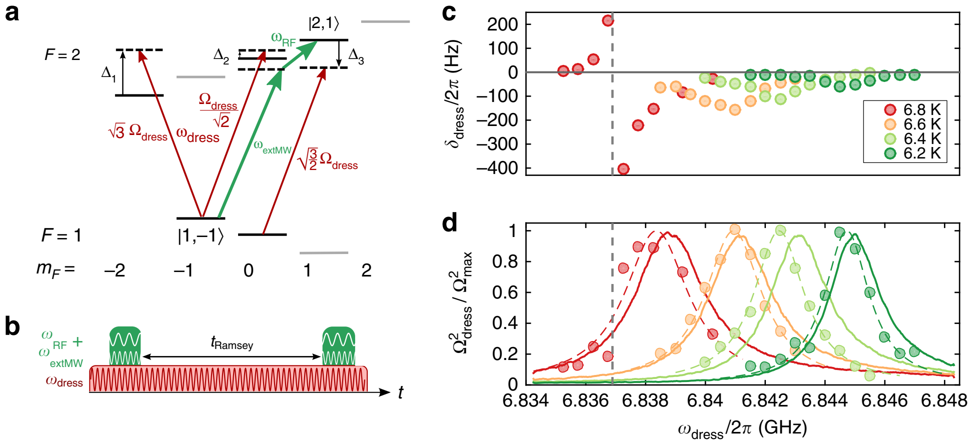

Fig. 2 Probing the off-resonant cavity field with cold atoms. **a** Level scheme of the ^{87}Rb ground-state manifold. The external MW and RF frequencies used for driving the two-photon transitions for the Ramsey scheme (green) and the off-resonant coupling of the cavity field to the relevant states are shown (red). **b** Experimental timing for the Ramsey sequence. The cavity field (red) is driven throughout the interferometric sequence. **c** Measured shift of the Ramsey frequency vs. frequency of the field in the superconducting microwave resonator for different chip temperatures. The sign change in the 6.8 K curve occurs at crossing the $|1, 0\rangle \rightarrow |2, 1\rangle$ transition, i.e., when $\Delta_3 = 0$, as indicated by dashed vertical line. **d** Data points: Calculated microwave intensity $\Omega^2_{\mathrm{dress}}$ based on the measurements of δ_{dress}. The colored dashed lines are Lorentzian fits to the data points. The solid lines are the measured transmission spectra of the microwave resonator

the off-resonant field shifts the atomic states by $\delta_{\mathrm{dress}} = \pm \frac{\Omega^2_{\mathrm{dress}}}{\Delta}$, where Ω_{dress} denotes the Rabi frequency of the dressing field and $\Delta = \omega_{\mathrm{dress}} - \omega_0$ is the detuning between the dressing field and the atomic transition frequency. The plus (minus) sign is valid for the ground (excited) state. The level scheme of the atoms involving all relevant fields is depicted in Fig. 2a. For a MW field which is linearly polarized perpendicular to the quantization axis, as it is in our case, the cavity field induces σ^- and σ^+-transitions with equal field strength, as depicted by the red arrows. This field hence couples the state $|1, -1\rangle$ to the states $|2, -2\rangle$ and $|2, 0\rangle$. The state $|2, 1\rangle$, on the other hand, is coupled to state $|1, 0\rangle$. This leads to a shift in the two-photon transition frequency $|1, -1\rangle \rightarrow |2, 1\rangle$ by

$$\delta_{\mathrm{dress}} = -\Omega^2_{\mathrm{dress}} \cdot \left(\frac{3}{\Delta_1} + \frac{1/2}{\Delta_2} + \frac{3/2}{\Delta_3} \right), \qquad (1)$$

which is measured in our experiment (Supplementary Note 5 for details). Here, $\Delta_i, i \in \{1, 2, 3\}$ denotes the detuning to the relevant atomic hyperfine transition. The numerical factors in the numerator are determined by the Clebsch–Gordan coefficients of the transitions.

For the measurement, the power of the microwave fed to the resonator and the magnetic offset field ($B_{\mathrm{off}} = 0.315 \pm 0.003$ mT) is held constant.

The measured frequency shift δ_{dress} in the Ramsey experiment is shown in Fig. 2c. As visible in the curve measured at $T = 6.8$ K, the dressing shift changes sign when the frequency of the dressing field is crossing an atomic resonance. Variation of the dressing frequency affects the shift in two ways, via the detuning to the atomic transitions and via a change in the microwave intensity in the resonator. Knowing the detuning to all involved levels, the normalized power of the microwave in the resonator, which is proportional to the square of the resonant Rabi frequency $\Omega^2_{\mathrm{dress}}$, can be deduced from the dressing shift. The calculated Rabi frequencies Ω_{dress} according to Eq. (1) are shown as circles in Fig. 2d. The measurement was repeated for different temperatures of the superconducting chip, corresponding to different cavity resonance frequencies. The result is compared with transmission spectra measured using a programmable network analyzer (solid lines in Fig. 2d). All curves are normalized to their maxima for the sake of comparability. Lorentzian curves (dashed lines) fitted to the data points match the transmission spectra closely in center frequency and peak width, which is on the order of $\kappa/2\pi \approx 2-3$ MHz. We note that there is a slight systematic offset between the reconstructed Rabi frequencies and the transmission curves. Possible explanations are trapping of Abrikosov vortices during the Ramsey measurement due to cycling of applied magnetic fields, which are known to shift the resonator frequency to lower values, or a small temperature difference (<50 mK) between the two measurements.

Coherent control of atomic states with cavity fields. When the electromagnetic cavity field is resonant with one of the (allowed) atomic transitions, the atoms undergo coherent Rabi oscillations between the ground and excited state (Fig. 3a). The observation of these oscillations demonstrates coherent control over the internal atomic degrees of freedom. The Rabi frequency is given by $\Omega_0 = \vec{\mu} \cdot \vec{B}_{\mathrm{MW}}$, where $\vec{\mu}$ is the atomic magnetic moment and $\vec{B}_{\mathrm{MW}}$ is the amplitude of the oscillating magnetic MW field. For the observation of these oscillations, we drive the cavity with a frequency of $\omega_0 = 2\pi \cdot 6.83242$ GHz, which is in resonance with the atomic transition $|1, -1\rangle \to |2, 0\rangle$, but detuned roughly by twice the cavity linewidth κ from the cavity resonance ($\omega_{\mathrm{cav}} \approx 2\pi \cdot 6.839$ GHz) at a chip temperature $T = 6.9$ K (Fig. 3b, c). By state-selective absorption imaging of the atoms, we observe resonant Rabi oscillations between the states $|1, -1\rangle$ and $|2, 0\rangle$ with a Rabi frequency $\Omega_0 \approx 2\pi \cdot 20$ kHz. By variation of the chip temperature between $T = 6.7$ and 7.0 K, the cavity frequency is shifted with respect to the atomic transition (Fig. 3d). This leads to a measurable change in the resonant Rabi frequency due to the altered MW power in the cavity, as visible in Fig. 3e. Here, the Rabi frequency increases with higher temperatures, as the cavity frequency approaches the atomic transition frequency. For temperatures around $T = 7.2$ K, the cavity resonance is shifted to coincide with the atomic resonance. However, at this temperature, the critical current of the superconducting coupling inductances is too low to support a stable magnetic trap.

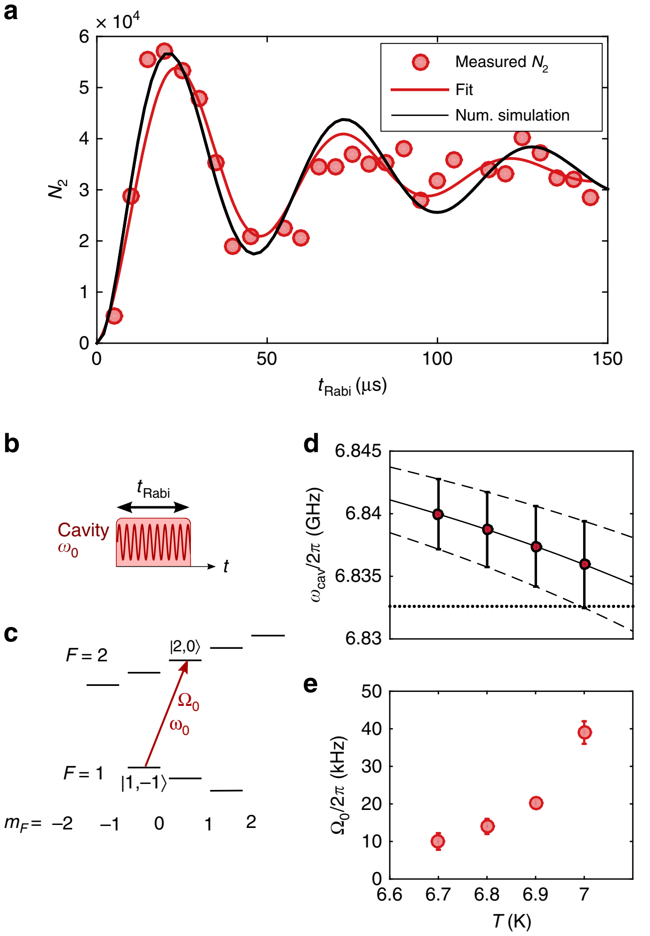

Fig. 3 Cavity-driven Rabi oscillations. **a** Measurement of the atoms in state $|2, 0\rangle$ reveals resonant Rabi oscillations between $|1, -1\rangle$ and $|2, 0\rangle$ for a cavity-driving frequency of $\omega_0 = 2\pi \cdot 6.83242$ GHz. The chip temperature was set to $T = 6.9$ K. The red solid line is a fit to the damped oscillation, and the black line shows the result of the numerical simulations. **b** Timing sequence and **c** level scheme for the driven one-photon Rabi oscillations. **d** Temperature dependence of the cavity resonance frequency. The circles and error bars indicate the peak and the width ($\pm\kappa$) of the cavity line obtained from fits to the resonator transmission data. The solid and dashed lines indicate the fitted temperature dependence of the cavity frequency and linewidth (Supplementary Note 3 for details). The horizontal dotted line indicates the driving frequency, corresponding to the atomic resonance. **e** Temperature dependence of the Rabi frequency. While the cavity is driven at the same frequency ω_0 for all measurements, the temperature dependence of the cavity resonance leads to a change in the microwave intensity. Error bars indicate the confidence interval of the Rabi frequency measurement

We observe a damping in the single-photon Rabi oscillations with a time constant of $\tau \approx 50$ μs. This damping is a result of the dephasing due to the inhomogeneous MW field of the cavity and the fact that Rabi oscillations are driven between two states with different magnetic moments. The magnetically trapped state $|1, -1\rangle$ is subjected to an energy shift of $\sim 2\pi\hbar \cdot 7$ MHz/mT, while the untrapped state $|2, 0\rangle$ is in first order insensitive to magnetic fields. As a consequence, the resonance frequency between the two states is not uniform across the cloud, and the atoms are only exactly on resonance at the center of the trap. A numerical simulation of a thermal cloud at $T_{\mathrm{at}} = 2$ μK trapped in a harmonic magnetic potential 20 μm above the cavity gap shows a damping time in excellent agreement with our measurement. We can estimate the number of photons in the resonator using the measured Rabi frequency and the simulated coupling strength per photon. Assuming a Rabi frequency of 20 kHz, we estimate the number of photons in the cavity $n_{\mathrm{Ph}} \approx 1.6 \times 10^9$, so that the thermal occupation of the cavity ($n_{\mathrm{th}} \sim 20$) is negligible.

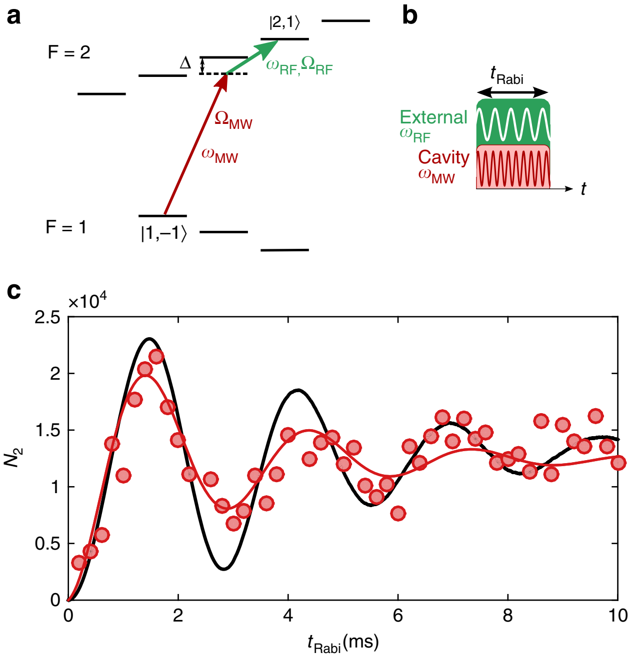

Fig. 4 Two-photon Rabi oscillations. **a** Level scheme and **b** timing sequence for the two-photon Rabi oscillations between the trapped states |1, −1⟩ and |2, 1⟩. **c** Observation of two-photon Rabi oscillations between states |1, −1⟩ and |2, 1⟩ (circles), and fit of the damped oscillation (red), yielding a damping time of $\tau = 5$ ms due to the inhomogeneity of the MW field amplitude across the cloud. The black solid line shows a numerical simulation of the state evolution for an ensemble of thermal atoms moving in the trap

In order to exploit the long coherence times of cold atoms, it is necessary to create superpositions between appropriate atomic states, which can both be trapped in the cavity. For ^{87}Rb, such a state combination consists of the hyperfine levels |1, −1⟩ and |2, 1⟩, which can both be trapped magnetically and exhibit excellent coherence properties. To this end, we start with an atomic cloud at a lower temperature of $T_{at} = 800$ nK and $N_{at} \sim 3 \times 10^4$ atoms in the state |1, −1⟩. In order to prepare a coherent superposition of the two states, we drive the cavity with the MW field ω_{MW} and employ an additional external RF field ω_{RF}, with a detuning of $\Delta = 2\pi \cdot 300$ kHz to the intermediate state |2, 0⟩ (cf. Fig. 4a). If the two corresponding Rabi frequencies are small compared to the intermediate detuning, i.e., $\Omega_{MW}, \Omega_{RF} \ll \Delta$, the population of the intermediate state can be neglected. In this case, the two-photon Rabi frequency Ω_{2Ph} can be calculated by adiabatic elimination of the intermediate state $\Omega_{2Ph} = \Omega_{MW}\Omega_{RF}/2\Delta$[42]. By driving the two fields with variable pulse lengths (Fig. 4b), we observe Rabi oscillations with $\Omega_{2Ph} = 2\pi \cdot 340$ Hz, and a dephasing on the order of $\tau \sim 5$ ms (Fig. 4c). A numerical simulation of an ensemble of noninteracting atoms in a magnetic trap reveals damping on the same timescale. As in the one-photon case, the dephasing is mainly due to the variation of the microwave field strength over the size of the atomic cloud (Supplementary Note 6).

Discussion

To make the presented cold atom–superconductor hybrid device a useful high-coherence quantum resource, several aspects need to be addressed and optimized. In particular, dephasing during the Rabi pulses should be reduced and the coupling between atoms and the cavity increased.

Dephasing due to inhomogeneous coupling, as seen in the experiment above, can be a limitation for the high-fidelity creation of superposition states needed in information processing. The inhomogeneity seen by the atomic ensemble can be reduced by reducing the cloud temperature, yielding smaller cloud extension in the trap (Supplementary Note 6). Several experiments have furthermore shown that reliable superpositions or quantum gates can be achieved in spite of this temporal or spatial variation of Rabi frequencies, as the related dephasing can be overcome using more elaborate MW and RF pulses using optimal control theory[43,44].

Furthermore, future experiments should be performed at chip temperatures in the mK regime to reduce the number of thermal photons, so, different ways to tune the cavity frequency need to be employed. Tuning the cavity could be achieved by various means, such as using nonlinear kinetic inductances[45], SQUIDs[46,47], or mechanical elements, as demonstrated in ref. [48].

For our geometry, we have estimated the coupling between a single atom and a single cavity photon to be $g \approx 2\pi \cdot 0.5$ Hz. Various means can be used to increase the coupling strength between the atoms and the cavity field. By decreasing the width of the gap W between the center conductor and ground planes of the cavity, the magnetic field per photon could be increased according to $B_{ph} \propto 1/W^2$, but would require the atoms to be trapped closer to the chip surface. By changing the resonator layout from CPW to lumped element resonator, the inductance and dimensions of the resonator could be decreased, leading to a significant enhancement of the current per photon and hence magnetic field B_{ph}. Finally, the electric field of the cavity mode could be used to couple neighboring Rydberg states, exploiting the large electric dipole moments of Rydberg states[49]. A similar experiment has been demonstrated with flying Rydberg atoms above a CPW transmission line[50]. For our geometry, the transition between the states $57S_{1/2}$ and $57P_{3/2}$ lies close to the third harmonic of our resonator. The dipole matrix element of this transition is $d \sim 2700\ ea_0$, yielding a single-photon single-atom coupling strength of $g/2\pi \approx 0.1$ MHz.

In summary, we have experimentally demonstrated coupling of ultracold ground-state atoms to a driven superconducting CPW resonator. Coupling was shown both in resonant Rabi oscillation and in dressing the frequency of an atomic clock state pair. Future measurements will explore collective effects of cold atoms to the cavity mode and work toward strong coupling between the superconducting resonator and Rydberg atoms. These experiments are the first step toward the implementation of cold atoms as a quantum resource in a hybrid quantum architecture.

Methods

Atomic cloud preparation. The atomic ensemble is prepared in a room-temperature setup and transported to a position below the superconducting atom chip using an optical dipole trap that is moved using a lens mounted on an air-bearing translation stage (cf. ref. [51] for details). Atoms are subsequently trapped in a magnetic trap generated by currents in the Z-shaped Nb wire and an external homogeneous bias field. The Z-wire configuration leads to a Ioffe-Pritchard- type magnetic microtrap with a nonzero offset field B_{off} at the trap minimum. We load $\sim 10^6$ atoms at a temperature of ~1 μK into the magnetic chip trap. After adiabatic compression, the cloud is transferred into the mode volume of the resonator by rotating the external bias field and switching off the current in the Z trap. Screening currents in the resonator, which conserve the flux in the closed superconducting loop, lead to the formation of a magnetic trap with oscillation frequencies $\omega_x = 2\pi \cdot 400\ s^{-1}$, $\omega_y = 2\pi \cdot 25\ s^{-1}$, and $\omega_z = 2\pi \cdot 600\ s^{-1}$ below the gap of the waveguide cavity, 20 μm from the chip surface. During the transfer into the tight trap, the atomic cloud is heated up to a temperature of $T_{at} \sim 2$ μK. At the cavity position, we perform radiofrequency evaporation to further cool the atomic ensemble.

Experimental cycle and state-selective detection. In order to measure the atomic state, the following experimental cycle is repeated every ~26 s. After preparation of an atomic cloud, transporting it to the superconducting chip, and loading into the cavity, as described above, all atoms are in the hyperfine state |1, −1⟩. Subsequently, we apply one MW (+RF) pulse of variable length t_{Rabi} for the measurement of Rabi oscillations, or two $\pi/2$-pulses of fixed length with a variable hold time t_{Ramsey} in-between for the Ramsey interferometry sequence. At the end of the sequence, we can measure the number of atoms in both of the states. First, the number of atoms in $F = 2$ is measured by illuminating the cloud with light resonant to the $5S_{1/2}$, $F = 2 \to 5P_{3/2}$, and $F = 3$ transition. The shadow of the atoms is imaged on a CCD camera and the measured optical density is used to determine the atom number. We then pump the atoms from $F = 1$ into $F = 2$ by illumination with a laser resonant with the $5S_{1/2}$, $F = 1 \to 5P_{3/2}$, and $F = 2$ transition. From the $5P_{3/2}$, $F = 2$ state, the atoms decay into $5P_{1/2}$, $F = 2$ in ~30 ns, and the atoms are imaged on a second CCD camera as described above.

Data availability. The data that support the findings of this article are available from the authors on reasonable request.

Received: 20 July 2017 Accepted: 26 November 2017

References

1. Xiang, Z.-L., Ashhab, S., You, J. Q. & Nori, F. Hybrid quantum circuits: Superconducting circuits interacting with other quantum systems. *Rev. Mod. Phys.* **85**, 623–653 (2013).
2. André, A. et al. A coherent all-electrical interface between polar molecules and mesoscopic superconducting resonators. *Nat. Phys.* **2**, 636–642 (2006).
3. Henschel, K., Majer, J., Schmiedmayer, J. & Ritsch, H. Cavity QED with an ultracold ensemble on a chip: Prospects for strong magnetic coupling at finite temperatures. *Phys. Rev. A* **82**, 033810 (2010).
4. Kim, Z. et al. Decoupling a Cooper-pair box to enhance the lifetime to 0.2 ms. *Phys. Rev. Lett.* **106**, 120501 (2011).
5. Paik, H. et al. Observation of high coherence in Josephson junction qubits measured in a three-dimensional circuit QED architecture. *Phys. Rev. Lett.* **107**, 240501 (2011).
6. Verdú, J. et al. Strong magnetic coupling of an ultracold gas to a superconducting waveguide cavity. *Phys. Rev. Lett.* **103**, 043603 (2009).
7. Patton, K. R. & Fischer, U. R. Hybrid of superconducting quantum interference device and atomic Bose–Einstein condensate: an architecture for quantum information processing. *Phys. Rev. A* **87**, 052303 (2013).
8. Patton, K. R. & Fischer, U. R. Ultrafast quantum random access memory utilizing single Rydberg atoms in a Bose–Einstein condensate. *Phys. Rev. Lett.* **111**, 240504 (2013).
9. Kubo, Y. et al. Strong coupling of a spin ensemble to a superconducting resonator. *Phys. Rev. Lett.* **105**, 140502 (2010).
10. Kubo, Y. et al. Hybrid quantum circuit with a superconducting qubit coupled to a spin ensemble. *Phys. Rev. Lett.* **107**, 220501 (2011).
11. Amsüss, R. et al. Cavity QED with magnetically coupled collective spin states. *Phys. Rev. Lett.* **107**, 060502 (2011).
12. Putz, S. et al. Protecting a spin ensemble against decoherence in the strong-coupling regime of cavity QED. *Nat. Phys.* **10**, 720–724 (2014).
13. Grezes, C. et al. Towards a spin-ensemble quantum memory for superconducting qubits. *Comptes Rendus Phys.* **17**, 693–704 (2016).
14. Schuster, D. I. et al. High-cooperativity coupling of electron-spin ensembles to superconducting cavities. *Phys. Rev. Lett.* **105**, 140501 (2010).
15. Probst, S. et al. Anisotropic rare-earth spin ensemble strongly coupled to a superconducting resonator. *Phys. Rev. Lett.* **110**, 157001 (2013).
16. Petrosyan, D. et al. Reversible state transfer between superconducting qubits and atomic ensembles. *Phys. Rev. A* **79**, 040304 (2009).
17. Petrosyan, D. & Fleischhauer, M. Quantum information processing with single photons and atomic ensembles in microwave coplanar waveguide resonators. *Phys. Rev. Lett.* **100**, 170501 (2008).
18. Pritchard, J. D., Isaacs, J. A., Beck, M. A., McDermott, R. & Saffman, M. Hybrid atom-photon quantum gate in a superconducting microwave resonator. *Phys. Rev. A* **89**, 010301 (2014).
19. Sárkány, L., Fortágh, J. & Petrosyan, D. Long-range quantum gate via Rydberg states of atoms in a thermal microwave cavity. *Phys. Rev. A* **92**, 030303 (2015).
20. Hafezi, M. et al. Atomic interface between microwave and optical photons. *Phys. Rev. A* **85**, 020302 (2012).
21. Gard, B. T., Jacobs, K., McDermott, R. & Saffman, M. Microwave-to-optical frequency conversion using a cesium atom coupled to a superconducting resonator. *Phys. Rev. A* **96**, 013833 (2017).
22. Yu, D., Kwek, L. C., Amico, L. & Dumke, R. Theoretical description of a micromaser in the ultrastrong-coupling regime. *Phys. Rev. A* **95**, 053811 (2017).
23. Haroche, S. & Raimond, J. *Exploring the Quantum: Atoms, Cavities, and Photons.* (Oxford Univ. Press, Oxford, 2006).
24. Wallraff, A. et al. Strong coupling of a single photon to a superconducting qubit using circuit quantum electrodynamics. *Nature* **431**, 162–167 (2004).
25. DiCarlo, L. et al. Preparation and measurement of three-qubit entanglement in a superconducting circuit. *Nature* **467**, 574–578 (2010).
26. Lucero, E. et al. Computing prime factors with a Josephson phase qubit quantum processor. *Nat. Phys.* **8**, 719–723 (2012).
27. Treutlein, P., Hommelhoff, P., Steinmetz, T., Hänsch, T. W. & Reichel, J. Coherence in microchip traps. *Phys. Rev. Lett.* **92**, 203005 (2004).
28. Deutsch, C. et al. Spin self-rephasing and very long coherence times in a trapped atomic ensemble. *Phys. Rev. Lett.* **105**, 020401 (2010).
29. Kleine Büning, G. et al. Extended coherence time on the clock transition of optically trapped rubidium. *Phys. Rev. Lett.* **106**, 240801 (2011).
30. Dudin, Y. O., Li, L. & Kuzmich, A. Light storage on the time scale of a minute. *Phys. Rev. A* **87**, 031801 (2013).
31. Bernon, S. et al. Manipulation and coherence of ultra-cold atoms on a superconducting atom chip. *Nat. Commun.* **4**, 2380 (2013).
32. Nirrengarten, T. et al. Realization of a superconducting atom chip. *Phys. Rev. Lett.* **97**, 200405 (2006).
33. Mukai, T. et al. Persistent supercurrent atom chip. *Phys. Rev. Lett.* **98**, 260407 (2007).
34. Roux, C. et al. Bose–Einstein condensation on a superconducting atom chip. *Europhys. Lett.* **81**, 56004 (2008).
35. Minniberger, S. et al. Magnetic conveyor belt transport of ultracold atoms to a superconducting atomchip. *Appl. Phys. B* **116**, 1017–1021 (2014).
36. Müller, T. et al. Programmable trap geometries with superconducting atom chips. *Phys. Rev. A* **81**, 053624 (2010).
37. Weiss, P. et al. Sensitivity of ultracold atoms to quantized flux in a superconducting ring. *Phys. Rev. Lett.* **114**, 113003 (2015).
38. Sárkány, L., Weiss, P., Hattermann, H. & Fortágh, J. Controlling the magnetic-field sensitivity of atomic-clock states by microwave dressing. *Phys. Rev. A* **90**, 053416 (2014).
39. Bothner, D., Wiedmaier, D., Ferdinand, B., Kleiner, R. & Koelle, D. Improving superconducting resonators in magnetic fields by reduced field-focussing and engineered flux screening. *Phys. Rev. Appl.* **8**, 034025 (2017).
40. Bothner, D. et al. Inductively coupled superconducting half wavelength resonators as persistent current traps for ultracold atoms. *New J. Phys.* **15**, 093024 (2013).
41. Chiorescu, I., Groll, N., Bertaina, S., Mori, T. & Miyashita, S. Magnetic strong coupling in a spin-photon system and transition to classical regime. *Phys. Rev. B* **82**, 024413 (2010).
42. Gentile, T. R., Hughey, B. J., Kleppner, D. & Ducas, T. W. Experimental study of one- and two-photon Rabi oscillations. *Phys. Rev. A* **40**, 5103–5115 (1989).
43. Schulte-Herbrüggen, T., Spörl, A., Khaneja, N. & Glaser, S. J. Optimal control for generating quantum gates in open dissipative systems. *J. Phys. B: At. Mol. Opt. Phys.* **44**, 154013 (2011).
44. Dolde, F. et al. High-fidelity spin entanglement using optimal control. *Nat. Commun.* **5**, 3371 (2014).
45. Vissers, M. R. et al. Frequency-tunable superconducting resonators via nonlinear kinetic inductance. *Appl. Phys. Lett.* **107**, 062601 (2015).
46. Palacios-Laloy, A. et al. Tunable resonators for quantum circuits. *J. Low. Temp. Phys.* **151**, 1034–1042 (2008).
47. Sandberg, M. et al. Tuning the field in a microwave resonator faster than the photon lifetime. *Appl. Phys. Lett.* **92**, 203501 (2008).
48. Kim, Z. et al. Thin-film superconducting resonator tunable to the ground-state hyperfine splitting of 87rb. *AIP Adv.* **1**, 042107 (2011).
49. Yu, D. et al. Charge-qubit21atom hybrid. *Phys. Rev. A* **93**, 042329 (2016).
50. Hogan, S. D et al.Driving rydberg-rydberg transitions from a coplanar microwave waveguide. *Phys. Rev. Lett.* **108**, 063004 (2012).
51. Cano, D. et al. Experimental system for research on ultracold atomic gases near superconducting microstructures. *Eur. Phys. J. D.* **63**, 17–23 (2011).

Acknowledgements

This work was supported by the Deutsche Forschungsgemeinschaft (SFB TRR21 & SPP 1929 GyRid) and the European Commission (FP7 STREP project "HAIRS"). H.H. and B. F. acknowledge additional support from the Carl Zeiss Stiftung and the Research Seed Capital (RiSC) programme of the MWK Baden-Württemberg.

Author contributions

D.K., R.K., J.F., and H.H. designed and mounted the experiment. D.B., D.W., B.F., and H. H. developed and fabricated the superconducting chip. H.H. and L.Y.L. carried out the experiments. H.H., D.B., L.Y.L., and B.F. analyzed the data. H.H., D.B., and B.F. performed the numerical simulations. L.S. provided the microwave dressing theory. D.K., R.K., and J.F. supervised the project. H.H., D.B., and J.F. edited the manuscript. All authors discussed the results and contributed to the manuscript.

Additional information

Supplementary Information accompanies this paper at https://doi.org/10.1038/s41467-017-02439-7.

Competing interests: The authors declare no competing financial interests.